COMPARISON OF POLYCYCLIC AROMATIC HYDROCARBON EMISSION TO HOT AND COLD DUST EMISSION IN M51, M83 AND NGC 2403

A thesis submitted to the University of Manchester
for the degree of Master of Science
in the Faculty of Engineering and Physical Sciences

December 2013

By

Andrew Jones

School of Physics and Astronomy

Contents

List of Tables

List of Figures

Abstract

Using *Spitzer Space Telescope* and *Herschel Space Observatory* data we investigate the relationship between the 8 μm continuum subtracted PAH emission to 24,160 and 250 μm dust emission for M51, M83 and NGC 2403. We find the 8 μm emission does not correlate with the 24 μm emission, showing signs of PAH inhibition in star forming regions. In NGC 2403 we find the 8 μm emission correlates well with the 250 μm emission, and the 8/250 μm surface brightness correlates well with the 3.6 μm surface brightness. This indicates the 8 μm PAH emission carriers are mixed in with the diffuse interstellar medium and are heated by the evolved stellar population. In M83 we find an almost linear relationship between the 8 μm and 160 μm emission. We find the PAHs are mixed in with the diffuse dust and the predominant heating source of the PAH emission is the UV radiation escaping from star formation. In M51 we find a complex relationship between the different dust emission components. In some areas this is similar to M83, and in other areas there is little relationship between the 8 and 160 μm and 8 and 250 μm dust emissions. We conclude by discussing relating PAH emission to dust mass and the implications of the relations between the different dust components when making models of dust and PAH emission in face on galaxies.

University of Manchester,
Andrew Jones
Master of Science
07 March 2013
Manchester,
M13 9PL.
Jodrell Bank Centre for Astrophysics,
Alan Turing Building,

Supervisor : Dr George J. Bendo
Advisor: Dr Clive. Dickinson

Declaration

No portion of the work referred to in this thesis has been submitted in support of an application for another degree or qualification of this or any other university or other institution of learning.

Andrew Jones

Jodrell Bank Centre for Astrophysics

Alan Turing Building

The University of Manchester

Oxford Road

Manchester

M13 9PL

U.K.

Copyright

i. The author of this thesis (including any appendices and/or schedules to this thesis) owns certain copyright or related rights in it (the Copyright) and s/he has given The University of Manchester certain rights to use such Copyright, including for administrative purposes.

ii. Copies of this thesis, either in full or in extracts and whether in hard or electronic copy, may be made only in accordance with the Copyright, Designs and Patents Act 1988 (as amended) and regulations issued under it or, where appropriate, in accordance with licensing agreements which the University has from time to time. This page must form part of any such copies made.

iii. The ownership of certain Copyright, patents, designs, trade marks and other intellectual property (the Intellectual Property) and any reproductions of copyright works in the thesis, for example graphs and tables (Reproductions), which may be described in this thesis, may not be owned by the author and may be owned by third parties. Such Intellectual Property and Reproductions cannot and must not be made available for use without the prior written permission of the owner(s) of the relevant Intellectual Property and/or Reproductions.

iv. Further information on the conditions under which disclosure, publication and commercialisation of this thesis, the Copyright and any Intellectual Property and/or Reproductions described in it may take place is available in the University IP Policy (see http://www.campus.manchester.ac.uk/medialibrary/policies/intellectual- property.pdf), in any relevant Thesis restriction declarations deposited in the University Library, The University Librarys regulations (see http://www.manchester.ac.uk/library/aboutus/regulations) and in The University's policy on presentation of Theses.

Acknowledgements

I would like to thank my supervisor Dr George J. Bendo for persevering with me through my grasp of the concepts, and patience when explaining areas I did not understand. I would not be here if it wasn't for my family, so Dad - I've done it! thank you for your support! I extend my gratitude to the students in both the east and west office for their friendly advice and help, and to the staff of the Jodrell Bank Centre for Astrophysics for their warm welcome into the department and the free tea, coffee and occasionally lunch we were provided with. Special mention to my fellow masters students, David, Carl, Rachana, Duncan and Phillipa, without whom, the whole experience would have been much less exciting. A personal mention to the University of Manchester Ski and Snowboard club (SKUM) for providing me with a means to escape the office on a wednesday and saturday, as well as the much needed holiday.

Andrew Jones

Jodrell Bank Centre for Astrophysics,

Alan Turing Building,

University of Manchester,

Oxford Road,

Manchester,

M13 9PL.

Supervisor: Dr George J. bendo

Advisor: Dr Clive. Dickinson

Chapter 1

Introduction

1.1 Background and Motivation

The evolution of galaxies can be traced out through stellar evolution. Stars are born when molecular clouds condense and the temperature and pressure ignite nuclear hydrogen fusion within the core of the clouds. These become protostars, then move onto the main sequence and progress up the Hertzsprung-Russell diagram, which through plotting the effective temperature verses luminosity can trace the life cycle of the star. Throughout their lifetime, stars give off intense radiation in the form of photons, and stellar winds in the form of charged particles and outflowing mass ejections. When stars die, they explode in novae scattering their enriched interiors into interstellar space, helping to shape and change its structure and contents. These processes feedback energy and mass into the ISM which in turn allows new stars to be born. This is a dynamic and every changing environment thanks to the constant feedback from the stellar population.

The life cycle of stars fills interstellar space with molecular gas and dust. Dust can be separated into hot and cold components where hot dust, defined here as having temperatures of $\sim$ 100 K, and cold dust ($\sim$ 20 K). As well as this dust are molecules which emit spectral features in the range of $3- \sim 20\mu$m, known as polycyclic aromatic hydrocarbons (PAH). These are large molecules consisting of many tens of carbon atoms and hydrogen atoms arranged in planar structures.

They have properties between the molecular gas and carbonaceous grains.

The dust plays an important role in the appearance of galaxies as well as the chemistry and star formation. Almost half of the starlight is reprocessed by the dust. The dust affects how galaxies look in multiwavelength observations. We see dust attenuation of wavelengths in the optical and UV range, whilst the dust contributes to infrared (IR) and submillimeter emission.

As well as the appearance of galaxies, dust also plays an important role in the chemistry of galactic evolution. Molecular hydrogen can be formed from dust grains and those same dust grains can shield the molecular gas, such that it is able to cool and condense and form stars. We can use hot dust emission powered by young stars to trace the star formation rate (SFR) of galaxies on a local and global scale.

The abundance of PAHs in the interstellar medium, mixed in with the dust grains has long been thought to show the PAH emission can be used to trace dust mass, though the heating sources of the PAHs remains in dispute. It is thought they are able to trace star formation. Work so far has been unable to provide accurate metrics to use PAH emission as a tracer of star formation. This is in part due to the molecules being unstable in the presence of strong UV radiation emitted from star forming regions. PAHs are thought to be excited by ultraviolet (UV) photons, which could possibly be attributed to star formation. Though there are theories that these molecules are excited by starlight from older stars, as such it is important to remember where the constraints for this lie.

1.2 Star Formation

As the universe ages, galaxies are transformed through star formation. This can be observed on scales ranging from individual stars forming regions in the Milky Way (MW) to large scale star formation in galactic and cosmological scales. Stars form through a mechanism whereby molecular clouds collapse under gravitational forces and condense. The infalling mass needs to be above a certain threshold in order for nuclear fusion to commence and a star to be born.

The Kennicutt Schmidtt law [Schmidt, 1959a] gives a basic understanding of the relationship between the SFR surface density and the local gas surface density.

$$\Sigma_{SFR} \propto (\Sigma_{gas})^n \tag{1.1}$$

The Σ_{SFR} is given in units of solar mass per year per parsec squared ($M_\odot\ yr^{-1}\ MPc^{-2}$) and the Σ_{gas} is in grams per parches squared (gparsec^{-2}). Measurements of Hα, H I, and CO distributions of many galaxies have constrained the value of n to be 1.4$\pm$. 0.15 [Kennicutt, 1998]. The Kennicutt-Schmidt Law provides good upper and lower estimations of the SFR, and extends to several orders of magnitudes in both the SFR and molecular gas density. This allows the SFR to be estimated through the relations between the dust and gas masses of the ISM.

It is possible to track the formation of new stars through a variety of multiwavelength observations and measure the SFR. With the advent of multiwavelength observations, star formation diagnostics techniques have improved to an extent where uncertainties in SFR are much smaller than they were just 10 years ago, often by an order of magnitude [Kennicutt and Evans, 2012].

The methods commonly used to measure SFR are outlined below. The infrared SFR tracers are described in Section 1.4 as these tie in nicely with PAH emission and are split into hot and cold dust components, section 1.6 deals with PAH emission as possible SFR tracers.

1.2.1 Star Counting and Colour Magnitude Diagram

A direct way of measuring SFR is to count the number of stars within a range of ages. Provided reliable data for the masses and luminosity are present, it is possible to infer the age of a star cluster by plotting the colour versus magnitude in a Hertzsprung-Russell diagram. By identifying the turn-off point for the main sequence in this diagram, it is possible to determine the age and ultimately the SFR.

For extragalactic observations, the resolution of the image is the main constraint, where the individual stars cannot be identified. The largest problem with this method for galactic observations is that not all objects in the field of view can be confirmed as stars, so care must be taken when counting the objects. This method only works for nearby objects, such as galaxies within the Local Group. Despite some inaccuracies with identifying stars and issues with dust obscuration, this remains one of the most direct methods of measuring SFR.

1.2.2 UV Continuum

The UV continuum (near the Lyman break) has a peak contribution from young stars of many 10s $M_{\odot}$. These very hot stars only live for 200 Myr, so UV light traces the most recent star formation in both the MW and extragalactic sources [Hao et al., 2011, Murphy et al., 2011] .

This method is heavily affected by dust obscuration. Since a variable fraction of the starlight is absorbed by the dust, the conversion between UV flux and SFR has high uncertainties, however it is possible to fit a profile to the spectral energy distribution of the dust attenuation and use that to correct the UV continuum for extinction [Calzetti et al., 1994, Kong et al., 2004, Seibert et al., 2005, Johnson et al., 2007, Salim et al., 2007, Treyer et al., 2007, Hao et al., 2011]. The infra red emission from the dust is assumed to be a product of the UV starlight absorbed by the dust. This emission is added back to the total UV flux to account for the dust extinction.

1.2.3 Emission Lines

Emission lines are the result of electrons changing their energy levels within atomic gases. The electron jumps to a higher energy state and upon dropping back down to a lower state, emit a photon. The wavelength of the photon is dependant on the gap between the energy levels. The notations for hydrogen are given with respect to the lowest energy state transitioned to. Lyman, Balmer and Paschen correspond to n=1, n=2 and n=3 respectively.

These emission lines, along with free-free emission, trace very young stars, and thus can be used to measure near-instantaneous SFRs. One of the emission lines most commonly used to trace star formation in both distant and local sources is Hα (6562.8 Å). For more distant galaxies, the Hα line is no longer useful, due to it being redshifted to millimetre and sub millimetre wavelengths. At high redshift, z, Hα becomes lost in the IR continuum [Ouchi et al., 2009]. Other emission lines can be used to trace these distant sources. Lyman$_\alpha$ emission at (1215.68Å) is a popular choice. We need to be careful when using this source as the flux we see from Lα is only a fraction of the total flux emitted in these galaxies. The Lα emission line is therefore only useful when observing star formation across galactic scales and not the individual regions within the galaxies.

Again, there are major issues with dust attenuation. Also in areas where the SFR is very low (ie where few massive stars are present), the accuracy in the SFR measured using emission lines drops off [Cerviño et al., 2003]. Calzetti et al. [2007] have used a calibration for dust corrected Hα surface brightness. The calibration allows for dust absorption by considering the 24 μm IR waveband accounts for the lost Hα emission. This is factored back into the corrected flux. This workaround is a neat solution to the problems of dust absorption for Hα. Kennicutt et al. [2009] expanded on from this work using a different metric by combining total IR luminosities (TIR) with Hα, as well as 8 μm + 24 μm luminosities. These methods work well to show that the TIR flux is consistent with the extinction corrected Hα fluxes tracing out star formation.

1.2.4 Radio Tracers

Synchrotron

Synchrotron emission dominates lower radio frequency emission (emission at < 5 GHz). This emission is generated by charged particles from supernovae explosions. Helou et al. [1985], Condon [1992] have observed a correlation between nonthermal radio emission and far-infrared emission from galaxies. Models of SFR produced by Bell [2003] tend to favour high luminosity galaxies as they underestimate SFR in the low luminosity galaxies by a factor of about 2. The discrepancy arises from the assumption that the low luminosity galaxies are optically thin in the far ultra violet. This would suppress the TIR flux of these galaxies and thus underestimate the SFR in the lower luminosity galaxies.

Synchrotron emission at these wavelengths originates from several different processes within galaxies, as such using it to measure of SFR is difficult due to the emission originating from sources other than star forming regions. Active galactic nuclei, AGN, and supernovae are by far the most dominant sources for this contamination. Though Genzel et al. [1998] concluded that ultra luminous infra red galaxies are powered by star formation rather than AGN.

Free-Free

Free-free emission tracing SFR can be measured using higher radio frequency data, 10-40 GHz, or using multifrequency data. Several papers have provided evidence for radio as a SFR tracer in regions, in the Galaxy [Mezger and Henderson, 1967], starbursts [Klein et al., 1988], and high resolution maps of nearby super star clusters in compact blue dwarfs [Turner et al., 1998, Kobulnicky and Johnson, 1999]. Evidence was also found in the nuclei of normal galaxies. [Turner and Ho, 1985]. This emission is not attenuated by dust like the Balmer lines are. Murphy et al. [2011] have compared 33 GHz data to infrared and Hα data and found a correlation between these different star formation tracers, demonstrating that 33 GHz radio emission can be used as a SFR tracer. However, the work also stated an issue whereby the SFR tracers relying on dust emission overestimate the SFR by a factor of ~ 2 compared to the free-free SFR. This was thought to be due to excess dust heating, so must be taken into account when using this method.

Radio emission between $\sim$ 10 and 90 GHz has a component attributed to rotating very small grains, that is often referred to as “anomalous dust emission”. The “anomalous dust” may complicate the use of free-free radio emission as a tracer of SFR. This is similar to synchrotron radiation. Though this emission can generally be discounted when using global scales and not local regions [Murphy et al., 2011].

Table 1.1: Table From Kennicutt and Evans [2012] Summarising the SFR Tracers

Band[b]	Age Range (Myr)[a]	References
FUV	0-10-100	Hao et al. [2011]
NUV	0-10-200	Hao et al. [2011]
TIR	$0-5-100^c$	Hao et al. [2011]
$H\alpha$	0-3-10	Hao et al. [2011]
24μm	$0-5-100^c$	Rieke et al. [2009]
1.4 GHz	0-100	Murphy et al. [2011]
2-10 keV	0-100	Ranalli et al. [2003]

[a] Second number is the mean age of stellar population whilst third number is the age below which 90% of emission is contributed
[b]Abbreviations: FUV, far ultraviolet; NUV, near ultra violet; TIR, total infrared.
[c] These are sensitive to SFR history; given for continuous star formation over the past 100Myr.

1.2.5 X-ray Emission

Ranalli et al. [2003]; have derived a calibration for 2-10 keV X-ray emissions. The 2-10 keV fluxes of galaxies have been shown to be correlated with the 1.4 GHz radio emission observed by Bauer et al. [2002] and also to be correlated with IR and radio emission stemming from nonthermal sources. This implies that X-ray emission can be used as a SFR tracer. However there could be issues with some X-ray sources being accretion discs of AGN though there is no dust obscuration.

1.3 Summary Of SFR Tracers

It is possible to use multiple tracers together to measure a more accurate SFR, this is done through the use of multi wavelength data. Table 1.1 summarises the SFR rate calibrated using several methods and the age range which can be measured, [Calzetti et al., 2007, Zhu et al., 2008, Kennicutt et al., 2009]. To work around the systematic errors associated with using IR luminosity as a SFR tracer, a combination of IR and UV or visible light can be used.

1.4 Dust Emission And It's Relation To Star Formation

Trumpler [1930] discovered the existence of interstellar dust through colour excess, where the absorbed light from distant stars was observed to vary with wavelength and not the distance to the source. Therefore the star appears to change colour. Through spectroscopic analysis as well as observed elemental depletion we have gained knowledge of the composition of this dust Li and Draine [2001].

The more generally accepted view is the dust is mainly composed of silicates with evidence of 9.7 μm Si-O and 18 μm O-Si-O bending mode absorption features in interstellar regions, and carbonaceous grains inferred from the strong interstellar absorption feature at 2200 $\AA$. Other elements such as Fe and Mg are also present in dust.

The IR spectrum of the MW and extragalactic objects is dominated by dust and PAH emission, with as much as half the total starlight being absorbed and reprocessed by these molecules [Lagache et al., 2005]. The dust grains can be parameterised by the wavelength dependant extinction curve into small and large grains. Large grains with radii a $>$ 0.025 μm, including the "classical" grains (a $\gtrsim$ 0.1 μm), which are primarily responsible for dust extinction and scattering in the optical wavelengths. Very small grains with a $<$ 0.025 μm, these are important contributors to the extinction of UV photons. [Li and Draine, 2001].

The emission from dust is dependant on both grain size and temperature. At wavelengths of 5-20 μm, emission from PAHs dominates. Emission at $\sim$ 20 μm is dominated by very small grains, which are emitting at temperatures of $\sim$ 100 K, this is referred to as hot dust. At wavelengths longer than 60 μm, colder emission ($\sim 20-30$ K) from larger dust grains dominates the spectra. The spectral energy distribution (SED) of the dust allows us to trace dust mass within the galaxy. We find areas of hot dust surrounding star forming regions, these are mostly very small grains. The large dust grains are mixed into the diffuse ISM and are heated through reprocessing near infrared and optical photons, from the evolved stars and

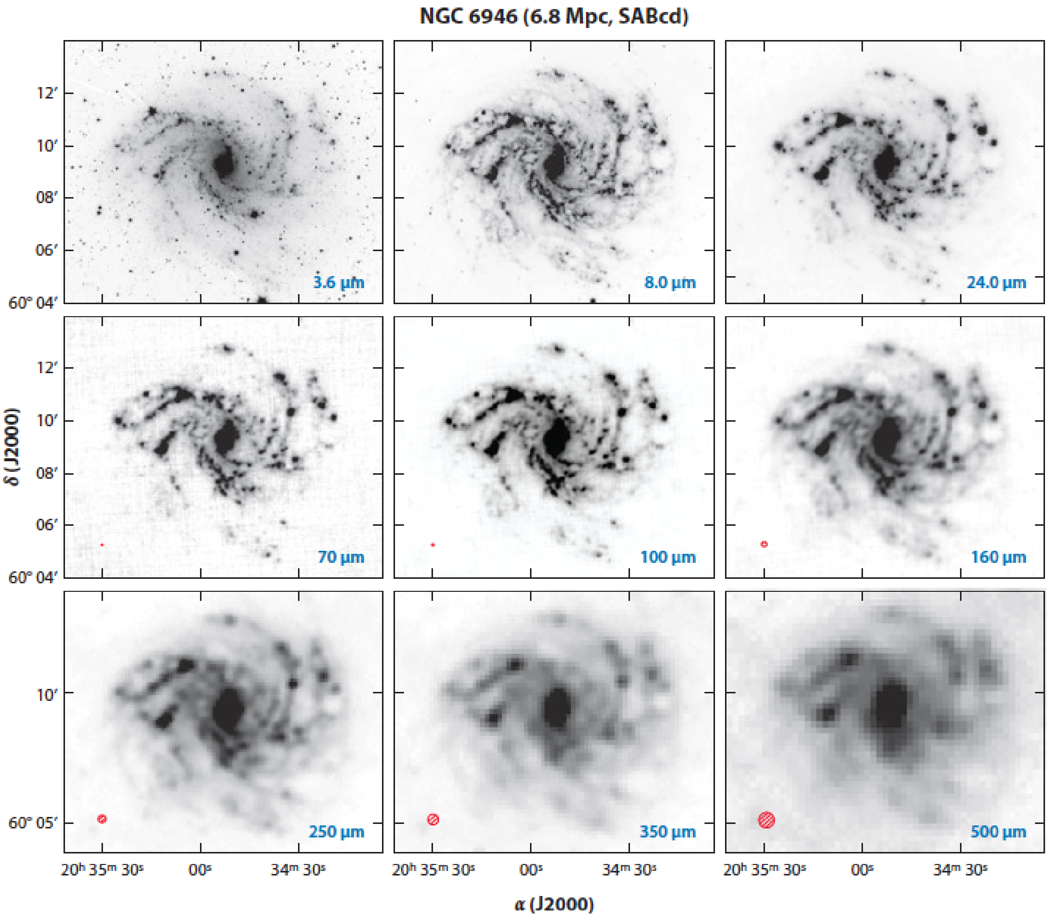

Figure 1.1: From Kennicutt et al. [2011], montage of images of NGC 6946 taken from *Spitzer*(SINGS) and *Herschel* KINGFISH) data sets. Top Panel: 3.6 μm, 8 μm and 24 μm emission dominated by stars, small PAH dust grains and hot dust grains heated by the young stellar population. Second Panel: 70 μm, 100 μm, and 160 μm, diffuse dust from larger grains in the ISM. Third Panel: 250 μm, 350 μm and 500 μm; tracing the coldest dust. This also traces out the majority of the dust mass within the galaxy. The FWHM of the *Herschel* images, is shown in the bottom left hand corner in red.

a component of the diffuse interstellar radiation field, ISRF, [Draine, 2003, Helou et al., 2004, Dale et al., 2005, Calzetti et al., 2007, Kennicutt and Evans, 2012]. We therefore see the majority of the dust mass in galaxies is traced through the emission at the longer wavelengths, originating from cold dust which by definition is larger in size and has a greater mass. The emission from the warmer component of the dust will underestimate the dust mass as it originates from a smaller fraction of dust mass, the very small grains.

The distribution of these different dust emission components are illustrated in Figure 1.1. With increasing wavelength, the increased contribution of the diffuse regions becomes apparent. The longer wavelength images are shown to have a greater contribution from the diffuse ISM when compared to the shorter wavelength IR images.

The dust is divided into hot and cold components and each component of the dust has a separate mechanism of heating sources, the hot and cold dust are described in Sections 1.5.3 and 1.5.2. The excitation mechanisms of the PAHs are more complex, and these are treated in Section 1.6.

1.5 Dust Emission Models

Current models of dust emission, for example Li and Draine [2001] best represent the progression from earlier models and considers the two different silicate and carbonaceous grains having different size distributions from a few Angstroms to larger grains of over 1 μm. The carbonaceous grains are distinguished by optical and physical PAH properties at small grain sizes. The larger grain sizes, with a > 100 $\mathring{A}$ can be assumed to have optical properties similar to graphite spheres. For simplicity each grain is modelled as sphere, avoiding complexities with polarisation. The carbonaceous grains can be treated such that there is a continuous emission spectrum.

1.5.1 Radiation Field

To model the IR emission of dust, realistic calculations of the excitation and de-excitation rates are needed. These are sometimes referred to as heating and cooling times. Dust grains are heated by absorbing starlight and cooled by emitting IR photons. The model assumes the dust grains sit in interstellar space far from any stars and are subject to a radiation field broadly based upon the solar neighbourhood interstellar radiation field (ISRF). This radiation field will have enhancement factors not attributed to the stellar population such as the cosmic background radiation. From this we can see how the dust emission varies when the intensity of the radiation field varies. The model for the radiation field is as follows,

$$u_\lambda = \chi_{MMP}\left[u_\lambda^{UV\odot} + \sum_{i=2}^{4} W_i \frac{4\pi}{c} B_\lambda T_i\right] + \frac{4\pi}{c} B_\lambda (2.9\ K) \tag{1.2}$$

the term χ_{MMP} in equation 1.2 represents the change in intensities of the ISRF relative to the solar neighbourhood radiation field. Note, where $\chi = 1$ corresponds to χ_{MMP} =1.23 where χ is the ratio of intensity relative to the [Habing, 1968] estimate at 1000 $\mathring{A}$; $u_\lambda^{\mathrm{UV}\odot}$ is the UV component; (W_2, W_3, W_4) = (10^{-14}, 10^{-13}, 4×10^{-13}) and (T_2, T_3, T_4) = (7500, 4000, 3000) K and are corresponding black body dilution factors. B_λ is the Planck function at temperature T and $\frac{4\pi}{c}$ B_λ (2.9 K) is the cosmic microwave background.

Figures 1.2 and 1.3 shows the emission from dust heated by radiation fields with varying intensities (where χ_{MMP} is modified) It is noted that for wavelengths $\lambda <$ 30 μm the emission seems to be relatively independent of intensity of the ISRF. This is due to the features at these wavelengths being dominated by single photon heating. This explains why increasing the intensity does not necessarily mean that the emission features will change in various radiation intensities.

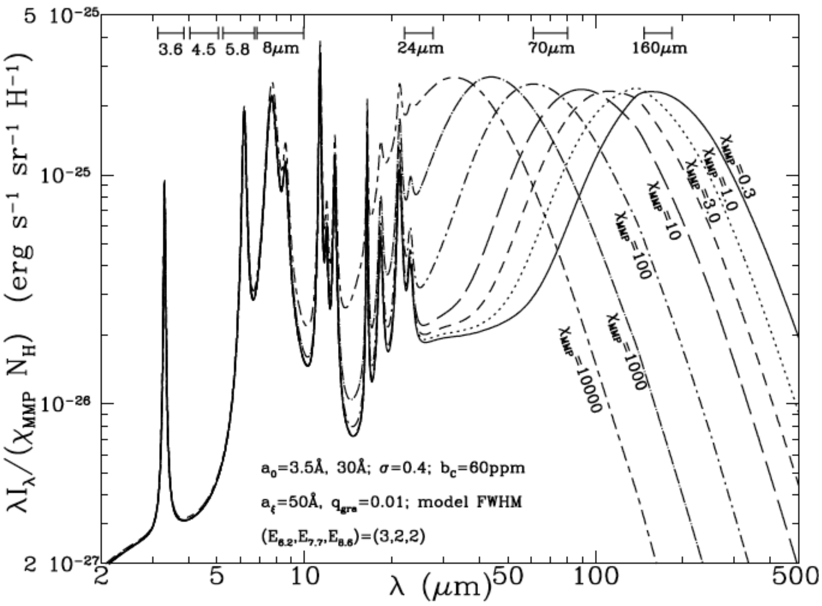

Figure 1.2: Figure from Li and Draine [2001] showing the IR spectra at various radiation intensities, $\chi_{MMP} = (0.3, 1.0, 3.0, 10, 100, 10^3, 10^4)$ Note that at shorter wavelengths, the shape of the spectra is dominated by PAH features and does not change much. The *Spitzer* IRAC and MIPS bands are shown in the top of the figure.

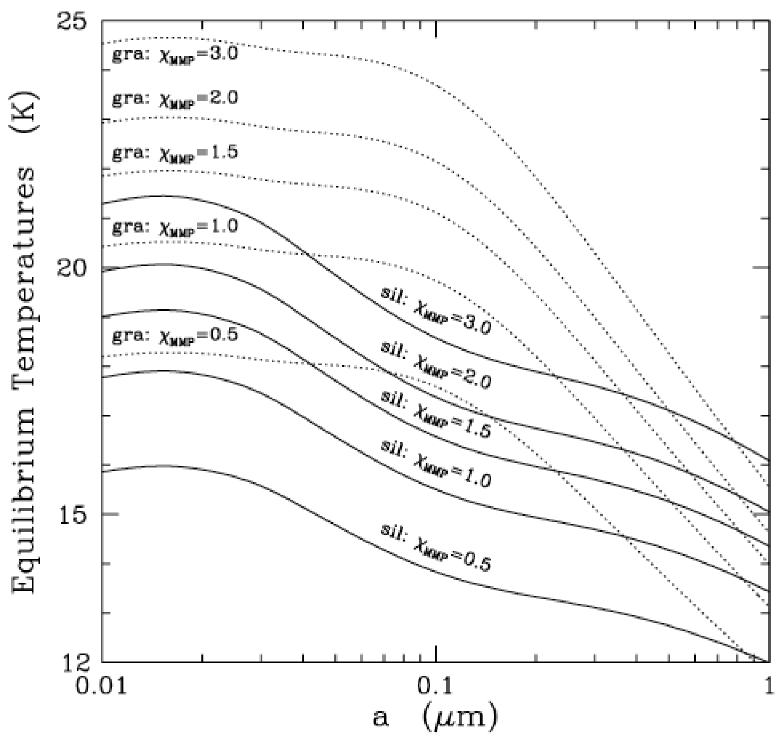

Figure 1.3: Figure from Li and Draine [2001] showing the equilibrium temperatures of silicate and graphite grains of different radii in environments with varying intensities of radiation fields.

1.5.2 Hot Dust

Heating of very small grains

First noted by Greenberg [1968] very small grains will undergo stochastic heating when illuminated by the ISRF. These are small enough grains that have vibrational energies $\langle E \rangle$ comparable or smaller than the energy of the photons in the ISRF. Much of the energy is re-radiated as IR. There are two approximations for modelling the emission: the "thermal-discrete" where each absorption and emission of a photon is handled as a discrete independent event, and "thermal-continuous" methods where only the emission is approximated as continuous.. Both assume that, at a given time, the grain has a "vibrational temperature" and that the de-excitation results in a thermal emission spectrum [Draine and Li, 2001].

In both these models the cooling time is much shorter than the heating time. As a result of this, the grain will quickly emit the IR photon. The size of the grain also effects the cooling time, since the hottest grains are also the smallest, meaning the small grains are able to cool completely between absorption events and the larger grains remain at a thermal equilibrium. For the smaller grains, most of the population will remain at or around their ground state energies. To include these small grains in the emission spectrum, integration across the grain population is necessary. This will lead to a higher than average temperature as the majority of the IR photons emitted will be at $\lambda \lesssim 30$ μm.

Within the SED of dust, there can be a population of cold dust occupied by very small grains which remain at a cooler temperature. This is due to some of these dust grains remaining at their ground state energies.

Hot Dust And Star Formation

Smaller grains with radii of $\lesssim$ 0.01 μm can be heated to temperatures of 100's K by a single photon. The dust will stay at this temperature for only a fraction of a second, and in this time the dust will emit at a shorter wavelength, $\sim$ 50 μm, the mid infrared (MIR) band. The emission from normal galaxies at the MIR is

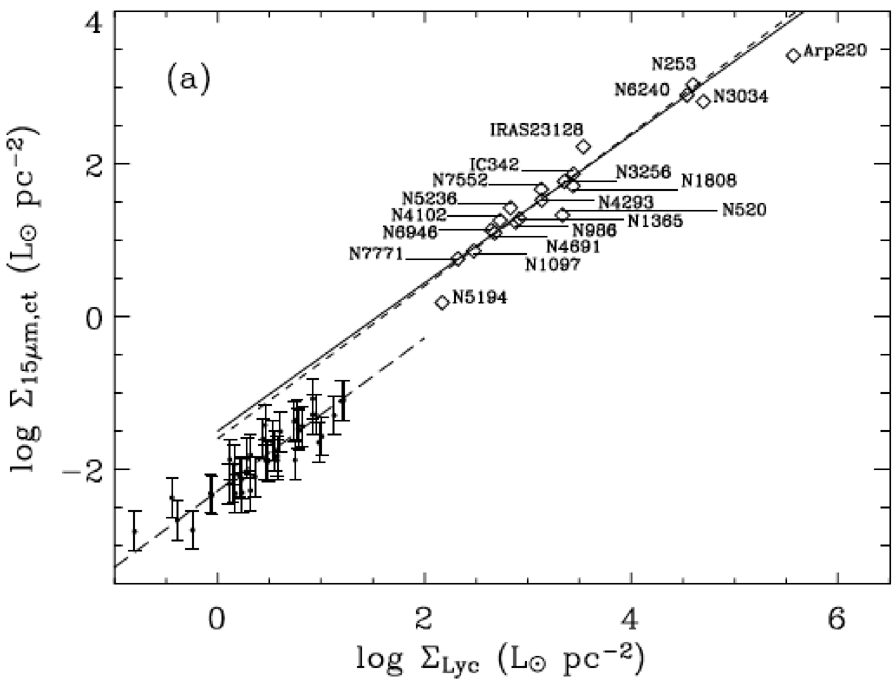

Figure 1.4: Figure from Forster Schreiber et al. [2004] showing 15 μm hot dust emission and Lyman continuum. The hot dust emission is shown to be an excellent SFR tracer due to the correlation with the Lyman continuum; a quantification of SFR itself.

dominated by thermal emission from these small grains [Desert et al., 1990].

It is important to be aware that not all starlight is absorbed by dust [Hirashita, 2001] so using IR emission by itself as a SFR tracer is not without some errors. It is possible that in galaxies, evolved stars will contribute to a significant fraction of dust heating. This will lead to the overestimation of SFR using IR tracers. A conversion factor can used to estimate the fraction of dust emission due to star formation, however this is not fixed and depends on the local stellar population. This has been calculated by Sauvage and Thuan [1992], Hao et al. [2011] to be approximately 1.3-2 between starburst galaxies and dormant galaxies. The use of this calibration and IR radiation by itself is best as a global tracer for star formation [Kennicutt et al., 2009].

ISO observations of NGC 300 by Helou et al. [2004] confirm dust emission at 4.5 μm is found in star forming regions, so this hot dust emission is most likely a good tracer of SFR. This dust emission is due to the heating of very small grains by the UV photons originating in star forming regions. Helou et al. [2004], Bendo et al.

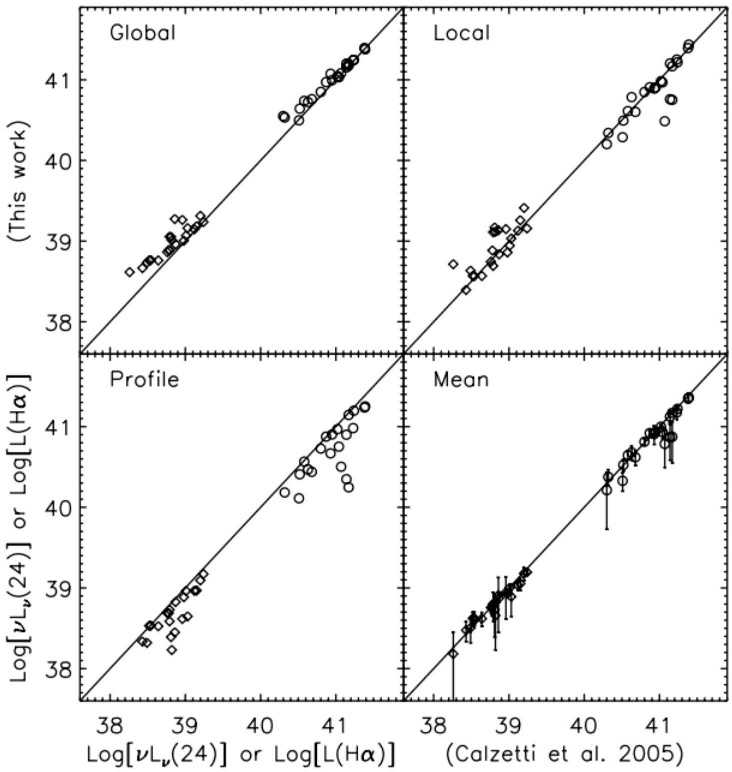

Figure 1.5: Figure from Prescott et al. [2007] showing measurements of regional luminosities of $\nu L_\nu(24)$ (circles) and L (Hα) for 3 different techniques used in the analysis. Also shown is a comparison to Calzetti et al. [2005]

[2006, 2008] describe how dust detected at 24 μm is seen within rings centred around H II regions. Helou et al. [2004] go on to correlate this with the regions traced by Hα. Werner et al. [2004] and Forster Schreiber et al. [2004] have also carried out diagnostics on 15 μm very small grain dust emission, see Figure 1.4. Gordon et al. [2008] using *Spitzer* data, have been able to study aromatic features at ~ 8 μm and concluded these correlate strongly with the ionization index.

The MIR luminosities are commonly used waveband for calibrating the mid infrared SFR tracers, Zhu et al. [2008], Rieke et al. [2009], Kennicutt and Evans [2012] have correlated 8 μm and 24 μm with 70 and 160 μm as well as 8 μm and 24 μm with Hα as well. They find that when using Hα correlated data, the results show that these can be used as good SFR tracers, provided that the $H\alpha$ is corrected for dust extinction. Calzetti et al. [2007] have correlated 24 μm with Paα (1.8765 μm). Prescott et al. [2007] show a correlation between the 24 μm emission and Hα star formation tracer. This is also similar to the conclusions reached by Calzetti et al.

[2005]. The correlations are shown in Figure 1.5.

1.5.3 Cold Dust

Thermal Equilibrium Temperatures of Large Grains

The large grains with radius of $\approx$ 0.1μm will emit longwards of 60 μm. These maintain a constant temperature upon balancing the absorption and emission of photons. The cooling time and heating time of the dust grains are of a similar length. The grains will rise to a particular temperature and remain at this equilibrium in the presence of a continuous ISRF such that,

$$\int_0^\infty C_{abs}(a,\lambda) c u_\lambda \,\mathrm{d}\lambda = \int_0^\infty C_{abs}(a,\lambda) 4\pi B_\lambda(\bar{T}) \,\mathrm{d}\lambda \tag{1.3}$$

where $C_{abs}(a,\lambda)$ is the absorption and emission cross section for a grain of size a at a wavelength λ, c is the speed of light, B_λ(T) is the Planck function at temperature T and u_λ is the energy density of the radiation field. This is also illustrated in Figure 1.3.

Cold Dust Profiles

Using IRAS data, the consensus on how this dust is heated, was different to the picture we have now. Buat and Xu [1996] concluded that star formation could be responsible. Sauvage and Thuan [1992] postulated evolved older stars contribute to cold dust heating and star forming regions were not the principle mechanisms to drive this cold dust emission. Roussel et al. [2001] show a weak relationship between the total far infrared flux and star formation tracer Hα in Figure 1.6 These results are not spatially resolved so the dusk and nuclear contributions cannot be identified.

Thanks to *Spitzer* and more recently *Herschel* data, models on the origins of cold dust have been refined. Calzetti et al. [2010] show from *Spitzer* data that increasing contributions to the heating of cold dust are due to older stellar populations. Bendo et al. [2012a], Smith et al. [2012] using *Herschel* data, both show that for dust emission at wavelengths longer than 160 μm, contributions to heating are mainly

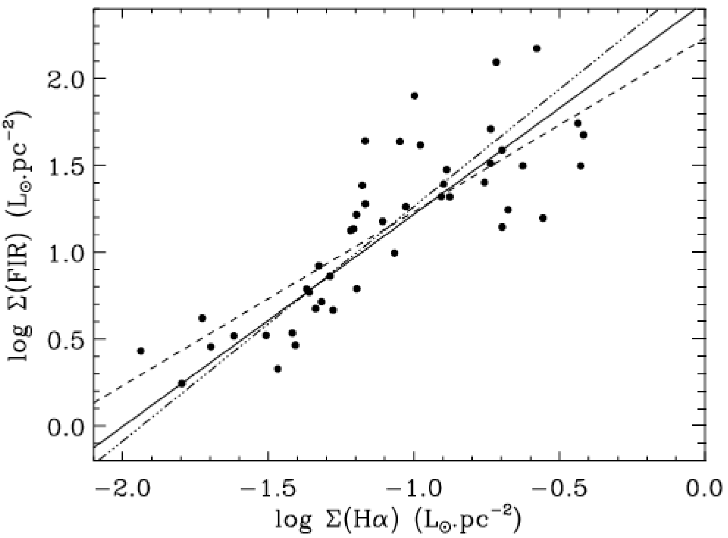

Figure 1.6: [Roussel et al., 2001] relationship between Hα and FIR size normalised fluxes for a sample of nearby spiral galaxies observed using ISOCAM. The dashed line represents linear correlation, the dot-dashed line is the least square fits, solid line the least absolute deviation fit. with slopes $1.35^{+0.50}_{-0.34}$ with 3 σ interval"

from older stellar populations. [Boquien et al., 2011, Groves et al., 2012] also state the temperature of the cold dust is constrained by these older stars. The advantages of *Herschel* for the longer wavelength IR studies are the improvements in resolution compared to previous generation telescopes. Figure 1.7 shows star forming regions traced out from Hα and stellar populations and dust emission surface brightness ratios from the 70 − 500 μm images. The surface brightness ratio of the dust at 250/350 and 350/500 μm indicates a radial dependance for the cold dust with the most intense emission originating in the nucleus. The 70/160 μm and 160/250 μm show some similarities to the star forming regions traced out by Hα. It is clear that colder dust does not trace star formation, and is heated by the evolved stellar population.

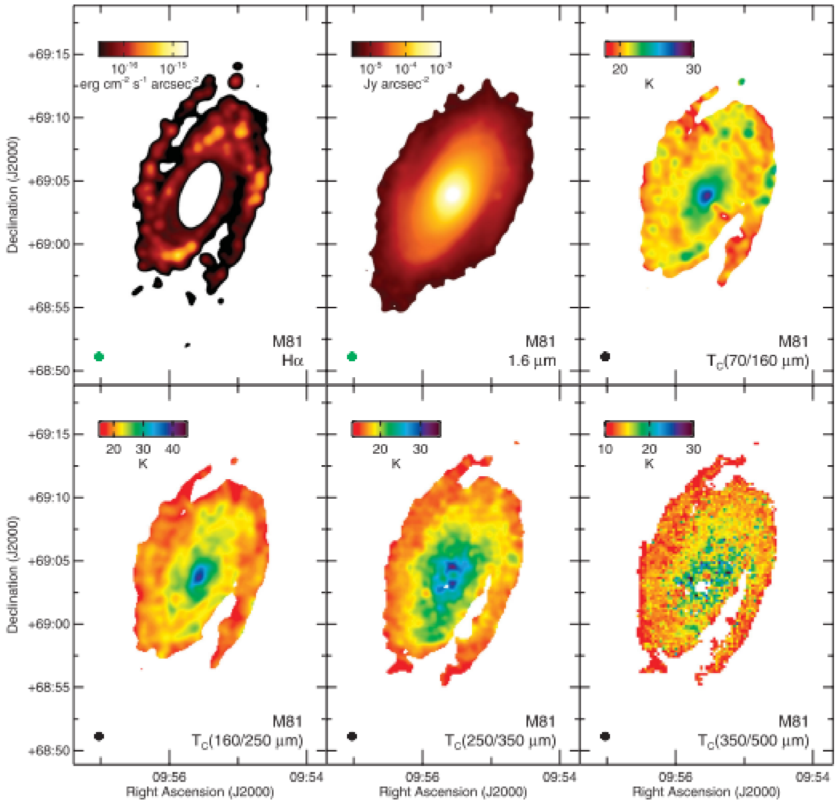

Figure 1.7: Taken from Bendo et al. [2012a], shows a composite colour map showing emission for M81. The 70/160 μm ratio and 160/250 μm ratio follow the Hα indicating that the dust emission in these bands is linked to star forming activity. Longwards of 250 μm there is a clear radial dependance where the dust is heated by the older stellar population in the bulge of the galaxy.

1.6 Polycyclic Aromatic Hydrocarbons

1.6.1 Characteristics, Properties and Abundance in the Interstellar Medium

Polycyclic Aromatic Hydrocarbons (PAHs) are large carbon based molecules containing about 50 carbon atoms arranged in a honeycomb structure of fixed six-membered aromatic rings with adjoining hydrogen atoms. Each carbon atom is bonded to another C atom or H atom through three strong covalent bonds (sigma bonds), resulting in a planar structure. The fourth electron of each C atom is in a p orbit to form delocalized clouds above and below the plane of carbon atoms. This results in molecules with 2D structure where three electrons are bound in the sigma bonds and each fourth C electron is free to orbit the molecule. The 2D structure of these molecules leads to stacking of PAH clusters bonded by Van der Waals forces. High stability of these molecules is attributed to the structure of the C atoms and electrons orbiting the molecules, [Tielens, 2008].

PAHs are abundant in the ISM (Interstellar medium). The number ratio of PAHs to hydrogen is 10^{-7}, [Tielens, 2008]. They influence the structure and evolution of the ISM, due to domination of the heating of neutral gas and the ionization balance of molecular gas and dust within the ISM. Hence they will influence the phase structure of the ISM as well as the ion-molecule chemistry that builds up the gas phase species within the ISM. Since these molecules are known to influence the ambipolar diffusion processes that set the stage for star formation as well as appearing abundant in massive star forming regions, it is thought that these can be used to trace recent star formation. PAH are thought to be excited by UV photons from massive young stars [Tielens, 2008].

1.6.2 IR and Excitation Mechanisms of PAH

The emission of PAHs mainly falls in the infrared. PAH emission features, including those at 3.3, 6.2, 7.7, 8.6 and 11.3, 12.7 and 16.4 μm, are produced by stretching, vibrational transitions and either in plane or out of plane bending, [Allamandola et al., 1989, Tielens, 2008]. There are weak PAH features interspersed amongst the stronger features up to 18.9μm. Many of these features show a sensitivity to physical conditions. This results in a shift in position or changes in the widths and structure or substructure.

As the nature of the C-C and C-H bonds are different, it is likely that different intensities in the emission features are seen. The PAH; 3.3 μm feature is due to CH stretching modes, pure C-C stretching modes generally fall between 6.1-6.5 μm. Longwards of 6.5-8.5 μm lie vibrations at emission lines involving a combination of CC stretching and CH in plane bending modes. CH in-plane wagging modes lie within 8.3- -8.9 μm. The 11-15 μm bands are CH out-of-plane modes. Wavelengths longer than 15 μm are more molecule specific, characterised by in-plane and out-of-plane ring bending motions of the carbon hexagonal structures [Tielens, 2008]. Figure 1.8 shows the different features and their associated wavebands. The relative intensity of the feature is dependant on the degree of ionization as well as the relative strength between the CC and CH modes. There are also various side groups to PAHs. Most of them contain aromatic hydrogen and have features that are sometimes overlapping with PAH molecules.

The most commonly observed PAH feature is the C-C stretching at 7.7 μm, it has been studied by Calzetti et al. [2005, 2007], Prescott et al. [2007], this is because it lies in a band not dominated by either hot dust emission or emission from stellar sources.

1.6.3 Relation to Hot Dust

Roussel et al. [2001] suggest a relationship where the PAHs are spread uniformly across the ISM and as such there is not much evidence to find hot dust and PAH emission originating from the same localised regions. The PAH features at around 8 μm are related to 24 μm hot dust emission, from very small grains, VSG. Forster Schreiber et al. [2004] look at the VSG (15 μm) to PAH emission (5-8.5 μm) and find this increases when moving from the disc to areas of star formation to areas of intense

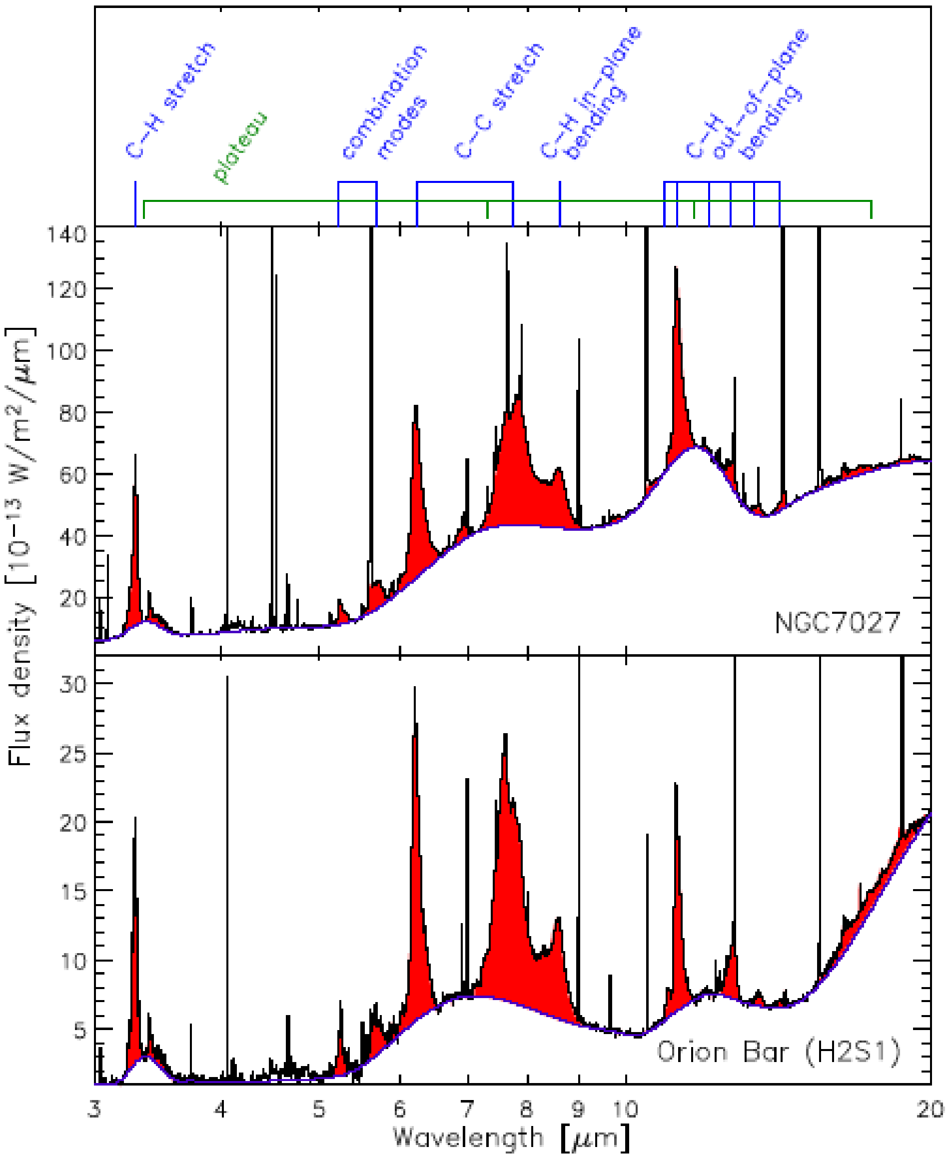

Figure 1.8: From Tielens [2008], Adapted from Peeters et al. [2002]. The spectrum from two objects using ISO data, the individual features are clear and labelled.

star formation. This indicates the PAHs are destroyed by the intense radiation field, or could be shielded by the dust so they see fewer UV photons. Peeters et al. [2004] show a strong correlation between PAH 6.2 μm/FIR and 6.2 μm IR continuum.

Helou et al. [2004] have also found a relation between the PAH and hot dust emission, on local scales. The PAHs are found in a shell around the star forming regions. Hot dust emission originates from within these regions, Figure 1.9. This demonstrates that PAHs break down in the presence of strong UV radiation. Bendo et al. [2006], and Bendo et al. [2008] also show the 8 μm emission emanates from rings centred on H2 regions.

Bendo et al. [2006, 2008], Gordon et al. [2008] find PAH features at around 8 μm could be related to 24 μm hot dust emission in the diffuse ISM. This relationships shows the PAH 8 μm feature to be suppressed in the regions where 24 μm emission is strongest. Calzetti et al. [2005] find the 8 μm emission is under luminous in areas with strongly ionizing photons, and over luminous in the diffuse regions of M51. These show the 8 μm emission is not correlated with the hot dust emission centred around star forming regions, and is more closely associated with the diffuse medium. These suggest the PAHs have complex heating mechanisms, not just the UV radiation. Possible reasons for the shell like structures and PAH inhibition in regions where the 24 μm emission is strong could be due to the changes in PAH or the 24 μm dust emission. It is likely the dust emitting at 24 μm is more stable than the PAHs in the intense ISRF, found in regions where the SFR is high.

1.6.4 Relation to Cold Dust

Haas et al. [2002] show a relationship between the 850 μm cold dust emission and the 7.7 μm PAH line. This suggested PAHs are spread out across the ISM, and are excited by the ISRF. This inter stellar radiation field is thought to be strong enough to drive PAH emission, and thus UV photons from local star forming regions were not thought to contribute to the majority of PAH emission. This hypothesis makes the assumption that though PAH emission may not locally be driven by star formation, this is still a way to measure a global SFR for the galaxy as a whole

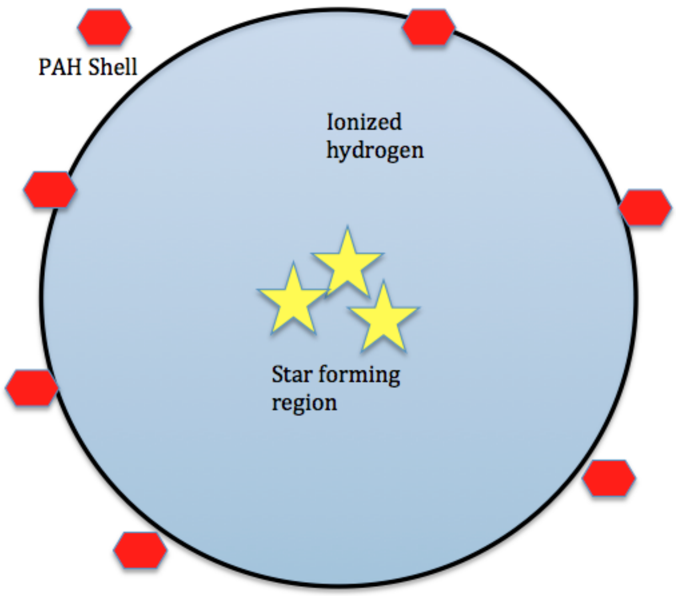

Figure 1.9: PAH shell formed around a star forming region within a Strömgren sphere of ionized Hydrogen

as the SFR is high enough to power this ISRF, [Zhu et al., 2008, Kennicutt et al., 2009].

Bernard-Salas et al. [2007] stated that PAH emission was weaker in the presence of a strong ISRF and the explanation for this was the photo disassociation of PAHs. Bendo et al. [2008] have also shown a relationship between the PAH emission at 8 μm and cold dust at 160 μm. This scales well over distances of $\sim$ 2 kpc. This shows the PAHs are good tracers of cold dust and diffuse ISM material, able to trace large scale structure within the galaxy. This suggest the PAHs are able to trace the strength of the ISRF, and therefore are best suited to tracing the diffuse dust in the ISM. Most likely they could not be used as a tracer for SFR.

It is possible for galaxies to evolve through material spiralling in towards the centre and star formation to take place in the central disc [Kormendy and Kennicutt, 2004]. If the rate of mass accretion in the centre of the galaxy were to be higher than the SFR, a gas cloud will form. Regan et al. [2006] have found that a radial distribution similar to this theory with strong profiles of both CO and 8 μm PAH emission within the central bulge. Vlahakis et al. [2013] show a correlation between the PAH emission and CO J=3-2 emission from molecular clouds in M51, with

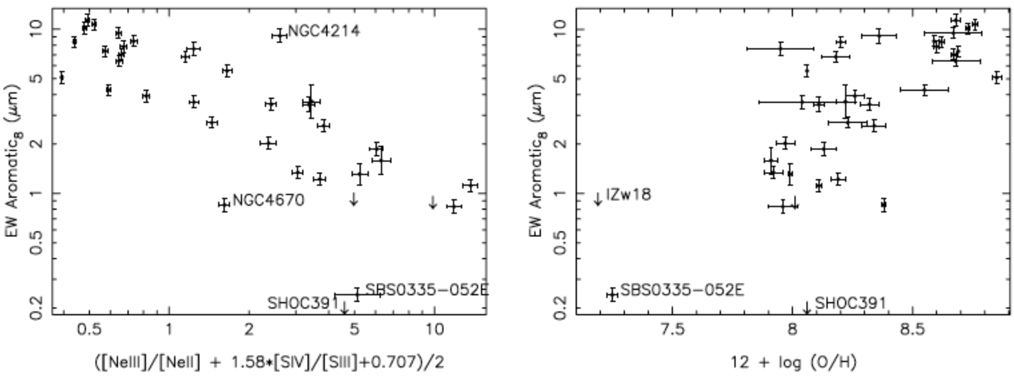

Figure 1.10: Figure from Engelbracht et al. [2008] PAH 8 μm plotted against a function of ionizing radiation (left) and metallicity (right).

the same radial dependancy. An excess of molecular gas within the central bulge is evidence for star formation, and as such it can be inferred that PAH emission occurs where star formation is present.

1.6.5 Relation To Metallicity

PAH emission was thought to be related to the metallacity of the galaxy/region. The correlation is best described by Engelbracht et al. [2005, 2008], Gordon et al. [2008]. This relationship is based on the low metallicity galaxies having little diffuse dust and as such the PAH are exposed to high intensity radiation fields which causes their dissociation. As such it is airing on the side of caution to use them as a tracer for SFR, and Calzetti et al. [2007] also show the same relationship between 8 μm PAH metallicity and therefore as this is such a strong dependance, a calibration for using these as SFR tracers remains yet to be calculated. They do conclude that the PAH emission does show a strong correlation with the ionizing rate. Figure 1.10 shows the stronger relation to ionization and not to metallicity. This is due to the low metallicity weakening the PAH emission due to there being less dust in the ISM. This allows the UV photons to destroy the PAH molecules, through photodissociation.

Spiral galaxies in the local group are metal rich. This is due to generations of star formation producing these heavier elements. Nearby low metallicity galaxies exhibit properties of early low metallicity galaxies and can be studied to simulate likely conditions in these high z galaxies [Kunth and Östlin, 2000]. The spectra of low metallically galaxies differs from the high metallicity and higher luminosity galaxies in the IR, with weak PAH emission and large dust grain emission [Calzetti et al., 2000, Houck et al., 2004].

1.7 Goal Of The Thesis

As has been shown by Genzel et al. [1998], Helou et al. [2004], Bernard-Salas et al. [2007], there are correlations between the IR emission of PAHs and the traces of massive young stars; ionizing rate of UV photons. More recent work by Bendo et al. [2006, 2008], Calzetti et al. [2007] has shown little correlation with 8 μm emission associated with PAHs and 24 μm hot dust emission, a known star formation tracer. The authors have shown the 8 μm emission is not correlated with the 24 μm emission on local scales.

Bendo et al. [2008] have argued that whilst the 8 μm PAH emission can be correlated with the 160 μm cold dust emission, there is still no case for using these as SFR tracers due to the lack of correlation where known star forming regions are. Haas et al. [2002] show a relation to 850 μm, this does not support theories showing PAH emission can be a reliable tracer of SFR. Draine et al. [2007] show PAH molecules break down in the presence of strongly ionizing photons, which are thought to originate in star forming regions.

As well as trying to constrain the use of PAHs as star formation tracers, we want to build on work by by Haas et al. [2002], Bendo et al. [2008, 2012a]. This will involve looking at the relationship between PAH emission and hot dust, and PAH emission and cold dust. The source of heating of the dust will be discussed with more emphasis on heating on PAHs than cold and hot dust.

This analysis will build on these foundations and further analyse PAH emission from galaxies. We have chosen three nearby face on galaxies, M83 (NGC 5236), M51 (NGC 5194, NGC 5195) and NGC 2043. Each of these have an optical disc larger than 10 arc minutes across. This will allow us to resolve the spatial differences in the emission components. Data from both *Spitzer* IRAC and MIPS as well as *Herschel* PACS and SPIRE instruments at the following wavelengths will trace out different components of emission from these galaxies; 3.6 μm trace starlight; 8 μm traces PAH emission; 24 μm traces hot dust; 160 and 250 μm trace out cold dust.

Chapter 2

Sample Selection

2.1 Sample Selection

The sample galaxies selected for analysis are NGC 2403, M51 (NGC 5194/5) and M83 (NGC 5236). These were all observed with *Herschel* as part of the Very Nearby Galaxies Survey (P.I.: C. Wilson), a *Herschel*-SPIRE Local Galaxies Guaranteed-Time Programs that performed observations of 13 nearby galaxies. This subset was selected for analysis because they are all nearby (< 10 Mpc) spiral galaxies that appear face-on (with inclination from face on $\lesssim 60^o$) and that have major axes > 10 arcmin.

These properties allow us to measure the local as well as global emission from the dust, including the PAHs as well as the star forming regions and total stellar population. Details of these three galaxies are given in table 2.1.

It is important to choose galaxies that are face on as this represents the best methods of resolving detail locally within the galaxy, rather than analysing the galaxy as a whole. The size of the major axis, $>$10 arcmin allows these regions to be resolved to levels of details in the kpc range. With the rebinned pixels each being 18 arc seconds across, the furthest galaxy from us is 8.4 Mpc gives the size of these regions to be of the order of hundreds of kiloparsecs.

Table 2.1: Table listing the properties of the sample galaxies.

Name	RA & Dec (J2000)	Hubble Type[a]	Distance (Mpc)	Size of Optical disc (arcmin)[d]	Position Angle of Optical disc[d]
NGC 2403	07 36 54.5: +65 35 58	SAB(s)cd	3.2 ±0.3[c]	21.96x12.3	127
NGC 5195 (M51a)	13 29 53.3 +47 11 48	SA(s)bc pec	8.4 ± 0.6[b]	11.2x 6.9	170
M83	13 37 00.3: -29 52 04	SAB(s)c	4.5± 0.2[c]	12.9x11.3	0

[a] Data are the D_{25} isophote taken from de Vaucouleurs et al. [1991]
[b] Data are from Feldmeier et al. [1997].
[c] Data for M83 and NGC 2403 are taken from Freedman et al. [2001]
[d] Data taken from de Vaucouleurs et al. [1991] and are given as degrees from north through to east.

2.1.1 M51

M51 is composed of NGC 5194 and an interacting smaller companion galaxy NGC 5194, it has a Hubble type SA(s)pc [de Vaucouleurs et al., 1991]. NGC 5194 is of grand design with two major spiral arms, within which are the star forming regions spread out in localised clumps. In blue light, there are strong dust lanes towards the inside of the galaxy, and shows tidal features to the north, east and west, possibly due to the interaction. The galaxy is not asymmetric, but shows symmetry in the I-band. The stellar background is very strong even in the dense dust lanes, where the intense starlight is not attenuated by dust. The nuclei of both NGC 5194 and NGC 5195 are bright in the 24 μm.

The galaxy is the subject of many studies, from kinematics [Tully, 1974] and tidal interactions [Noble et al., 2006], to the interactions within the ISM [Koda et al., 2009]. Star formation and HII regions are well studied in this galaxy [Bastian et al., 2005, Bianchi et al., 2005, Calzetti et al., 2005, 2007, González-Lópezlira et al., 2013].

Figures 2.1 to 2.5 show the 3.6, 8, 24, 160 and 250 μm data for M51 used for analysis. The images are shown before the data preparation steps in section 4.1 were applied.

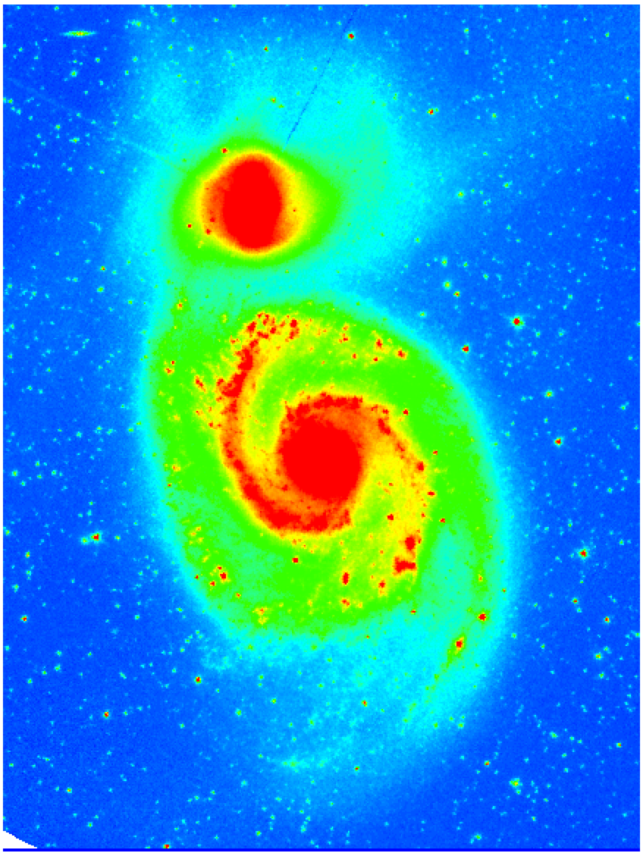

Figure 2.1: 3.6 μm data for M51.

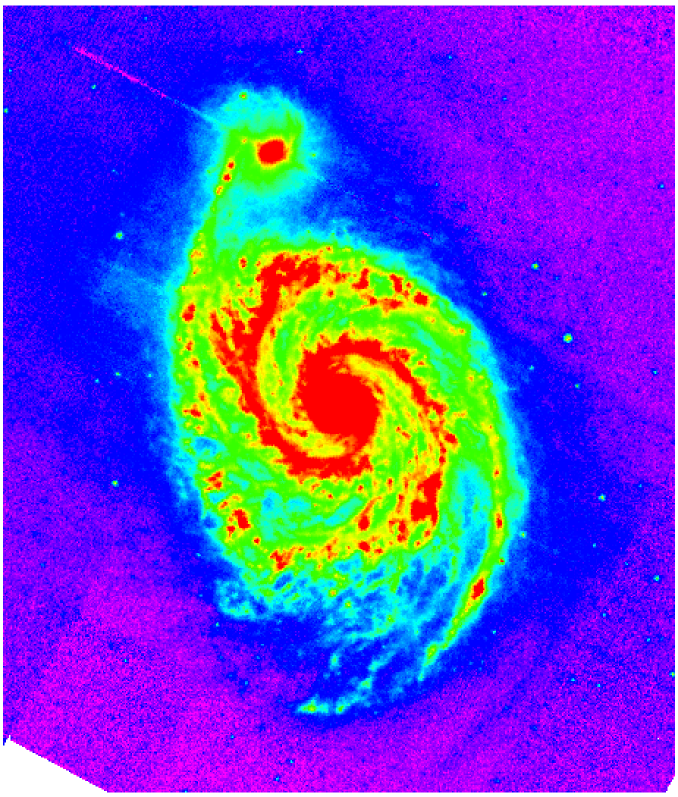

Figure 2.2: 8 μm data for M51.

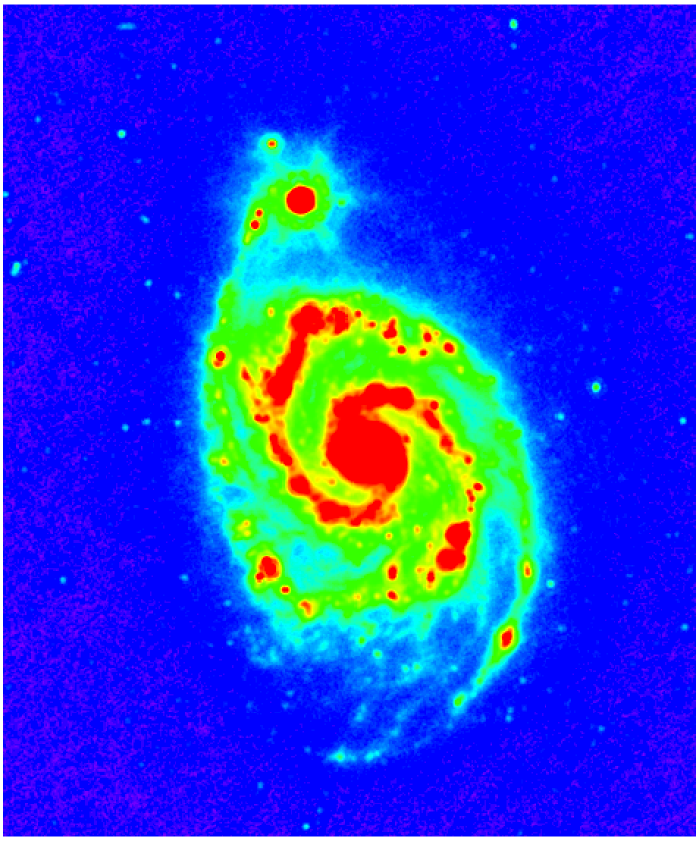

Figure 2.3: 24 μm data for M51

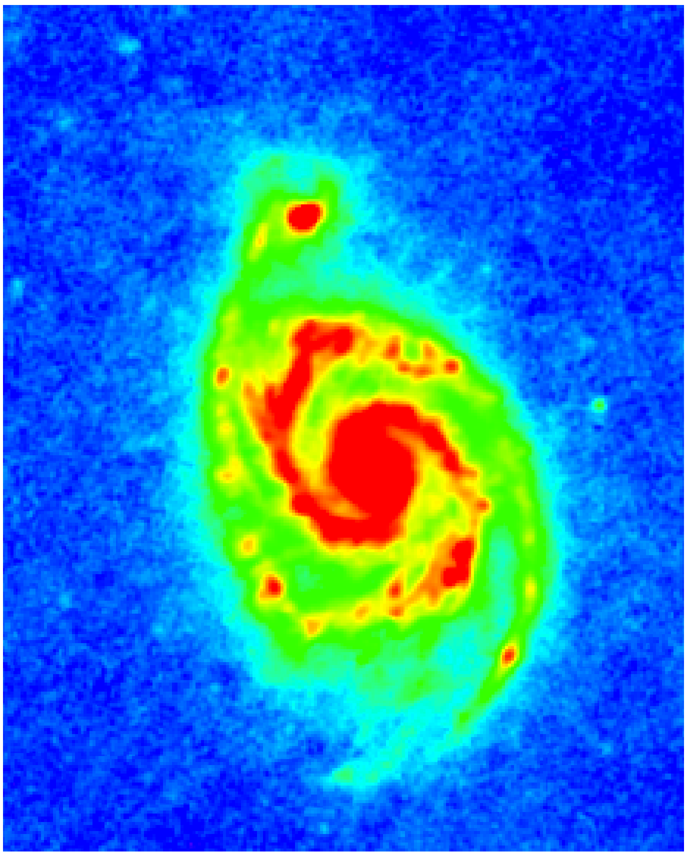

Figure 2.4: 160 μm data for M51.

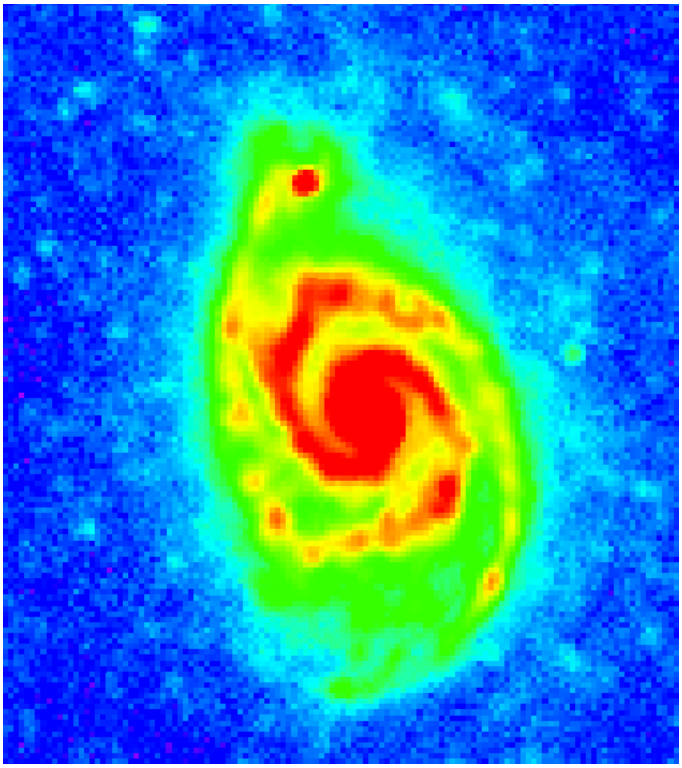

Figure 2.5: 250 μm data for M51.

2.1.2 M83

M83 (NGC 5236) is a SAB(s)c classification de Vaucouleurs et al. [1991], with a bright star burst nucleus [Bohlin et al., 1983]. It is a face on grand design spiral type galaxy with strong dust lanes and a well defined two arm spiral pattern. The structure in the outer disc shows considerably complex with various dust structures branched off the main spiral arms, this is typical behaviour of other spiral galaxies.

M83 is very well studied, being the subject of dozens of research papers. The starburst nucleus is of particular interest as a double circumnuclear ring was discovered by Elmegreen et al. [1998]. Other studies have focused on the young star clusters within the nucleus, for example Harris et al. [2001]. The molecular gas structures are very well studied [Lundgren et al., 2004, Heiner et al., 2008]. The dust heating processes have also been studied, [Bendo et al., 2012a, Boquien et al., 2011, Foyle et al., 2013]. Star formation in the galaxy is well known [Thilker et al., 2005, Lundgren et al., 2008].

Figures 2.6 to 2.10 show the 3.6, 8, 24, 160 and 250 μm data for M83 used for analysis. The images are shown before the data preparation steps in section 4.1 were

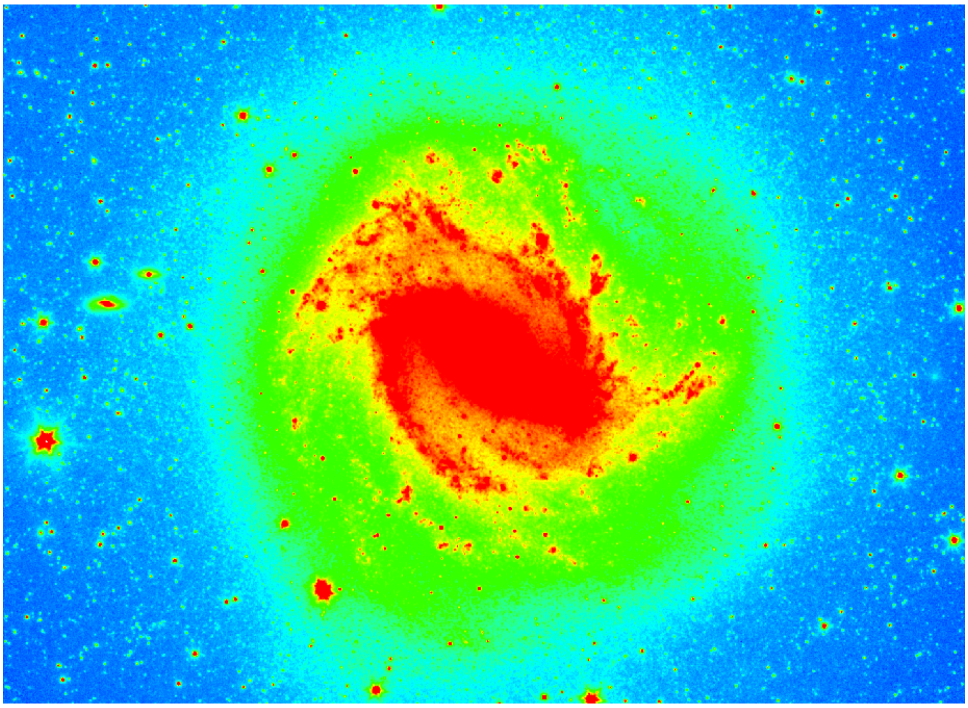

Figure 2.6: 3.6 μm data for M83.

applied.

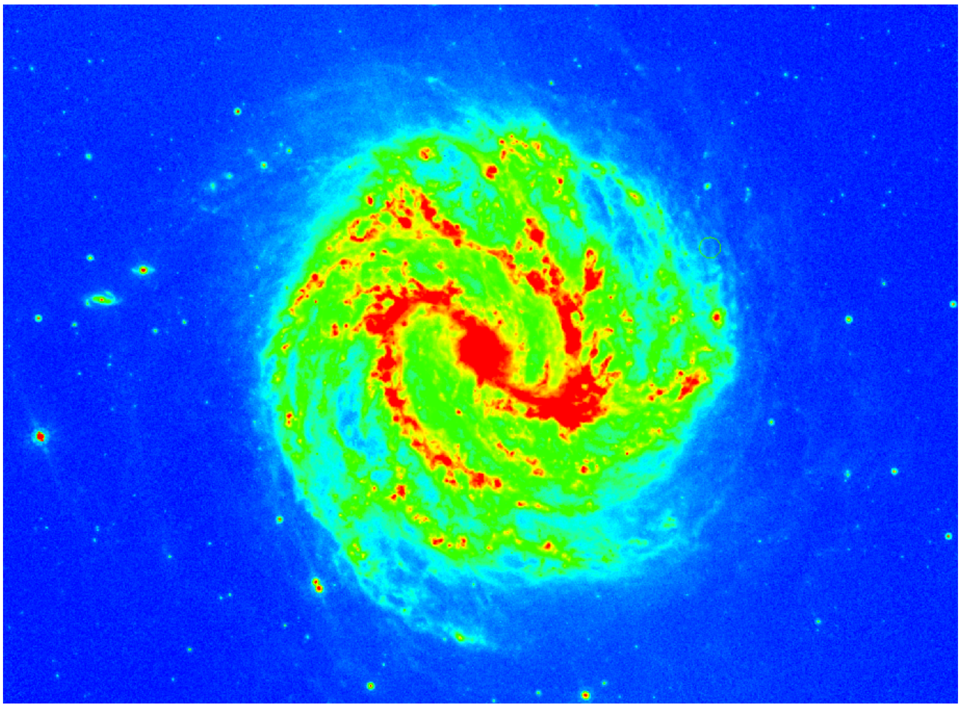

Figure 2.7: 8 μm data for M83.

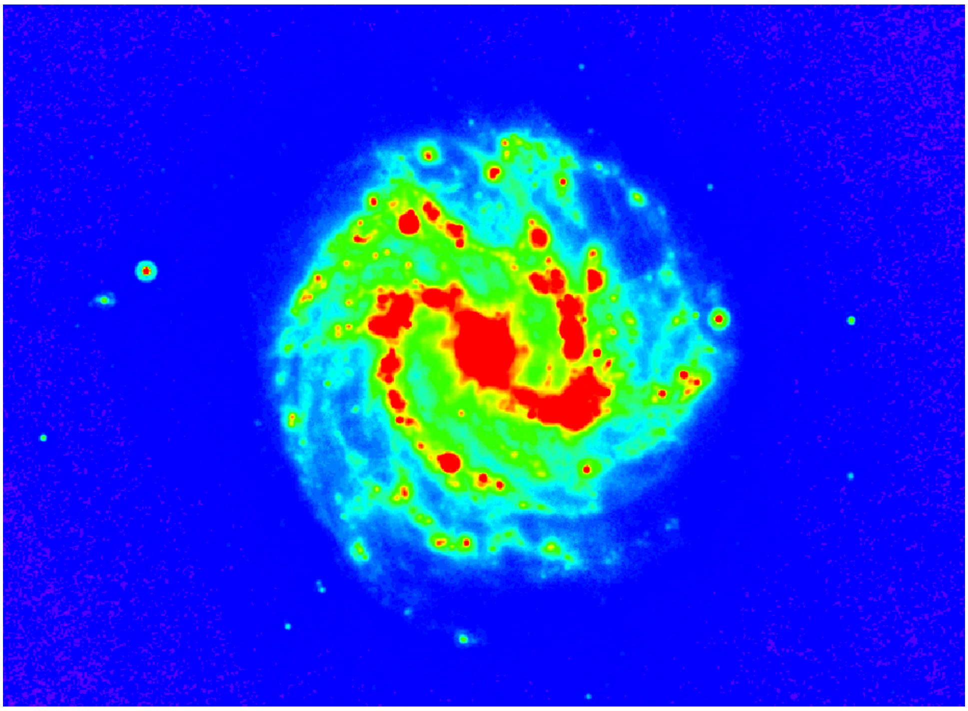

Figure 2.8: 24 μm data for M83.

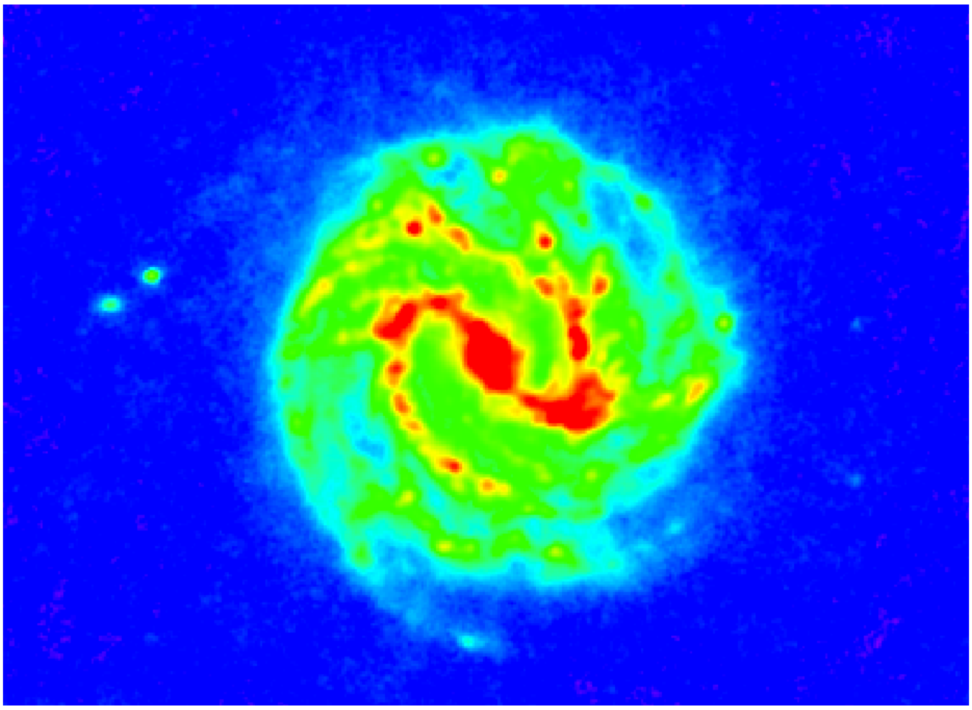

Figure 2.9: 160 μm data for M83.

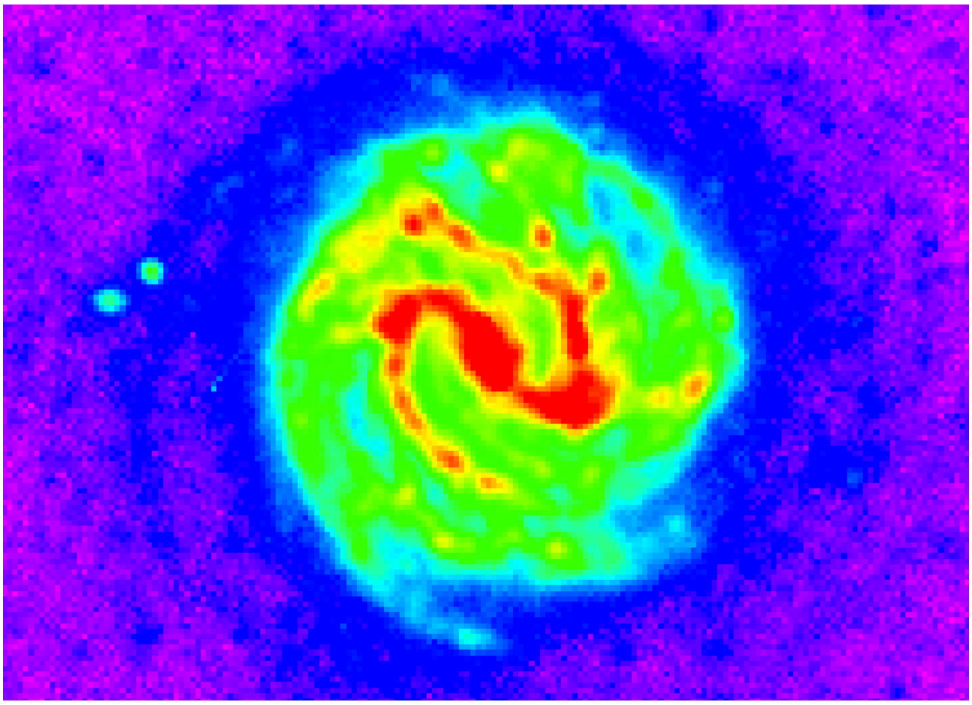

Figure 2.10: 250 μm data for M83.

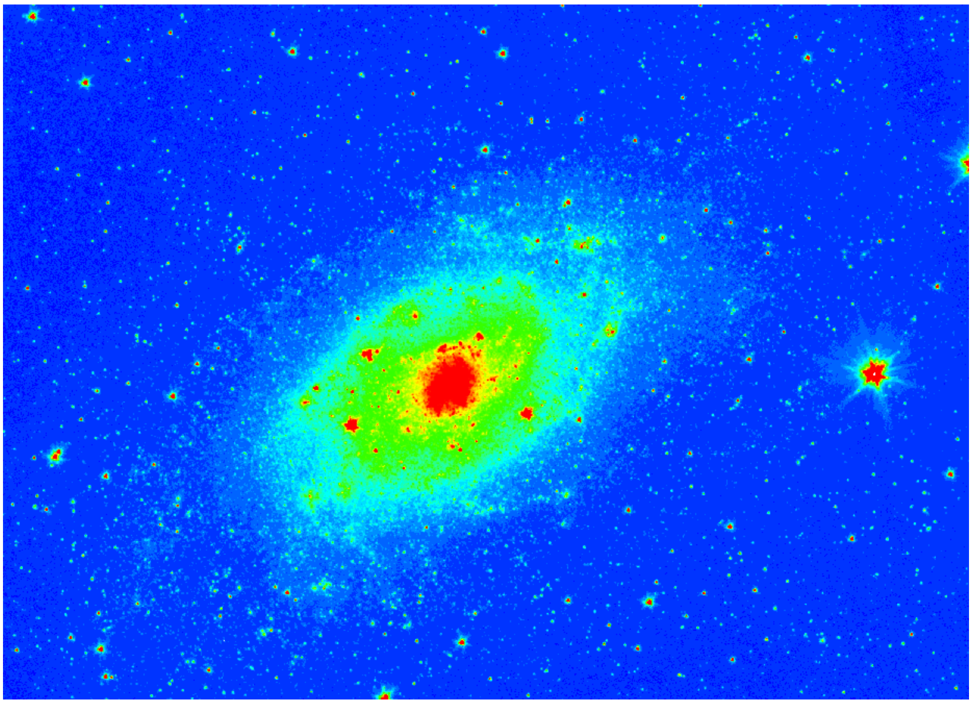

Figure 2.11: 3.6 μm data for NGC 2403.

2.1.3 NGC 2403

NGC 2403 is a flocculent spiral galaxy with no clear bulge of Hubble type SAB(s)cd de Vaucouleurs et al. [1991]. There are some dust lanes, but these are not particularly evident in wavelengths of around 8-250 μm. We see weakly defined spiral arms, as such there are multiple off centre star forming regions, this disorganised structure makes analysis of radial profiles of interest. The brightest region in the 24 μm tracing star formation, is to the northeast of the centre. These regions are shown in the 24 μm images as well as in Bendo et al. [2008].

NGC 2403 is well studied as it is a bright nearby galaxy. The colour / magnitude of the bright stars within the galaxy are very well known, [Sandage, 1984]. Very luminous variable stars,Cepheids within the galaxy are well studied, so the distance towards it is very well known. The dust heating and surveys of infrared light [Bendo et al., 2010, 2012a], as well as molecular gas content and structure are also studied [Thornley and Wilson, 1995].

Figures 2.11 to 2.15 show the 3.6, 8, 24, 160 and 250 μm data for NGC 2403 used for analysis. The images are shown before the data preparation steps in section 4.1 were applied.

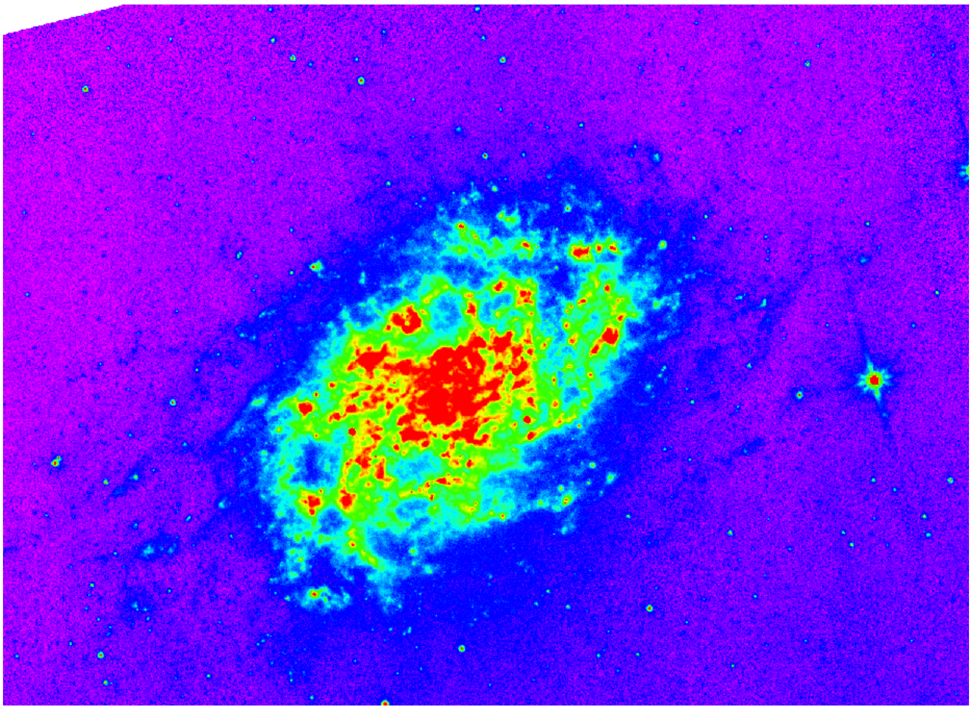

Figure 2.12: 8 μm data for NGC 2403.

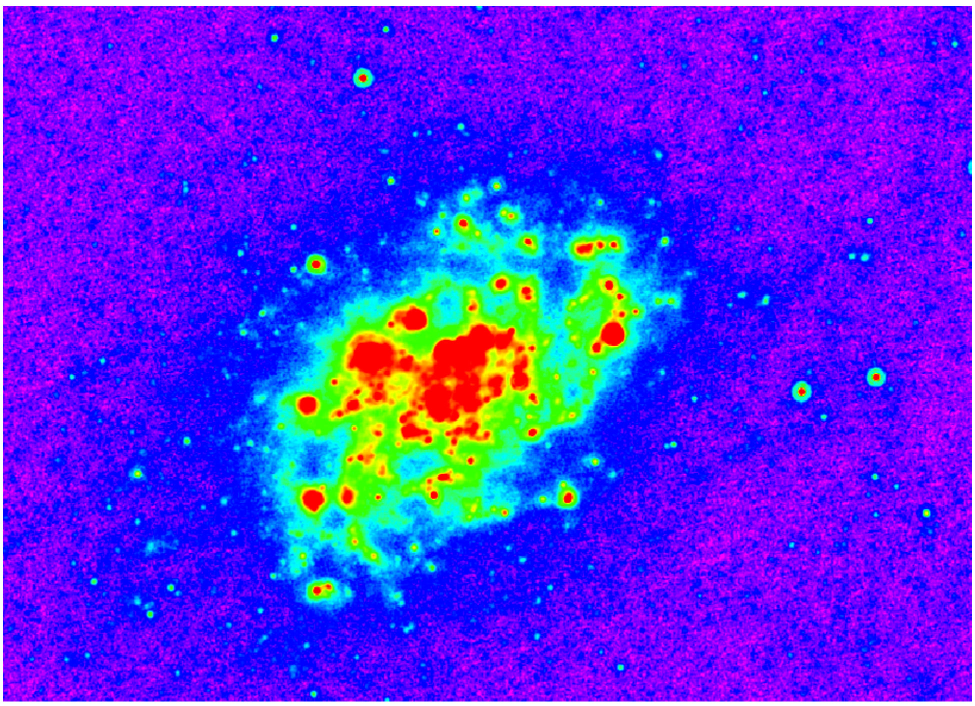

Figure 2.13: 24 μm data for NGC 2403.

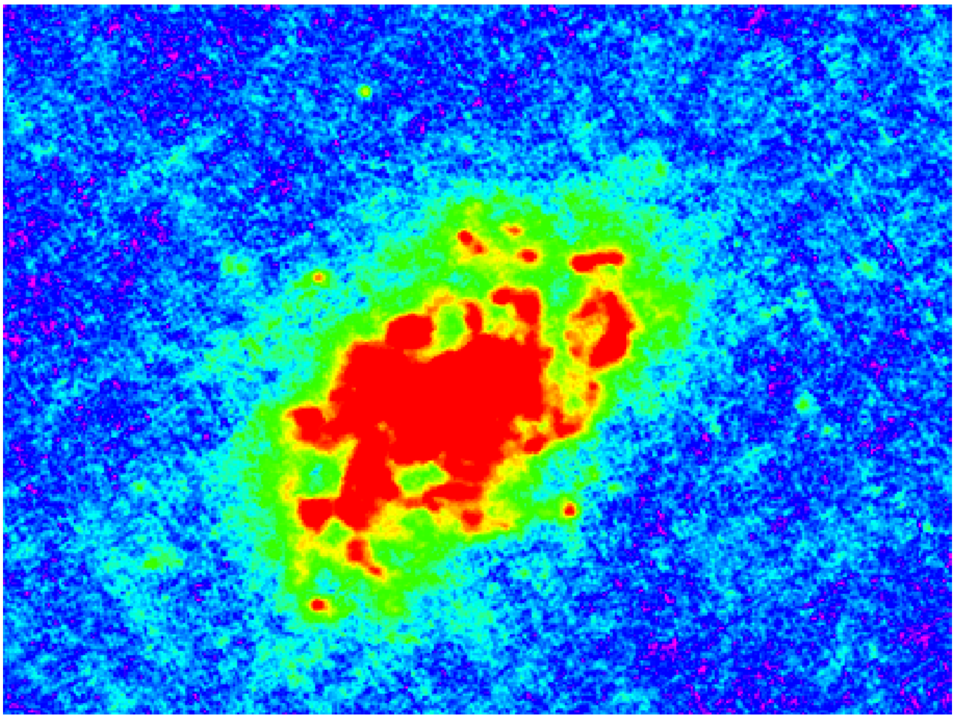

Figure 2.14: 160 μm data for NGC 2403.

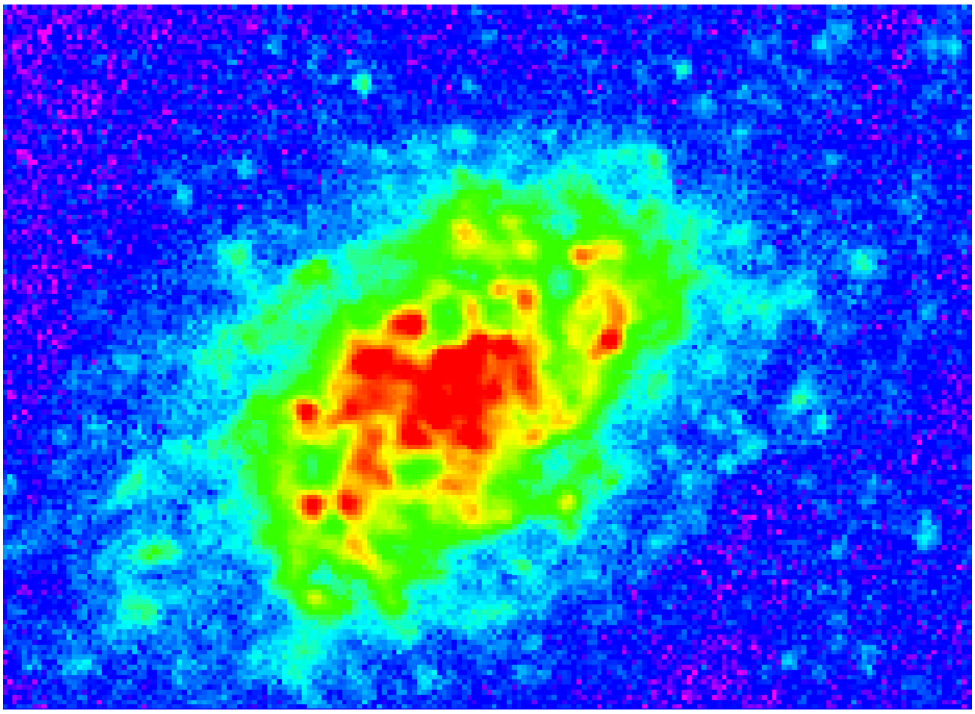

Figure 2.15: 250 μm data for NGC 2403.

Chapter 3

Observations

3.1 Observations

Once the target galaxies had been selected, the wavelengths at which they were observed were decided upon. Each wavelength filter will target a different physical property of the galaxy. The dust within the galaxies is assumed to emit as a modified black body emission function. The estimations for the wavelengths can be calculated from the temperatures of the dust, by using Wein's Law where dust at temperatures of 20K, gives a wavelength of around 250 μm.

The observations were carried out using various wavelengths to trace these properties of the spectral energy distribution emitted; 3.6 μm to represent the stellar continuum. PAH emission is observed at 8 μm (corresponding to the 7.7 μm feature). The 24 μm emission traces the hot dust, 160 and 250 μm to trace the cold dust.

The data are summarised in Table 3.1, this provides a reference for the origin of the data and the processing steps used before analysis.

3.1.1 3.6 IRAC Data

The 3.6 μm data are used to trace out the stellar continuum [Mentuch et al., 2009, Smith and Hancock, 2009, Mentuch et al., 2010], are observed using the IRAC instrument on the *Spitzer* Space Telescope. It observes simultaneously at 3.6, 4.5,

Table 3.1: Table summarising the sources of the data

Wavelength	Instrument	FWHM (arcseconds)	Flux calibration Uncertainty	Reference for Data
3.6 μm	Spitzer IRAC	1.44	3%	Dale et al. [2009]
8 μm	Spitzer IRAC	1.71	3%	Dale et al. [2009]
24 μm	Spitzer MIPS	6	4%	Bendo et al. [2012b]
160 μm	Herschel PACS	11.31 $\times$ 13.32	5%	Roussel [2012]
250 μm	Herschel SPIRE	18.3	5%	Bendo et al. [2012a]

5.7, and 8.0 μm. It has a 5'.2 $\times$ 5'.2 field of view. Each detector is 256 $\times$ 256 pixels across. This gives a pixel size of approximately 1.2"^{2}. The key properties of IRAC for both the 3.6 and 8 μm channels are listed in table 3.1.

The data are taken as part of the *Spitzer* Local Volume Legacy (LVL) Survey, [Dale et al., 2009] as well as SINGS Kennicutt et al. [2003], using the IRAC instrument in imaging mode. The processing steps are the same for the 3.6 and 8 μm data. The data used for post pipeline processing are from versions S18.0 and S18.5 of the IRAC pipeline. After this is done, using MOPEX mosaicking software, the multiple frames of data are combined into one single image for each band. Distortion correction, rotation of the individual frames, drift and structure bias corrections, detector artefact subtraction and a constant background subtraction are applied to the individual frames during the mosaicking step. The images are resampled into 0.75" pixels which slightly improves the PSF, when the final image is produced.

In the case of bright sources (an example of this is the nucleus of NGC 5195 in the 8 μm band) the source saturates the detector. new 1.2 second observations of the galaxies in high dynamic range are taken. The pixels affected by saturation are flagged during the processing steps. To correct for saturation, a mosaic of the 1.2 second exposures is interpolated onto the the same pixel grid as the original mosaic. A difference image is created using the two mosaics, with residual and systematic sky backgrounds removed, pixels in the difference image with values at 1 MJy sr^{-1} are flagged and these pixels in the longer exposures are replaced with the pixels in the shorter exposures.

3.1.2 8 μm IRAC Data

The 8 μm wavelength range contains little emission from hot dust and some stellar continuum. It is primarily dominated by the PAH emission feature at 7.7 μm [Lu et al., 2003, Smith and Kennicutt, 2006]. For these reasons it is an ideal choice to trace PAH emission as it has little contaminants. Data are taken using the IRAC camera on *Spitzer*.

The data were taken using the same *Spitzer* IRAC instrument as the 3.6 μm data. The data used here are part of the *Spitzer* LVL Survey Dale et al. [2009]. The processing steps are outlined briefly in section 3.1.1.

3.1.3 24 μm MIPS Data

The 24 μm emission traces out the component of dust emission primarily from hot dust [Li and Draine, 2001, Dale et al., 2005, Draine et al., 2007] and there is little contamination from other sources such as starlight. As outlined by Li and Draine [2001], Draine et al. [2007], the emission stems from several sources; the heating of very small grains stochastically up to $\sim$100 K which then cool rapidly; large grains in intense radiation fields; and steady state heating of dust at 100 K. The 24 μm dust emission is well correlated with star forming regions on a local scale as well as the global star formation of the galaxy as a whole [Calzetti et al., 2007, Zhu et al., 2008, Rieke et al., 2009, Kennicutt et al., 2009].

The *Spitzer* data from the SINGS survey [Kennicutt et al., 2003] as well as the LVL surveys [Dale et al., 2009] are produced, as a compliment to the Herschel Local Galaxies Guaranteed Time Programs by the *Spitzer Space Telescope* MIPS instrument. This is a multiband imaging photometer for *Spitzer*. It is capable of imaging as well as photometry in broad bands centred at 24, 70 and 160 μm. The focus for this project is on the 24 μm band, which has a 5.4 $\times$ 5.4' field of view. The FWHM of the 24 μm is given as 6 arcsec and a flux calibration uncertainty of 4% [Engelbracht et al., 2007].

The data were processed by Bendo et al. [2012b], created from raw archival data, from the Spitzer archive. The data are reprocessed using the MIPS Data Analysis Tools laid out in [Gordon et al., 2005], along with some additional custom steps. The steps carried out are as follows. First a "droop correction", electric non-linearity correction and dark current correction are applied. Then a flat field correction along with a correction for the readout differences between columns in each data frame are applied. Pixels with signal above 2500 MIPS units were masked out to remove latent images from bright sources. Frames hit by cosmic rays or containing other artefacts were masked out manually. A flat field to correct for response variations in the array that are specific to each observation was created and is applied to the data. The background signal gradients were removed. The final step was to produce an asteroid removal across the frames where necessary.

3.1.4 160 μm PACS Data

Emission at 160 μm is thought to originate from diffuse dust heated by light escaping from star formation regions [Bendo et al., 2010]. This is not emission from the coldest dust so does not trace the majority of the dust mass within the galaxies. It is useful to compare the 8 μm emission to this 160 μm emission to see if light escaping from the star formation regions can excite the PAHs seen at 8 μm.

Data were taken by the PACS instrument aboard Herschel as part of the VNGS (P.I: C.D. Wilson). The instrument is a bolometer with two modes spectroscopy and photometry. The data here are observed in photometry mode, which has a field of view of 1.75 $\times$ 3.5 arcmin, The FWHM of the PSF is 11.31 $\times$ 13.32 arcsec. The flux calibration uncertainty is 5%, [Poglitsch et al., 2010].

The data are level-1 data, meaning it is flux calibrated and had the associated pointing information. These are processed using the Scanamorphos software, following steps outlined in Roussel [2012]. This software processes the observations from the Herschel photometers. The steps include subtracting the low frequency noise, thermal and non thermal, masking off the artefacts such as cosmic rays, as well as projecting the data onto a map. To make the level one data, the steps outlined are as follows. Bad channels are masked, ADUs are converted to voltages with timing attached to each bolometer. The pointing of each bolometer is calculated and the data are converted to useful units, here in terms of Jy per pixel. Corrections are made for electrical interference, including cross talk between the optics and electrics.

3.1.5 250 μm SPIRE Data

The 250 μm data were chosen to trace diffuse dust in the ISM. As has been shown by Bendo et al. [2010, 2012a] and Smith et al. [2012] the 250 μm emission originates from the coldest dust within the galaxies, this is useful when tracing the dust mass as a whole.

The 250 data are taken by *Hersche*l SPIRE telescope and instrument. The SPIRE instrument is as bolometer operating in three waveband filters, 250, 350 and 500 μm. It operates by scanning across the target to produce the data. The PSF has a FWHM of 18.3 arcsec. The field of view is 4 $\times$ 8 arcmin and a flux calibration at the time of writing has a flux density uncertainty of 5%, Griffin et al. [2010]. This figure has since been updated to 4% by Bendo et al. [2013]. For this project though the data are analysed using the old calibration. The difference is only small, of the order of a few percentage points, so should not account for any major anomalies.

The data were taken as a pair of orthorgonal scans using the 30 arcsec s^{-1} scan rate. The area scanned is selected to be at least 1.5 times the major diameter of the optical disk. The observations were produced using a custom version of the official pipeline script, [Griffin et al., 2009, Dowell et al., 2010], from Bendo et al. [2012a].

The first steps were to apply a concurrent glitch removal. This removes cosmic rays that affect all the detectors in the individual array. Then a wavelet glitch removal was done to remove cosmic rays from individual detectors. A flux calibration and an electrical low pass filter correction were performed. Then another wavelet deglitch and a time response correction were done.

A custom method to remove the temperature drift and bring all the bolometers to the same level were done. To create the final maps, the naive mapper in HIPE was used. The median background in areas 4 to 6 arcseonds wide outside the optical disks were then subtracted. A correction to adjust the monochromatic source flux to monochromatic extended source values was applied. This multiples the data by 0.9828. This colour correction assumes the spectral energy distribution of the dust behaves as a modified blackbody, consistent with Li and Draine [2001].

Chapter 4

Data Preparation

4.1 Data Preparation

The three galaxies were observed at a range of wavelengths from 3.6 μm to 250 μm. With the exception of the 3.6 and 8 μm data, each image was observed using a different instrument. Hence, they all have different coordinate systems, resolutions and pixel sizes, and the pixel values in the data we begin with are given in different units.

The purpose of data preparation is to match each image to a standard resolution, coordinate system, pixel size, and (when possible) units. To do this, several steps need to be carried out on each image. This chapter describes the process of preparing the data for analysis. To illustrate the individual data preparation steps, we show the preparation steps applied to the IRAC 8 μm images for M83 as an example. Some images have specific individual issues, and the steps used to deal with these issues are discussed at the end of the chapter.

The software used to prepare the data is IDL version 8.2 running on a scientific linux version 6.xx machine. The procedure is broadly similar to ones outlined by Bendo et al. [2008, 2012a].

4.2 Unit Conversion

Each image has different units depending on the instrument used. The first step is to match the units of the pixel values. The units chosen for this are Jy arcsec^{-2}. For this step a conversion factor was calculated for each image and the pixels were multiplied by this conversion factor.

Table 4.1: Table summarising the units of each wavelength to be converted into Jy arcs^{-2}

Wavelength	Original Units	Conversion Factor
3.6 μm	mJy sr^{-1}	2.350443$\times$ 10^{-5}
8 μm	mJy sr^{-1}	2.350443$\times$ 10^{-5}
24 μm	mJy sr^{-1}	2.350443$\times$ 10^{-5}
160 μm	Jy pixel^{-1}	0.1231
250 μm	Beam sr^{-1}	439.161

4.3 Removal of Foreground Stars and Other Artefacts

The vast majority of foreground artefacts are stars. It is important to subtract these as they are not part of the galaxy to be analysed and will effect the photometry of the galaxy. These stars are present in the 3.6 and 8 μm data, and may be present in the 24 μm data as well.

To identify the stars, the 3.6, 8 and 24 μm are placed side by side and compared using the DS9 image viewer software. The images are matched to one world coordinate system and a crosshair across the images. This allows the same pixels to be inspected in all three images at the same time. The stars will become fainter in the 8 and 24 μm wavelengths as their spectral energy distribution peaks towards the 3.6 μm. The objects which become fainter and drop out of the 24 μm and 8 μm images are therefore possible foreground stars. Regions are drawn around the possible stars using the region drawing tool in DS9. Care was taken to ensure the regions were suitable sizes, these were modified to include spikes in the PSF and any other extended artefacts. This was done for each star and the complete set of region files

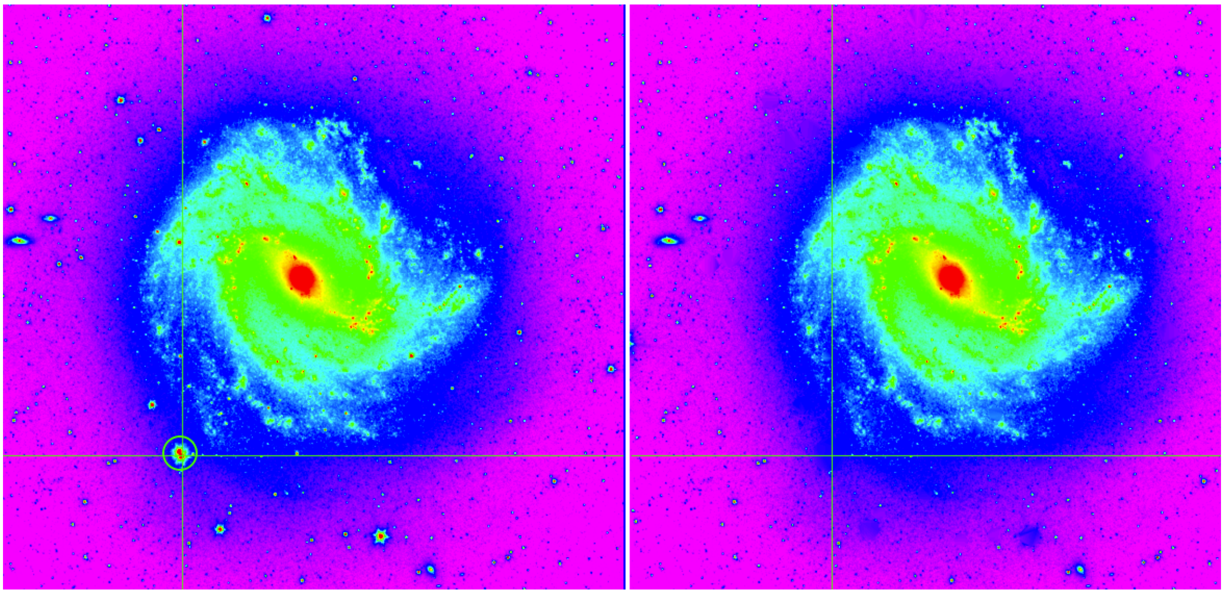

Figure 4.1: 3 μm data for M83 showing before and after star removal. The left hand panel shows the data before the star removal with the crosshair centred on a foreground object and a region drawn around the star. The right hand panel shows the data after star removal is complete. The bright objects to the east of the galaxy are background galaxies.

is saved to disc.

After this an IDL program is used to read in the region files and interpolate over the data, using a linear quintic polynomial interpolation for non-spherical data. The interpolation uses the surrounding data as a guide to fill in the regions marked as stars with new data. Figure 4.1 shows the before and after star removal for the 8 μm data for M83.

4.4 Convolution

Convolution is a mathematical operator which in this case acts on two arrays of different sizes to produce a third array, preserving the dimensionality of the original arrays. The third array is typically a modified version of one of the original arrays. In this case, the arrays we want to modify are the images once the stars are removed. Therefore the third array is a convolved images which preserves the characteristic SED of each pixel of the data for useful analysis.

We use convolution kernels to match the PSF of the data to the PSF of the images with the lowest resolution, the 250 μm data, this low resolution is a combination of both the wavelength at which the data are taken and the size of the telescope used.

4.4.1 Generating The Convolution Kernels

We use convolution kernels generated using the methods outlined in Aniano et al. [2011]. The convolution kernels will transform the images with different PSFs into a common PSF where the kernel K $\{A \Rightarrow B\}$from instruments A to B satisfies the following conditions,

$$I_B(x,y) = \int\int I_A(x',y'K\{A \Rightarrow B\}(x-x',y-y')dx'dy' \equiv (I_A \star K\{A \Rightarrow B\})(x,y)) \quad (4.1)$$

where I_A and I_B are the observed images from instruments A and B respectively. and x and y are the coordinates of the arrays. The PSFs are assumed to be approximately similar to rotationally symmetric functions. Whilst in practice this might not be the case, this would require extra kernels for each orientation of the telescope instruments.

The kernels are all of different sizes for each wavelength. In some cases when using the full sized kernel, the convolution process would have been too time consuming so we cropped the kernel to take a smaller portion of it. The cropping was done to ensure the central pixel of the kernel remained at the centre of the box. For the 3 and 8 μm data, we used kernels 200 $\times$ 200 pixels. For the 24 μm data, the kernel was 513 $\times$ 513 pixels. To convolve the 160μm data, the size of the kernel was 150 $\times$ 150 pixels.

4.4.2 Convolving the Data

The data collected are all of different wavelengths and as a consequence have varying point spread functions (PSFs). The process of convolution allows matching of these PSFs with no loss of colour from the sources. This is done so we can analyse the variations in the intensity of the emission of the different wavelengths.

In this case the data are convolved with kernels that match the PSF of the data to the largest PSF in the analysis, the 250 μm Hereschel SPIRE images. These

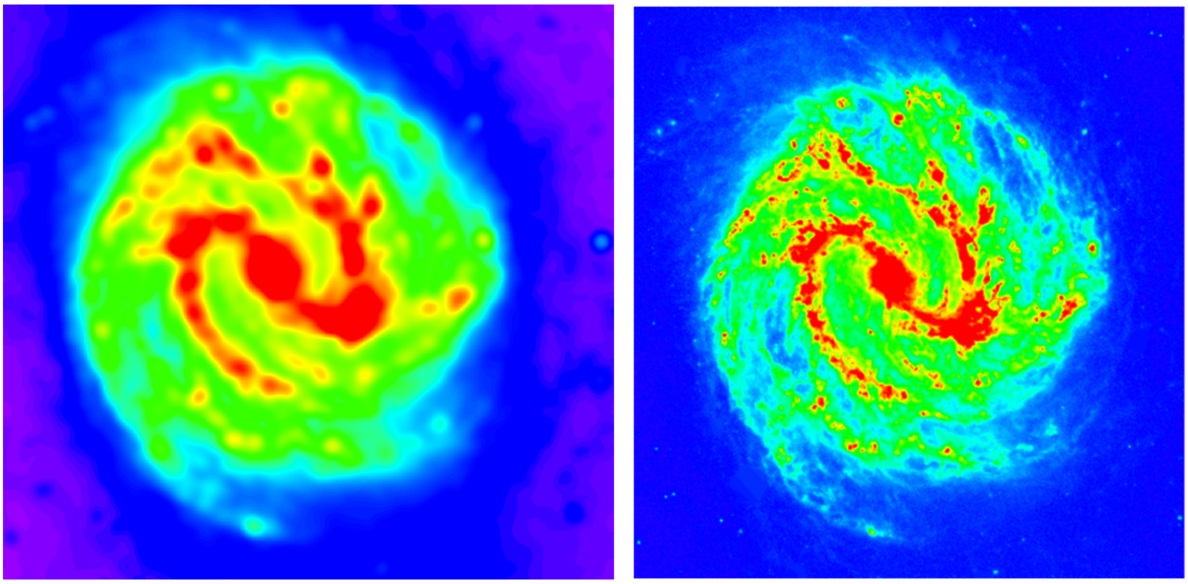

Figure 4.2: 8 μm data for M83 showing the data image on the right, and the convolved image on the left. Notice how the data have been smoothed out.

have the largest PSF, the FWHM being 18 arcseonds. These kernels allow the preservation of each pixel spectral energy distribution Aniano et al. [2011].

Convolution can be carried out using the IDL command "CONVOL". There are various keyword commands when using this step to alter how the procedure deals with the edge of the image. The keywords EDGEZERO and NAN are used to refine the procedure in this case. EDGEZERO will compute the convolution as though the edge of the image are set to zero. The NAN keyword ensures pixels with values of NaN or infinity are set as missing data and are consequently ignored for the convolution.

These two commands tidy up the edges of the convolved data. Here the IDL command sees the data past the edges of the images as being zeros. The convolution is carried out on all the images apart from the 250 μ data. Figure 4.2 shows the 8 μm IRAC image before and after convolution. The convolution step has matched the PSF of the 8 μm data to the PSF of the 250 μ data. This also makes the image look smoothed.

4.5 Match Coordinates

To perform analysis, the images must all be in one coordinate system. This is to keep the astrometry for each image the same, and avoids any potential offset issues when analysing the data at later stages.

To be consistent with the convolution to the 250 μm data, this was taken as the reference for coordinate matching. The 3.6, 8, 24 and 160 μm were matched to this reference using the coordinate transformation procedure "HASTROM", which rotates and shifts the alignment so the pixel coordinates are all the same. This command also preserves the flux in each pixel, as well as the pixel sizes for each image.

4.6 Background Removal

After the image alignment steps, the background needs to be subtracted. Some of the images are not background subtracted and contain infrared emission from dust within the MW known as cirrus, as well as cosmic infrared background from high redshift galaxies. There are also sources of zodiacal dust and infrared bands from stars within the MW. These additional sources of emission need to be subtracted out before proceeding with the analysis.

First the optical disc of each galaxy data were taken from de Vaucouleurs et al. [1991]. This is defined as the isophotal diameter measured at a surface brightness of μ_B=25 B arcmin^2. This was superimposed over the image in a DS9 region file shown in Figure 4.3. Emission from outside this region is assumed to originate primarily from the background. This was selected by drawing regions using DS9 suitably placed around the outside of the optical disc and saving them all to one region file. Care was taken to ensure no bright foreground/background sources not associated with the galaxy are included within the regions selected as background.

The next step is to read in the region files into IDL identifying the pixels in the background regions. This sets a mask array over the image where the indices of data within these region files are set equal to one. A parameter is set which will only

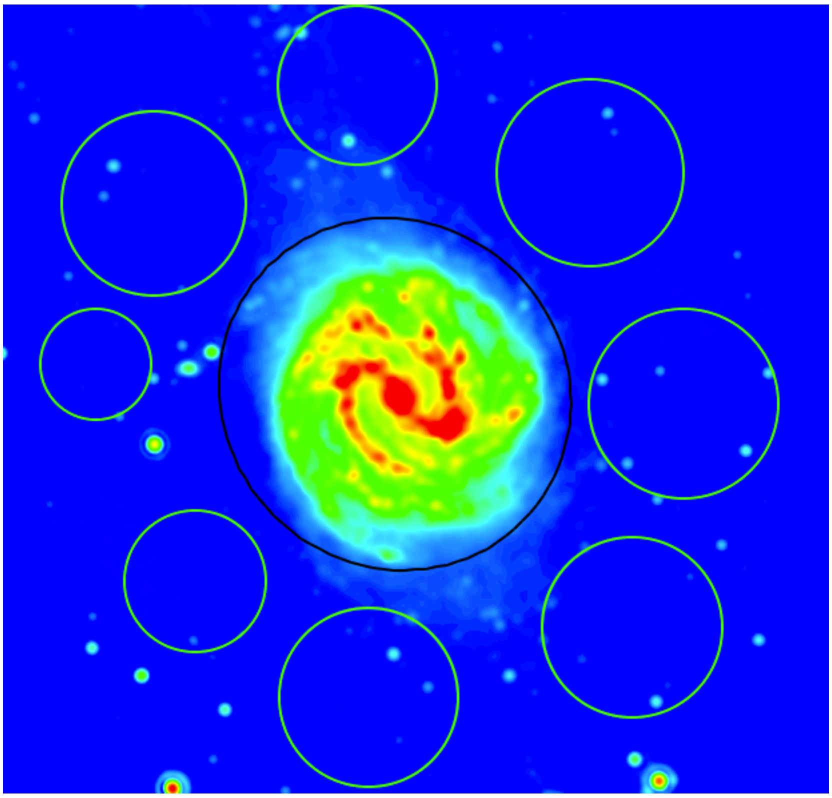

Figure 4.3: 8 μm data for M83 showing the optical disc and the regions selected for the background subtraction.

read the data with indices equal to one. The data outside the regions have indices equal to zero so are effectively ignored by this parameter. The median pixel values in these regions was subtracted from the image.

Two of the 8 μm images needed separate treatment, NGC2403 and M51 had surface gradients across the background. These had a separate treatment as the median of the background in the regions is not uniform.

For NGC 2403 the background was selected using DS9 by masking out the optical disc of the galaxy. To remove the background, a function needs to be assigned to the background surface and subtracted from the data. This was done by making a 3 dimensional array where the z axis values are the pixel values of the background. The procedure "SFIT" was used to fit a surface polynomial of order 1 to the surface gradient. This produces an equation for the surface using parameters chosen by SFIT. Figure 4.4 shows the surface fitted to the 8 μm data as well as the before and after data for a comparison. This surface represents the background, and was then subtracted from the convolved image.

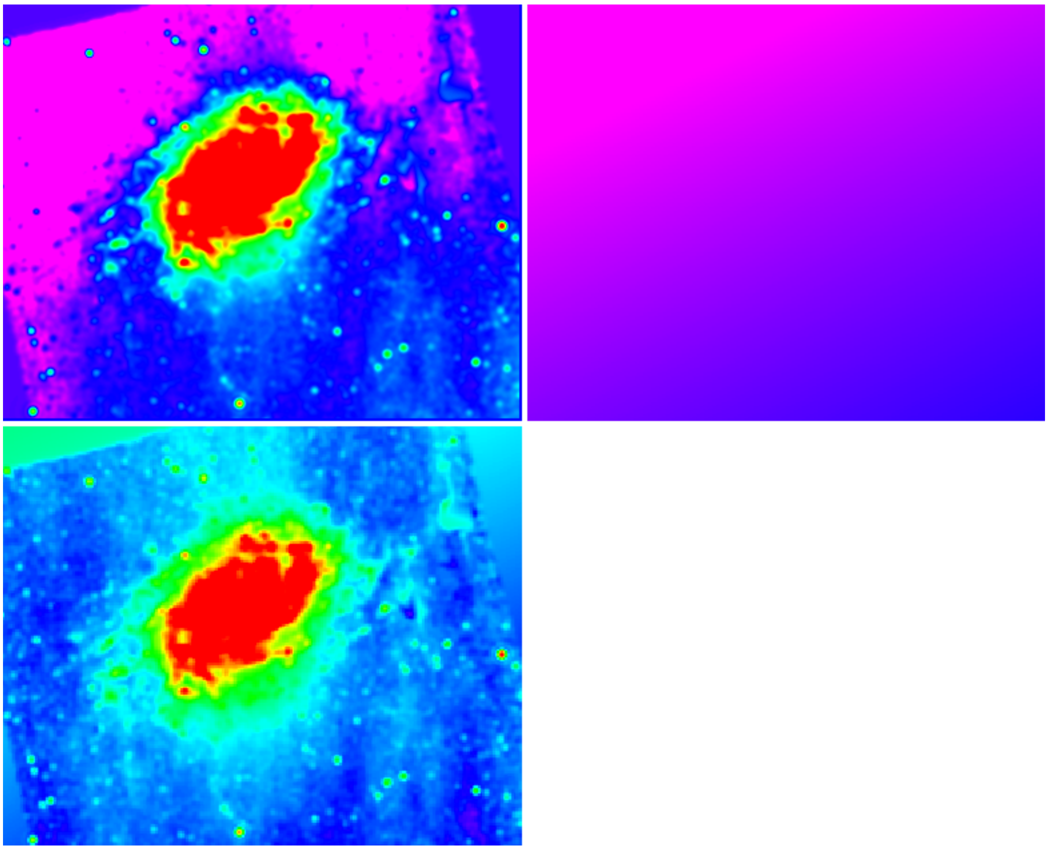

Figure 4.4: 8 μm data for NGC 2403. From top left clockwise: The coordinate matched image; surface assumed to be the background; background subtracted image.

For M51, the data are as a mosaic of different images as per how the IRAC instrument performs the observations at different positions across the galaxy. Therefore, it was decided to split this up into columns and subtract the background one column at a time. A procedure was written to divide the image into columns of one pixel width. The median of each column was subtracted from that column. Masked regions containing bright background sources, as well as the optical disc of the galaxy, were set so the pixel values with these regions were equal to zero for the background subtraction.

4.7 Cropping And Rebinning The Data

4.7.1 Cropping the Data

The coordinate matching of the images sets them all to the same size. We crop the data down to extract the useful data from the images, as the extra background is not needed for the analysis. The useful data are extracted using a box of predetermined sizes. The size of this extraction box is calculated by drawing a region 1.5 $\times$ the size of the major axis diameter of the optical disc (given in arcminutes). This gives an extraction box size in terms of pixels. The pixel scale is such that there are 6 arcseconds to a pixel. Hence when converting from arcminutes to pixels, multiplying by 10 gives the size of the box in pixels.

The box size was then adjusted to be an integer multiple of three. This is so when we rebin the data, the central pixel remains in the centre of the galaxy. This avoids astrometry issues with the analysis.

The cropbox is shown in figure 4.5. This is centred over the centre of the image using the centre reference pixel as a guide. The information for this was read off the header of the image using DS9 to access it. The coordinates of the box in terms of pixels were noted down for each galaxy. The bottom left and top right pixel central values on DS9 were recorded as $x_0, x_1 : y_0, y_1$. The box was saved as a region file for further use.

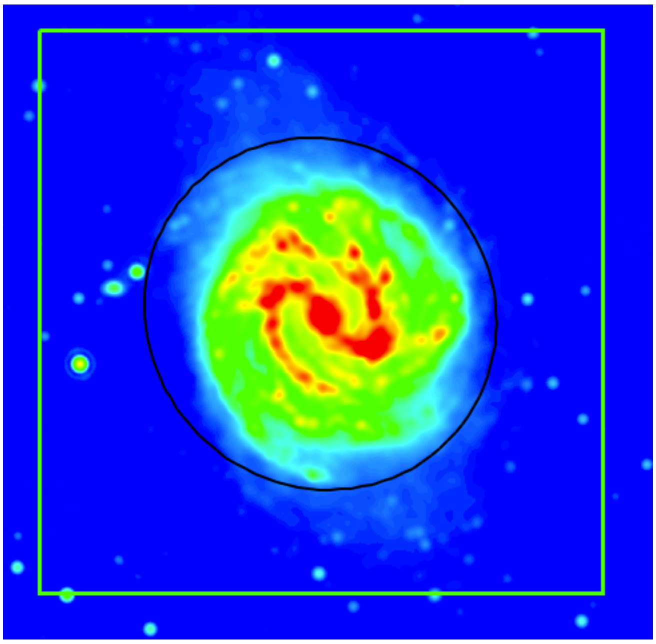

Figure 4.5: M83 8 μm data with the optical disc and box used to crop the data.

The procedure "HEXTRACT" in IDL was used to extract this box using the values of the reference pixels in each corner of the box minus one. This is because IDL reads in arrays where the first indices are zero not one as in DS9. This new image was saved to disc ready for the next step.

4.7.2 Rebinning

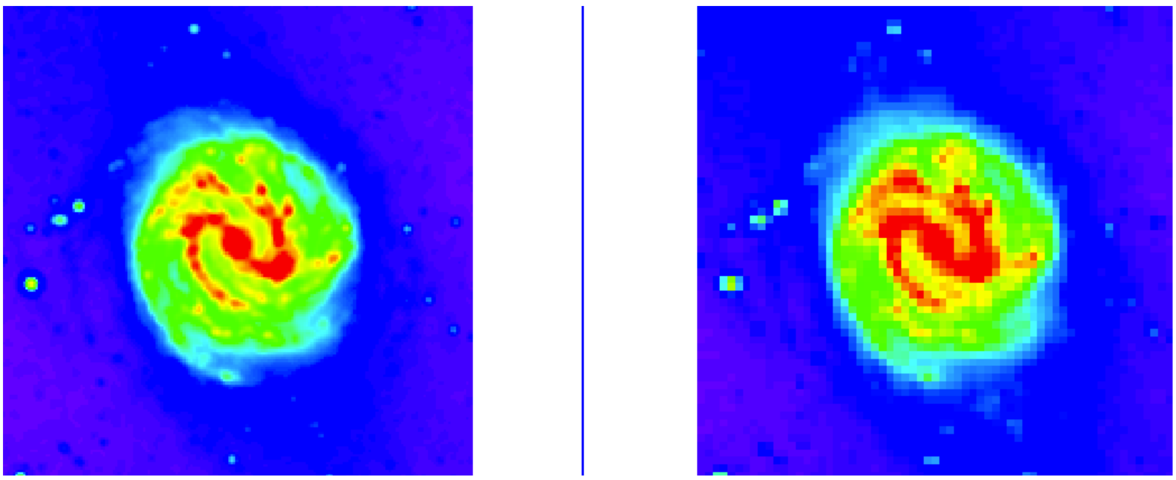

Figure 4.6: M83 8 μm data on the right with the optical disc and box used to crop the data for reference. The rebinned data is shown on the left. The colour bar and image scale are identical for both images. The pixels in the rebinned data are much larger in size.

The next step is to match the pixel sizes, so they correspond to the size of the largest PSF. This will ensure the PSF is not separated into several components and loss of colour variation might occur. Therefore to rebin the data, pixels which are no smaller than the largest PSF are used. The rebinned data require a pixel size of 18” across to match the PSF of the 250 μm images. We will lose some image quality at the smaller wavelengths, but this ensures the PSFs of the data are matched evenly across all wavelengths for analysis.

To calculate the size of the rebinned box in terms of number of pixels, the box used for the cropping step was loaded into the galaxy. This was modified so the lengths of the sides were an odd integer multiple of 3. This is because the 6 arcsecond pixels now need to be rebinned into 18 arcsecond pixels. The odd number ensures the central pixel remains on the centre of the galaxy. The size of the rebinned box for each galaxy were given as:

- NGC 2403: 109 $\times$ 109 pixels
- M83: 63 $\times$ 63 pixels
- M51:59 $\times$ 59 pixels

The “HREBIN” command was used to rebin the data. This increases the size of the pixels. The size of the array is reduced, so the procedure takes the average of the box of 9 pixels to be rebinned into one pixel. Figure 4.6 shows the same sized box with the data before and after the rebinning steps.

4.8 Stellar Continuum Subtraction

The star subtraction step will remove foreground objects, these are present in the 8 and 24 μm data. The data at these wavelengths also contain emission from stellar sources within the target galaxies, as well as emission from stellar objects within the MW. For this analysis these components need to be subtracted out to use these data as tracers of interstellar sources.

The stellar continuum for these galaxies is a function of the 3.6 μm emission, Helou et al. [2004]. This is subtracted from the 8 and 24 μm data to leave continuum subtracted interstellar emission in the target galaxies. This numbers are given as a fraction of the IRAC 3.6 μm data:

- IRAC 8.0 / IRAC 3.6 : 0.265 +/- 0.007
- MIPS 24 / IRAC 3.6 : 0.0368 +/- 0.0014

We then use these numbers to apply a correction factor as shown:

$$I_\nu(8\ \mu m \text{ continuum subtracted}) = I_\nu(8\ \mu m) - (0.265 I_\nu(3.6\ \mu m) \tag{4.2}$$

$$I_\nu(24\ \mu m \text{ continuum subtracted}) = I_\nu(24\ \mu m) - (0.368 I_\nu(3.6\ \mu m) \tag{4.3}$$

4.9 Data Selection

Once the data have been rebinnned and continuum subtracted, the final step is to select the good data for analysis. Only the data above a 5σ signal to noise ratio are used. To measure the noise in the data, the standard deviation of the background outside the optical disc was measured. Pixels with values 5 $\times$ greater than this are selected using a where command.

For the analysis of M51, the companion NGC 5194 needs to be masked out as this is not part of NGC 5195. When we plot the contour maps in section 5 NGC 5194 is left in to show the complete picture of the galaxy, but for the plots and other analysis it is ignored. To do this we use the 8 μm data as a template for all wavelengths. A region was drawn to approximate the companion galaxy in the 8 μm data. The pixel values within the region are set to zero for all wavelengths, this is shown in Figure 4.7. Once the data have been selected for analysis the analysis can be performed.

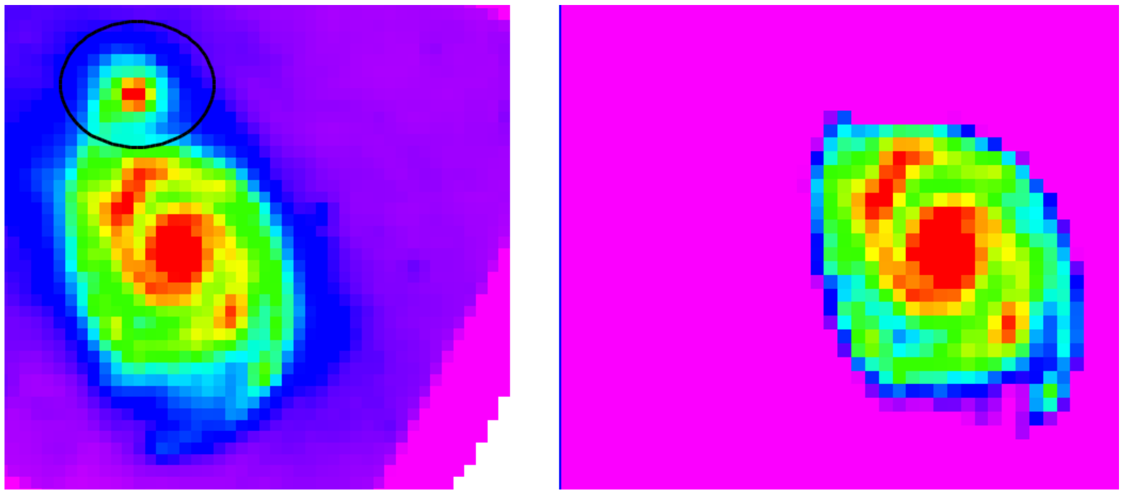

Figure 4.7: M51 8 μm rebinned data showing the masked out region for NGC 5194. The figure on the left shows the before masking and the subregion containing NGC 5194. The figure on the right shows after the data are masked.

Chapter 5

Analysis

The data are presented for analysis in the following ways. First the relations between the 8 μm emission with the 3.6, 24, 160 and 250 μm dust emission are discussed for all three galaxies. Then each galaxy is discussed in sequence as there are various analysis methods used and results taken for each galaxy. When presenting each galaxy, the sequence runs from NGC 2403, M83 to M51. This is the simplest case to the most complex case.

These contour and ratio maps are produced using the surface brightness ratios and not yet converted to colour temperature maps. The purpose of these is to describe the ratio of surface brightness structure for the different wavebands and the selected ratios. All maps are made using data convolved to a 18 arcsecond resolution. This is good enough to show the variation on a local scale, as indicated by the presence of distinguishable regions.

When analysing the data and drawing the plot for M51 it was decided to mask off NGC 5195 from the data, This was done as this is a companion galaxy and is not of interest to us for the results. The contour maps in the following sections show the companion as well as NGC 5195. The decision to include it within these maps is purely to show a complete picture of the objects as a whole. An area of 2 $\times$ 1.6 arc minute covering NGC 5195 is masked off. This is shown in Figure 4.7 in Section 4.1.

5.1 Analysis On All Three Galaxies

5.1.1 8 μm emission and 24 μm Emission

Figure 5.1 displays the contour maps of the surface brightness of the 8 and 24 μm data. Figure 5.2 shows the ratio of the 8/24 μm colour variation. For all three galaxies, the 8 and 24 μm contour maps show the 8 μm emission and 24 μm hot dust emission trace similar structure. Variations in intensity with radius in NGC 2403, and well defined spiral arms for M51 and M83 are seen in both wavebands. The strongest 8 and 24 μm sources in both M51 and M83 are within the nucleii, for NGC 2403, the brightest region in both wavebands is located to the northeast of the centre of the galaxy. All three galaxies show a drop off in intensity of 8 μm emission with increasing radius, this is especially evident, in NGC 2403 which does not share the same spiral arm structure as the other two galaxies. In NGC 2403, a flocculent rather than grand design type, several bright star forming regions within the galaxy as traced out by the 24 μm as well as some appearing enhanced in the 8 μm. The centre of the galaxy shows enhancement of 8 μm emission where star forming regions are not present. For M51 and M83 the 8 and 24 μm contours trace out the spiral arms and structures and the individual star forming regions can be picked out in the 24 μm maps for these galaxies. The 8 μm emission also following the same pattern of intense emission within the nucleus and tracing out the spiral arms, though is slightly smother and structures are not as well defined. The similarities in the contour plots are evident in the scatter plot Figure 5.3, where all three galaxies show a correlation where the 8 μm increases with 24 μm surface brightness.

For each galaxy the individual contour maps of the 8 μm and 24 μm wavebands shows the possibilities of using 8 μm emission as a tracer of star formation. In order to look more closely at the relation between the 8 and 24 μm emission, we created ratio maps. The ratio of 8/24 μm is plotted on contour maps in Figure 5.2. These show the enhancement of the 8 μm emission relative to the 24 μm emission. These plots give a clearer picture of the relative differences in the 8 and 24 μm surface

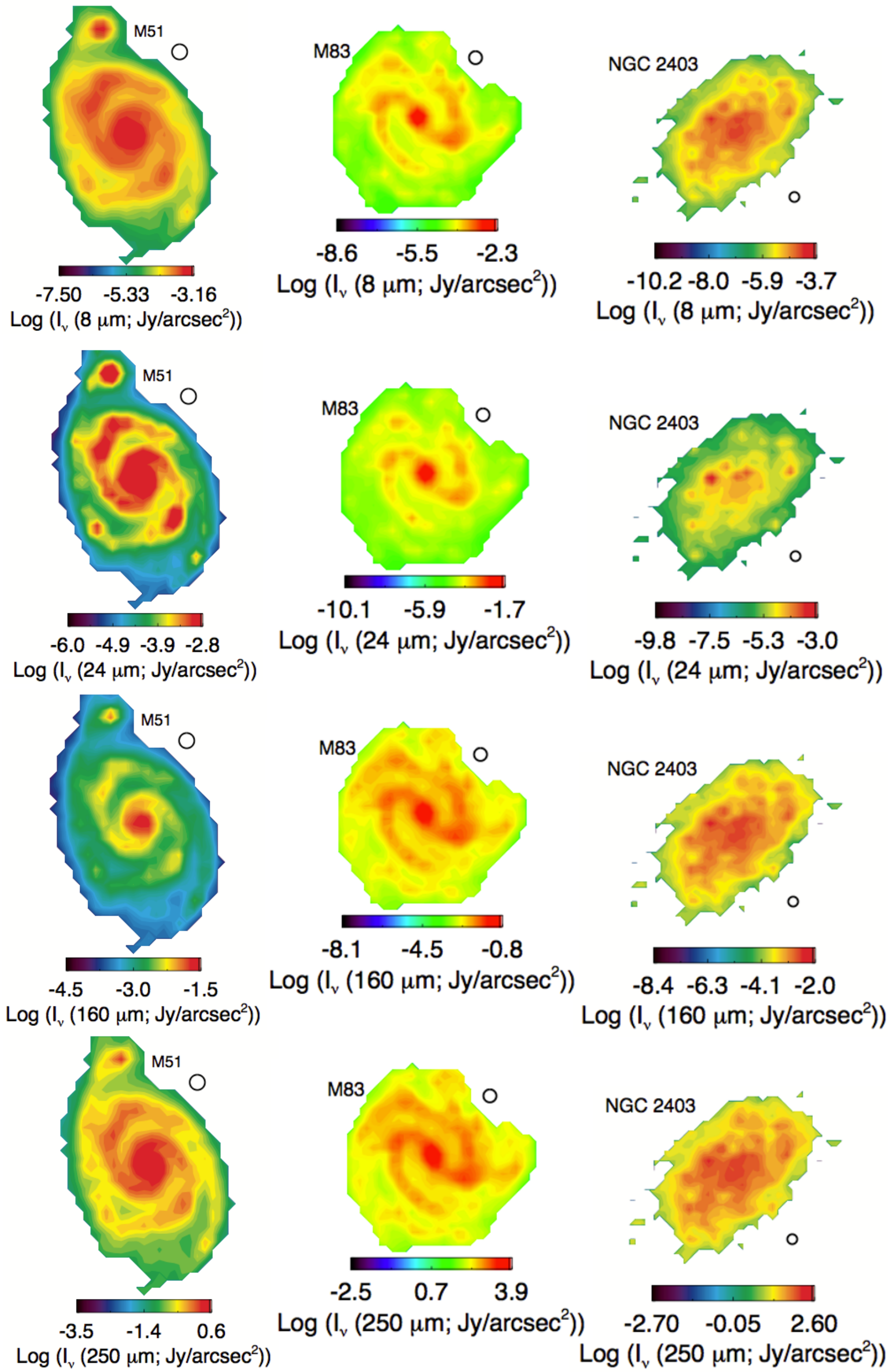

Figure 5.1: 8, 24, 160 and 250 μm emission surface brightness plots. All data plotted here and subsequent contour and ratio plots are the rebinned 18 arcsecond pixel sizes with gradients smoothed over to show the variations in intensity of emission. The circles represent the 18 arcseconds bins for each galaxy.

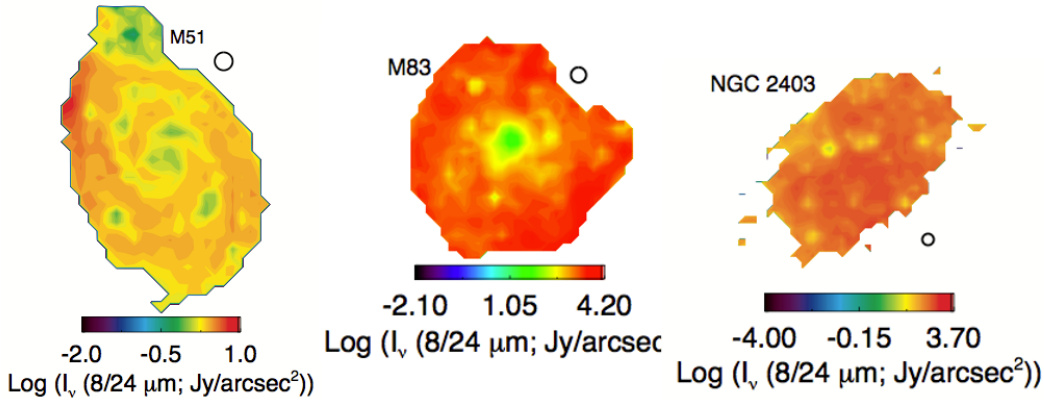

Figure 5.2: 8/24 μm ratio plot, showing the colour variations of the galaxies. The circles represent the 18 arcseconds bins for each galaxy.

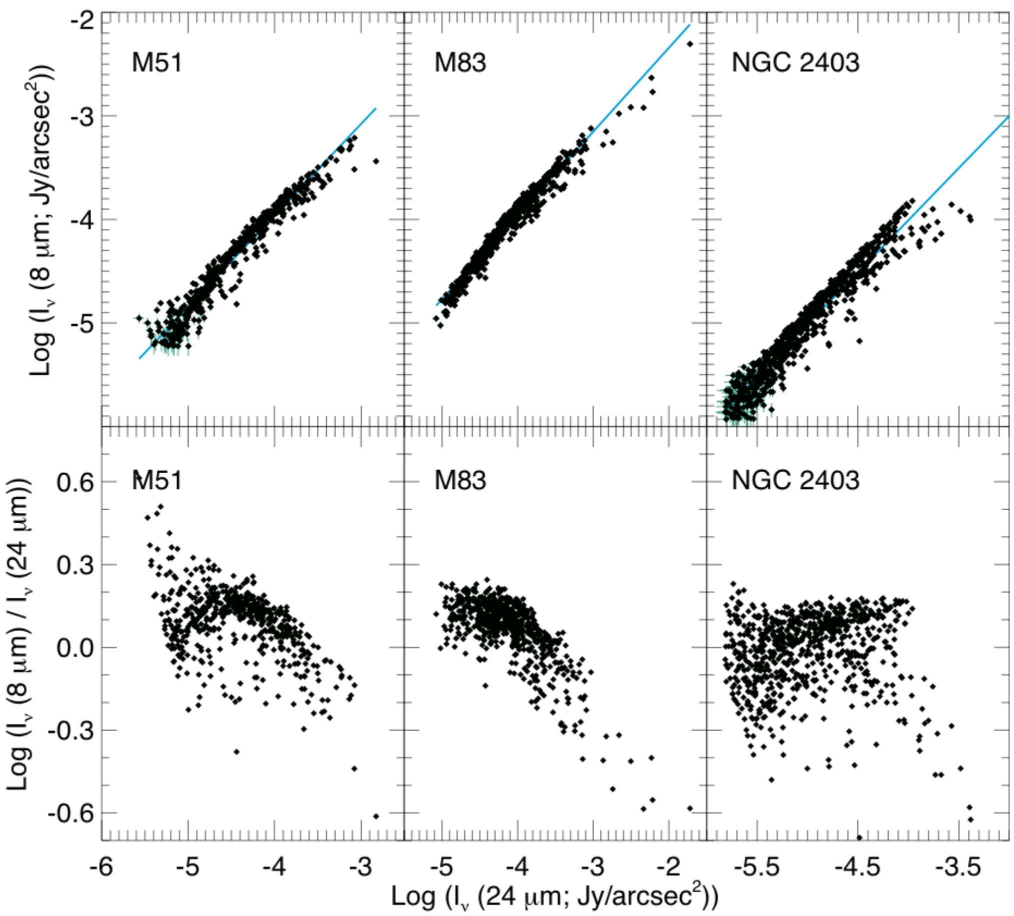

Figure 5.3: 8 μm emission as a function of 24 μm emission for all three galaxies. The lower panels show the ratio of 8/24 μm vs 24 μm surface brightness indicating the colour variation. The blue line for this and subsequent plots marks the line of best fit to data with errors in x and y coordinates. We used the "FITEXY" procedure, plotting the linear least squares approximation in one dimension.

brightnesses.

The ratio plots show a very different picture to the contour maps of the individual wavebands. For all three galaxies, the regions which are brightest in 24 μm have the weakest 8/24 μm colour ratio. The two grand design galaxies show the 8/24 μm ratio is lowest within the nucleii. As M83 has a starbust nucleus, it could be expected that the strongest 24 μm emission originates in the nucleus. This could skew the colour scale a little and make the star forming regions within the spiral arm appear redder than they are. With this scale it is still possible to determine the spiral arm structure and star formation within the arms is also visible. For M51 and NGC 2403, the star forming regions appear bluer and can be identified much more easily than M83, with the spiral arms of M51 being identifiable. For NGC 2043, the peak in the 8 μm emission in the centre of the galaxy does not appear in the 8/24 μm ratio map. This shows that the 8 μm surface brightness in the centre of the galaxy is not as sensitive to the 24 μm surface brightness, seen in Figures, 5.1 and 5.2. Since the areas of strongest 24 μm emission are know to trace star formation, we see a high rate of star formation has a weakening effect on the PAH emission.

The maps show the picture to first principles, where the locations of the star forming regions as traced out by the most intense 24 μm emission and the most intense 8 μm emission are correlated. The ratio plots show this relationship is not as well defined as shown in the contour maps in Figure 5.1. From the 8/24 μm ratio plots it is possible to infer that on local scales the 8 to 24 μm relationship breaks down and the PAHs are being inhibited in some way.

The Figure 5.3, shows a correlation for all three galaxies, as indicated by the top panels. Here it can be generally stated that the 8 μm emission correlates with the 24 μm hot dust emission quite well. Each correlation coefficient shows a strong correlation for all three galaxies, as indicated in Table 5.1, but this is not indicative of the whole picture. The plot of the 8/24 μm colour variations is useful to show the difference in the colour with respect to the 24 μm surface brightness. Here for all three galaxies the 8/24 μm ratio decreases with the 24 μm increase. This is consistent with the ratio maps where the 8/24 μm ratio decreases with the 24 μm

Table 5.1: Table showing the correlation coeffecients for the plot for the logarithm of 8 μm emission vs logarithm 24 μm emission.

Galaxy	Correlation Coeffecient
M51	0.895
M83	0.979
NGC 2403	0.969

surface brightness.

Taking the simplest case first, NGC 2403, there appears to be a strong relationship between the two wavebands. However, as can be seen by the points at the bright end of the relation dropping off below the line of best fit, there is little correlation. These points represent the strong star forming regions and show the photo disassociation of the PAHs by the strong UV photons from young stars within the star forming regions. The ratios plotted show this picture up very well, the high amount of scatter show the lack of correlation despite a 0.969 correlation coefficient. The flat ratio is probably due to the centre of the galaxy, where the 8 μm emission is strong and the 8/24 μm colour variation relatively flat. The shape of the plot indicates that where the 24 μm emission is strongest the 8/24 μm is weakest, confirms the conclusions that can be drawn from the plot of the 8 and 24 μm relationship.

The case of M83 is a little more complicated. The correlation coefficient points to a regime where the 8 μm and 24 μm emission is correlated, similar to NGC 2403. Though the correlation is the strongest out of all three, the plot of the 8/24 μm ratio plot reveals that the relationship is more complex than a simple linear relationship. The faint end exhibits a relationship where the 8 μm and 24 μm behave with a tighter relationship. There is a knee at log (I_ν(24 μm) = -4 in both the 8 to 24 μm surface brightness plot, and 8/24 μm ratio to 24 μm colour variation plot. This shows the 8 μm emission is weakened compared to the the 24 μm surface brightness. The weakest 8/24 μm ratio corresponds to the strongest 24 μm emission in the spiral arms and especially the nucleus. The ratio plot on Figure 5.2, shows this to be the case where the nucleus is much bluer than the rest of the galaxy. The downward slope of the 8/24 μm ratio plot indicates as the 24 μm increases the 8/24 μm ratio decreases, this is more evidence to a similar picture to NGC 2403 where the 8 μm emission is suppressed in star forming regions.

Figure 5.3, shows the 8 to 24 μm relationship for M51. The 8 μm emission is inhibited in regions where the 24 μm is strong. Yet, it shows a roughly linear relationship. However, this galaxy has the weakest relationship given by the correlation coefficient and a majority of the points lying below the best fit line. The relationship here is similar to M83, with much more scatter across the whole relationship. The plot of 8 to 24 μm shows a fairly good correlation with no obvious inhibitions of the 8 μm emission compared to the 24 μm surface brightness. The plot of the 8/24 vs 24 μm shows a knee can be found at log (I_ν(24 μm) = -4.8 where the 8/24 μm ratio begins to drop off compared to the 24 μm surface brightness.

Here at the bright end, the relationship clearly shows the 8 μm emission is weaker than the 24 μm emission. The plot of the 8/24 μm ratio shows the downward trend towards the more intense 24 μm emission. This is indicative of the 8 μm being suppressed in star forming regions as traced out by the strongest 24 μm emission. The trend here is similar to M83 but with much more scatter, the correlation coefficient is evidence for the relationship here being the weakest of the three galaxies.

Every galaxy here has the same behaviour, on local scales the 8/24 μm ratio is suppressed relative to the 24 μm surface brightness. The immediate implications are in the regions with the most intense star formation, i.e. brightest 24 μm emission, the PAHs are being destroyed and can found in rings just outside these regions Helou et al. [2004], Bendo et al. [2006, 2008]. However, this does not accurately explain the intensity of the PAH emission from these regions when looking at just the 8 μm PAH emission maps. It could be that we find PAHs are abundant in these areas or we are seeing enhancements off the PAH 8 μm emission due to the more intense starlight.

5.1.2 8 μm Emission and 160 μm Emission

All galaxies show the same structure for the 160 μm as 250 μm emission discussed in Section 5.1.3. The spiral arms of M51 and M83 can clearly be seen with weaker emission in the diffuse regions. The star forming regions in NGC 2403 can be picked

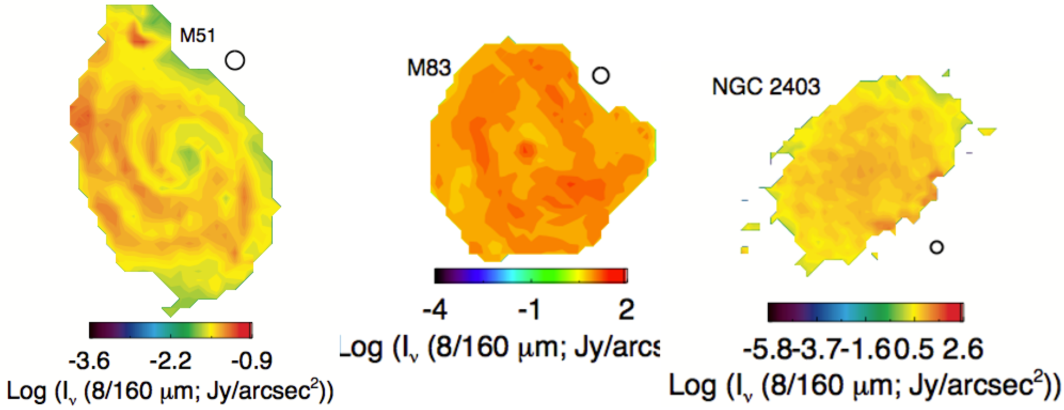

Figure 5.4: 8/160 μm ratio contour plot, showing the colour variations of the galaxies. The circles represent the 18 arcseconds bins for each galaxy.

Table 5.2: Table showing the correlation coefficients for the plot for the logarithm of 8 μm emission vs logarithm 160 μm emission

Galaxy	Correlation Coeffecient
M51	0.967
M83	0.991
NGC 2403	0.982

out and appear stronger in 160 μm, the individual structures are also easier to pick out than in the 250 μm maps. The surface brightness of all three galaxies drops off with radius as expected.

The ratio plots of the 8/160 μm emission for all three galaxies are shown in Figure 5.4. The plots here show structures more similar to the 8/250 μm ratio, shown in Section 5.1.3, than the 8/24 μm ratios. Here we see the enhancement of the 8 μm emission in the centre of each galaxy compared to the 160 μm emission. The structures of the spiral arms for M51 and M83 are seen. Compare this to the 8/250 μm ratio maps shown in Figure 5.6 as there is no offset of the 8 μm enhancement towards the outer edges in this case.

The structures in the centre of NGC 2403 are slightly more defined in the 8/160 μm map than the 8/250 μm map. This could just be a consequence of the 8 μm being brighter in these regions as a result of the stronger ISRF. In M83, we see the 8 μm emission relative to the 160 μm is weakened in regions just outside of the nucleus. The rest of the galaxy, the 8 μm are enhanced relative to the dust in the spiral arms. The intra-arm areas are relatively flat and show an almost uniform

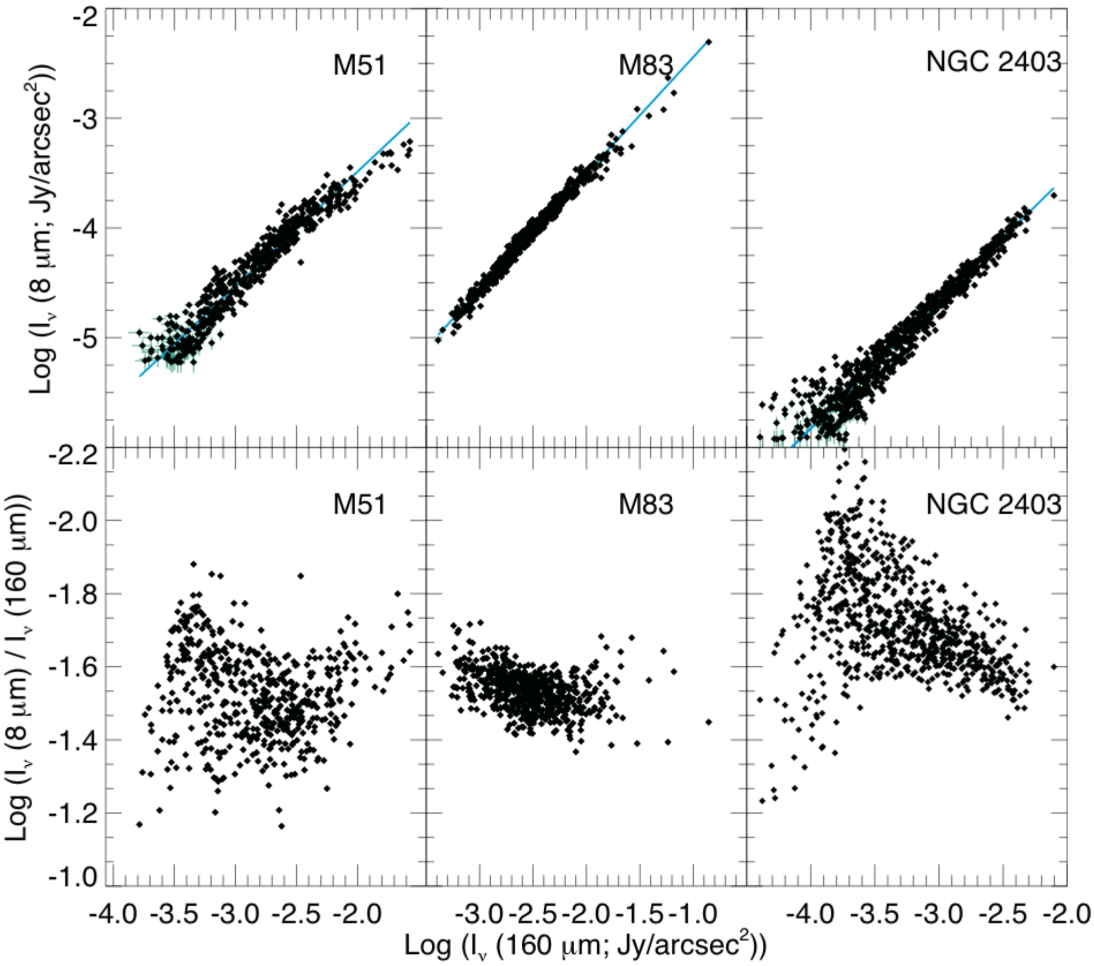

Figure 5.5: Plot of the 8 μm emission and 160 μm relationship. And the 8/160 μm colour variation vs 160 μm surface brightness emission for all three galaxies.

structure. The 8/160 vs 160 μm ratio plot of M51 shows an offset colour variation where the 8/160 μm is enhanced towards the outer edges of the spiral arms, with the intra-arm regions being much more sensitive to the 160 μm surface brightness.

Figure 5.5, shows the relationship between the 8 and 160 μm emission for all three galaxies. We plot the 8/160 vs 160 μm surface brightness to examine this relationship further. Each galaxy exhibits slightly different behaviour with the overall theme of there being a correlation between the two wavelengths. Table 5.2 displays the correlation coefficients for this relationship, and we find the best relationship in M83 with the worst relationship in M51. We can use this to compare the 8 vs 160 μm relationship to the 8 vs 250 μm relationship to constrain the sources driving the 8 μm emission in these galaxies, as we know the sources of heating of the dust at both 160 and 250 μm comparatively well. We analyse each galaxy in turn, from the least complex to most complex case, though we find the relationship for M51 and M83 to be vaguely similar.

The easiest case to understand is M83. Figure 5.5, shows a good correlation between these two data sets, and a correlation coefficient of 0.991 shown in Table 5.2. The plot of 8/160 μm vs 160 μm demonstrate this excellent relationship. The small spread indicates that the 8 μm surface brightness is dependant on the 160 μm surface brightness. Since the dust in this galaxy seen at 160 μm is heated primarily by UV photons escaping from star forming regions, Bendo et al. [2012a], the 8 μm emission is also heated by these same photons.

For NGC 2403, the relationship between the 8 and 160 μm dust shows a stronger correlation than the relationship between the 8 and 250 μm emissions, in Section 5.1.3. This would seem to imply, that the 8 μm emission is more dependant on the 250 μm surface brightness than the 160 μm surface brightness. From Figures 5.1, 5.6 and 5.9, we see the 8 μm surface brightness structures are more similar to the 250 μm emission, and the 8/250 μm emission is very similar to the 8 μm emission. We can see that the 8 to 160 μm emission may have a stronger correlation coefficient, but the plot of the 8/160 vs 160 μm relationship shows the 8/160 μm ratio decreases with the 160 μm surface brightness. However, the relationship between the 8 and 250 μm is different, see Section 5.1.3 for details. The faint end exhibits a large amount of scatter as shown by the plot of 8/160 μm vs 160 μm. From Figures 5.1 and 5.4, the ratio plot of the 8/160 μm contour map shows the structures within the centre of the galaxy are more easily identifiable in both the 8/160 and 160 μm maps than the 8 μm emission. This indicated the 160 μm emission, is in some way related to the star formation regions. However, the 8 μm emission does not show the same structure, this backs up the evidence seen in Section 5.1.1.

M51 shows a larger amount of scatter in Figure 5.5, it is evident there is little relationship between the 8 μm emission and 160 μm emission. Though there is a weak correlation between the 8 μm and 160 μm emissions, the relationship of 8/160 μm vs 160 μm shows a different picture. The large spread across the data, shows that the 8 μm to 160 μm relationship is one where the 8 μm surface brightness is not dependant on the 160 μm surface brightness. The interpretation of this is the 8 μm emission and 160 μm dust emission could have separate heating sources.

5.1.3 8 μm and 250 μm Emission

Figure 5.1 shows the contour plots for the 8 and 250 μm surface brightness. Figure 5.6 shows the 8/250 μm colour variation ratio. Both the 8 μm and 250 μm show similar structure in all three galaxies. M51 and M83 both show the spiral arm structure in the 250 μm emission. For NGC 2403, the star forming regions which are bright at 8 and 24 μm are bright in the 250 μm as well. Overall the 8 and 250 μm trace the similar structures. In the case of NGC 2403, the centre of the galaxy, has more define structures in 250 μm than in 8 μm. For M83, the spiral arms are more defined in the 8 μm than the 250 μm emission, and in M51 the reverse is true. These both peak in the 250 μm emission in the nuclei.

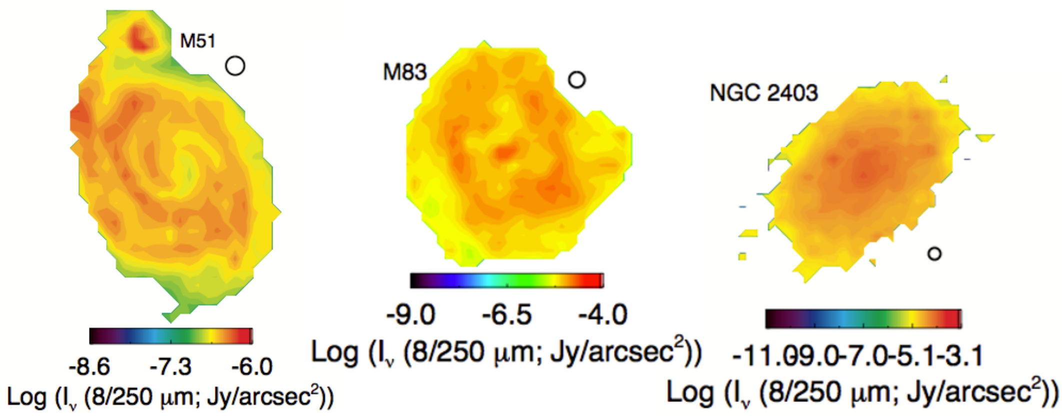

Figure 5.6: 8/250 μm ratio contour plot, showing the colour variations of the galaxies. The circles represent the 18 arcseconds bins for each galaxy.

The ratio maps in Figure 5.6 show a different picture for each galaxy. The ratio map for NGC 2403 is similar to the 250 μm contour plot. Here the structure in the centre of the galaxy is not as washed out as in the 8 μm map, but still shows the structures traced by the 250 μm emission. This shows that the 8 μm emission is closely linked to the 250 μm surface brightness. The ratio plot shows a better correlation to first order than the 8 to 160 μm relationship.

In M83, the 8/250 μm is enhanced towards the outer edges of the spiral arms, with a halo around the nucleus where the ratio drops off. This is seen in the ratio map where the regions to the north and south of the nucleus have comparatively low 8 μm to 250 μm emission. Overall the 8 μm emission is offset from the regions that are bright at 250 μm. The ratio plot does not clearly show the spiral arms.

A similar picture is the case for M51, though the bright region to the extreme left of the galaxy has artefacts due to muxbleed (image artefact caused by saturation of the detector) the instrument at 8 μm in it. This should be considered as not being a fair representation of the emission in this area. We see the 8 μm emission offset from the 250 μm emission, similar to the 8/160 μm ratio seen in Figure 5.4. The 8 μm emission is suppressed in the nucleus of the galaxy similar to M83. The fact that the 160 μm and 8 μm emissions are not correlated suggests the heating mechanisms for the PAHs are not similar to those of the hot dust and warm dust, there are probably multiple heating sources for the dust in this galaxy.

Figure 5.7 shows the relations between 8 and 250 μm emission for all the three galaxies and Table 5.3 shows the correlation coefficients. The ratio plots show there is a strong relationship between the 8/250 μm and 250 μm surface brightness for NGC 2403 and M83. However, M51 has a more complicated relationship.

The case for NGC 2403, shows there is a very strong correlation between the 8 μm and 250 μm emission sources. Both Figures 5.1 and 5.6 show the 8 μm emission increases with 250 μm surface brightness. In Figure 5.7, the 8/250 vs 250 μm shows we see the 8 μm emission increases with the 250 μm surface brightness. This is different to the relationship discussed in Section 5.1.2, despite the weaker correlation coefficient. Overall the picture shows the 8 μm emission carriers are mixed in with the 250 μm emission, and the heating mechanisms for both are the same or very similar.

M83 has an even stronger correlation between the 8 and 250 μm emissions than NGC 2403, the weak scatter in the 8/250 μm vs 250 μm ratio in Figure 5.7 shows this. The plot shows the 8 μm emission dependance on the 250 μm surface brightness is not as strong as the relationship between the 8 and 160 μm emission. A similar result is seen in Figure 5.6, the implications of this are the 8 μm emission is not

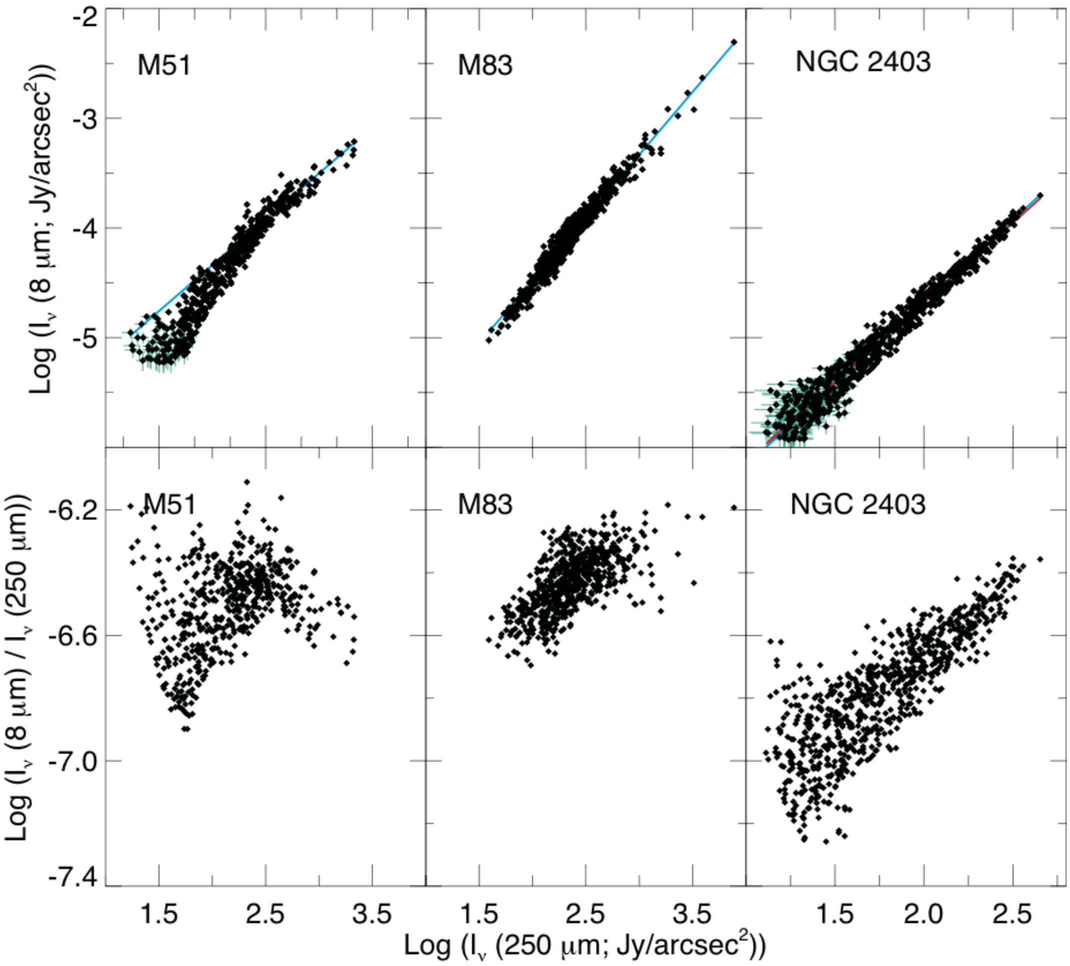

Figure 5.7: 8 μm emission as a function of 250 μm cold dust emission for all three galaxies. Lower three panels show the 8/250 μm vs 250 μm surface brightness.

as dependant on the heating sources that drive the 250 μm emission, as is the case for NGC 2403. Figure 5.7 shows at around log $I_\mu(250\ \mu m) = 2.5$ Jy arcsec^{-2}, the relationship changes. At the bright end of the relationship, the 8 μm emission is slightly suppressed relative to the 250 μm emission. At the faint end, the emission for both 8 μm and 250 μm seem to be better correlated with the 8/250 μm increasing with 250 μm surface brightness. This goes some way to explaining why the 8 to 250 μm relationship is not as strong as the 8 to 160 μm relation. Though both the 160 μm and 250 μm emissions will be correlated if plotted for this galaxy.

Here the relationship points to a picture of both the PAHs and cold dust having the same heating mechanism. There are two probable reasons for this, the PAHs and cold dust are being excited at a distance by UV photons which escape the star

Table 5.3: Table showing the correlation coefficients for the plot for the logarithm of 8 μm emission vs logarithm 250 μm emission

Galaxy	Correlation Coeffecient
M51	0.969
M83	0.982
NGC 2403	0.980

forming regions. Or the evolved stellar population is responsible for the heating of them. It is likely that a combination of these two are the case. The offset of the PAH emission to the outer edges of the spiral arms, hints at the likely case of strong dust attenuation on one side of the star forming regions. Therefore the heating mechanisms driving the emission of 8,160 and 250 μm are UV photons escaping from the edges of star forming regions not obscured by the dense dust lanes. These tend to be towards the outside edges of the spiral arms, where the density of dust is lower. This leads to less extinction of the UV photons, allowing them to heat the PAHs as well as the larger dust grains seen at 160 and 250 μm.

The 8 to 250 μm relationship in M51 has a similar look to the 8 to 24 μm relationship. The scatter shows that there is little relationship between the 8 and 250 μm emissions. The plot shows the relationship whereby the majority of the points lie below the best fit line. At the bright end it appears the 8 μm emission is suppressed relative to the 250 μm cold dust, this is indicated by the drop off from the best fit line in the top panel of Figure 5.7. The plot of the 8/250 vs 250 μm shows the 8 μm emission decreases with strong 250 μm surface brightness. The turnover point is around log $I_\mu(250\ \mu m) = 2.5$ Jy arcsec^{-2}. This shows the mechanisms which are heating the 8 μm emission relative to the 160 and 250 μm are different to both M83 and NGC 2403. This could be because the two species have separate heating mechanisms. In this regime the strength of the PAH 8 μm emission is dependant on the environment and the heating sources.

5.2 NGC 2403

For NGC 2403, we have a comparatively good understanding of the relationship between the 8 μm PAH emission and 24 μm hot and 160 and 250 μm cold dust. To first order looking at the surface brightness, the 8 μm emission is strong in regions where the 24 μm emission also peaks. However, the ratio plot showing the 8/24 μm colour variations show a different picture. Here the 8 μm emission is suppressed relative to the 24 μm surface brightness. This relationship is demonstrated in Figure 5.3.

We see the 8 and 250 μm emissions are correlated, as the surface brightness plots exhibit the same structure. This is also demonstrated by Figure 5.7 showing the 8 μm PAH emission and the 250 μm cold dust emission probably have the same heating sources as demonstrated by the linear relationship and the 8/250 vs 250 μm panel, showing an increase in 8/250 μm emission when the 250 μm surface brightness increases. To further examine if these have the same heating mechanisms, we plot the 8/250 vs 3.6 μm emission in Figure 5.8. We see a correlation between these two emission mechanisms indicating the 8 and 250 μm emission mechanisms are driven by emission traced out by the 3.6 μm band. We know the 3.6 μm emission traces out the evolved stellar population, and furthermore we see enhancement of both the 8 and 250 μm in the centre of the galaxy where the 3.6 μm peaks. These relationships are shown graphically in Figures 5.1 and 5.9. This points towards a picture where the PAHs are mixed in with the diffuse cold dust seen at 250 μm. The implications for this are the 8 μm PAH emission is probably driven by the same mechanisms that heat the 250 μm emission from large dust grains. Since these are known to be heated by the ISRF, traced out by the 3.6 μm stellar emission, as shown by Bendo et al. [2012a]., the PAHs are found in the same regions the large dust grains are. These results indicates that the PAHs are heated by the same sources as the 250 μm cold dust is. They could be mixed in with the larger dust grains and heated by the ISRF.

The plots for the 8/250 μm ratio, 160/250 μm ratio and 3.6 μm shown in Figure

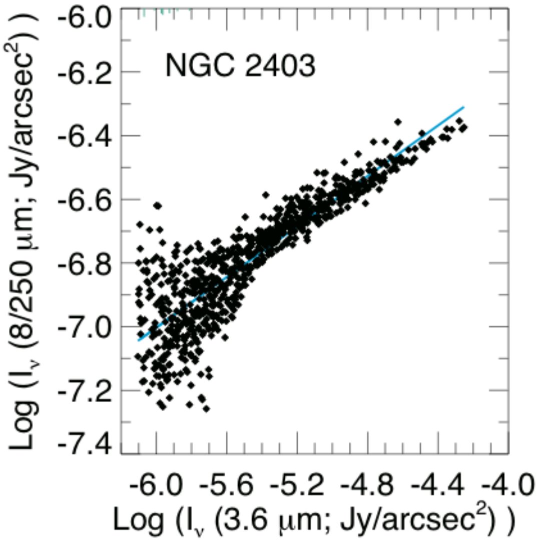

Figure 5.8: 8/250 μm colour variation as a function of 3.6 μm stellar emission for NGC2403.

5.9 The 8/250 μm shows the 8 μm emission increase with 250 μm surface brightness. We see similar structure between the 8/250 μm ratio and 3.6 μm surface brightness. This shows both the 8 μm and 250 μm emissions scale with the 3.6 μm surface brightness tracing out the evolved stellar population. The 160/250 μm ratio shows the 160 μm emission carriers are not associated with the 3.6 μm surface brightness, so these have different heating mechanisms to the 8 and 250 μm emission carriers.

In order to test this picture, we compare the 3.6 μm surface brightness to the 8/250 μm ratio shown in Figure 5.9. This along with the PAH 8 μm contour, show the 8 μm emission correlates well with the evolved stellar population, which heats the cold dust as shown by Bendo et al. [2012a].

With M83, as discussed in section 5.3 the 8 μm emission is strongly related to the 160 and 250 μm surface brightness. As this galaxy is similar to NGC 2403, in terms of the 250 μm to 8 μm relationship, it was decided to perform this analysis with NGC 2403. The comparison between the 160/250 μm and the 8/250 μm ratio is used to try and put constraints on the heating sources of the PAH 8 μm emission. We assume here, that the diffuse dust emitting at 160 μm is heated by light escaping the star formation regions, hence the contour plots in Figure 5.1 are similar for the 24 and 160 μm emission. The 250 μm as has been shown by Bendo et al. [2012a] to be predominantly heated by the evolved stellar population. We compare the 8/250 μm ratio to the 160/250 μm ratio to look at the differences in enhancement of the PAH at 8 μm and the diffuse dust heated by the star formation regions. This tests the relationships between the 8 and 160 μm emission and 8 and 250 μm together. The ratio plots for both are shown in Figures 5.4 5.9. These show the colour variations trace out the same structure in both the 160 μm and 250 μm dust emission. The PAH 8 μm and 160 μm emission are both enhanced in the star forming regions relative to the 250 μm cold dust.

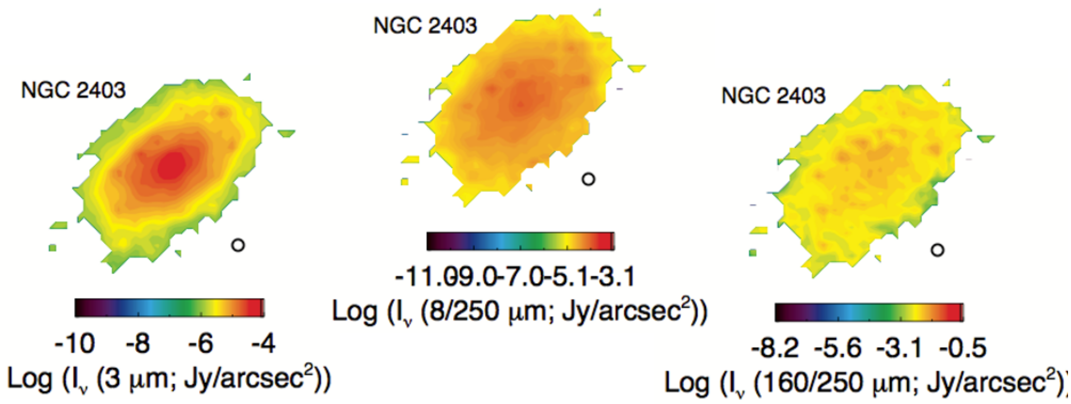

Figure 5.9: Contour plots of NGC 2403, from left to right, 3.6 μm, 8/250 ratio and 160/250 μm ratio plot, showing the colour variations of the galaxy. The circles represent the 18 arcseconds bins for the galaxy.

The Figure, 5.10 plots this relationship between the 8/250 μm ratio and the 160/250 μm ratio. The large amount of scatter demonstrated the 8 μm emission is more dependant on the 250 μm surface brightness than the 160 μm surface brightness, despite the better correlation coefficient for the 8 to 160 μm relationship. We see the 8/250 μm ratio increases much more than the 160/250 μm ratio.

The implications of this are the PAHs are mixed in with the large dust grains and a fraction of these are heated by the star forming regions as well as the large dust grains are heated to beyond 5 K and emit at 160 μm. Figure 5.10 shows a huge amount of scatter though so this relationship is not as apparent as is shown in the colour variations. It can be argued, that there is so much scatter that any relationship is difficult to see. Evidence for a relationship also breaks down when considering the 8/24 μm relationships, where the PAHs are destroyed in the star

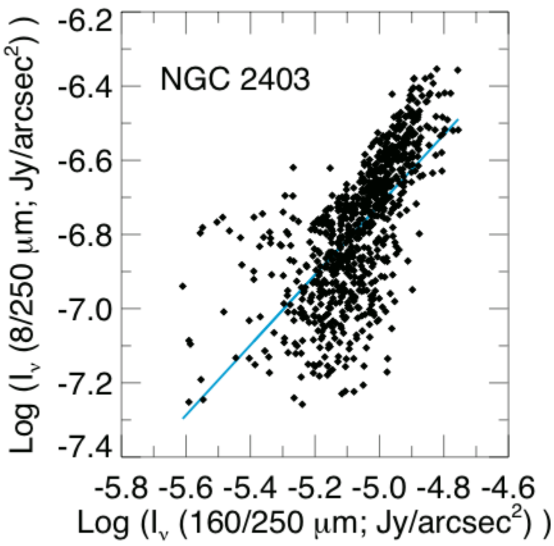

Figure 5.10: Plot of NGC 2403 for the 8/250 μm vs 160/250 μm ratios.

Table 5.4: Table showing the heating mechanisms for 8, 24, 160 and 250 μm emission in NGC 2403

Dust emission wavelength (μm)	Heating source
8	Evolves stellar population seen at 3.6 μm
24	Young stars and star formation
160	Most likely young stars and star formation, with some contribution from the evolved stellar population
250	Evolved stellar population seen at 3.6 μm

forming regions. The correlation between the 160/250 μm and 8/250 μm arises from the UV photons escaping these regions and heating the PAH shells around these areas.

For this galaxy then the PAHs are predominantly heated by the ISRF as shown by the excellent correlation between the 8,3.6 and 250 μm surface brightness maps. This is also seen in Figures 5.6 and 5.8, where the 8 μm is tightly correlated with the 250 μm emission which is heated by the 3.6 μm infrared emission from the evolved stars. We summarise the findings for the heating sources of PAHs and dust seen at 8, 24, 160 and 250 μm in NGC 2403 in Table 5.4.

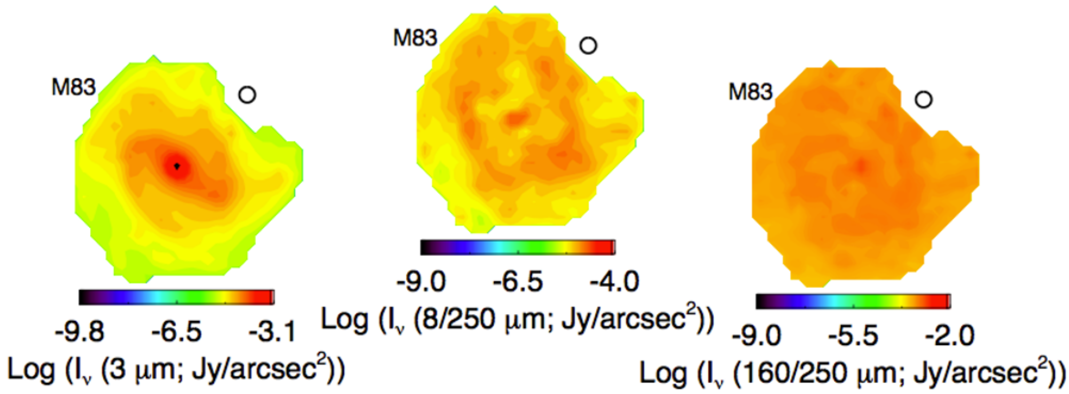

Figure 5.11: Plot of the 3.6 μm, 8/250 μm and 160/250 μm ratios for M83. The circles represent the 18 arcseconds bins for the galaxy.

5.3 M83

The results from the 8 μm to 24 μm relationship are similar to NGC 2403, in that areas of strong 24 μm emission we see the 8 μm emission is inhibited. The implications of this are the PAHs are being destroyed in areas where star formation occurs. The relationship with 160 μm emission from diffuse dust heated by star formation at a distance is the strongest we encountered, with the heating sources of the 8 μm PAH emission being the same as the heating sources for the 160 μm dust emission. The 8 to 250 μm relationship shows a similar correlation, though it is not as strong as the 160 μm.

We want to see if the heating sources for the 8 μm PAH emission are in some way connected to the 3.6 μm stellar emission. The correlation for the relationship between the 8/250 μm ratio and 3.6 μm emission for NGC 2403, shows the heating sources for both the 8 μm emission and 250 μm emission are connected to the 3.6 μm emission, as shown in Figure 5.12. We find that the 8/250 μm colour increases with the 3.6 μm then the ratio drops off towards the bright end. The contour map of the 3.6 μm This relationship shows, that the 8 μm emission is not that well connected to the 3.6 μm surface brightness as is the case for NGC 2403. This implies that in M83, the PAHs are being excited by a source other than the stellar population seen in the 3.6 μm.

We find the 160/250 μm ratios can provide clues as to whether the 8 μm PAH emission is more associated with the enhancement within the spiral arms or heated

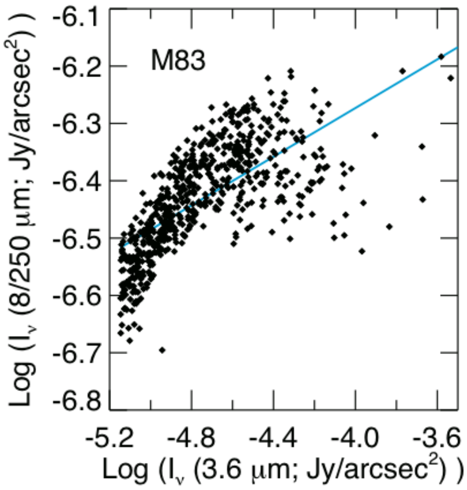

Figure 5.12: 8/250 μm colour variation as a function of 3.6 μm stellar emission for M83.

by light escaping the star forming regions. The contour plots of the colour variations of these ratios are shown in Figure 5.11. Here the 160/250 μm colour variations show the spiral arm structure, with the 160 μm dust being strongest towards the outer edges of the spiral arms. The star forming regions, are present though not as well defined as in the 24 μm contour plots shown in Figure 5.1. The 160/250 μm relationship shows the dust heated at a distance from light escaping the star forming regions. One probable explanation for this is the strong dust extinction of areas to the inside of the spiral arms heating the PAHs at a distance. This coincides with the 8 μm to 160 μm relationship, where the PAHs and 160 μm emission component of dust correlate well. Figure 5.13, plots this relationship. The plot shows an excellent correlation between the 8/250 and 160/250 μm relations, this is expected as the 8 and 160 μm emissions are correlated. Here the plot shows the 8 μm and 160 μm enhancement relative to the dust mass. What is seen here is the correlation between the 8 and 160 μm emission. The data here show more evidence for the 8 μm emission to be more correlated with the 160 μm surface brightness than the 250 μm surface brightness.

We make line cuts across two locations in M83, shown in Figure 5.14 The locations are a typical cross sections of the spiral arms of this galaxy. We have produced these to look at how the relationships between the 8 μm emission and dust vary

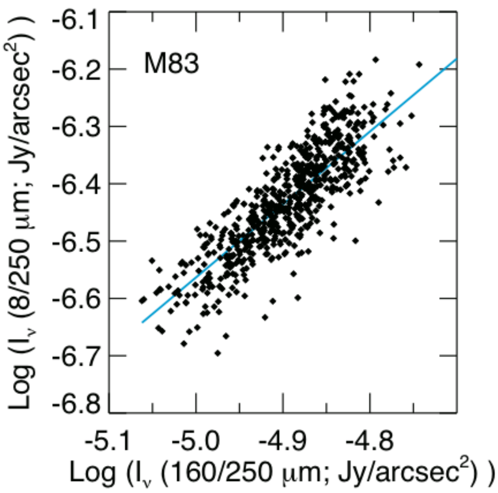

Figure 5.13: Plot of the 8/250 μm vs the 160/250 μm ratios for M83

across the spiral arms, as we see some offset of the 8/250 μm as well as 160/250 μm in the contour maps in Figures 5.6 and 5.4.

The data for the line cuts are selected as they trace various dust and dust excitation modes. The relations used, are the 250 μm tracing dust mass; the 8/250 μm ratio tracing the PAH enhancement; 24/250 μm which is local heating by star forming regions; and finally the 160/250 μm showing the heating by light escaping the star forming regions.

The 160/250 μm relationship is flat in both arms, indicating the light escaping from the star formation regions is the dominant process heating the dust. The peak of the 8/250 μm relation is offset towards the outer edges of the spiral arms, and appears to be correlated with the 160/250 μm relationship. This indicates the heating of the PAHs and diffuse dust is due to the light escaping from the star formation regions. The localised dust heating traced out by the 24/250 μm ratio also peaks in the same regions of the spiral arms, but drops off quicker than the diffuse dust emission shown by the 160/250 and 8/250 μm PAH enhancement. The regions towards the inside of the spiral arms show a decrease in intensity for all the data plotted. This is evidence for large amounts of dust extinction suppressing both the PAH and other dust emission in the intra arm regions.

The interpretation of this result from the line cuts with PAH enhancement towards the outer edges of the spiral arms, shows that the large amount of dust

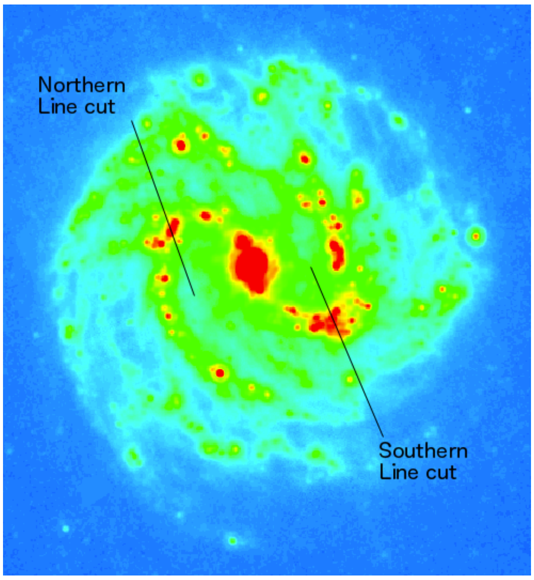

Figure 5.14: 24 μm image of M83 showing the two linecuts. The northern line and the southern line are both analysed.

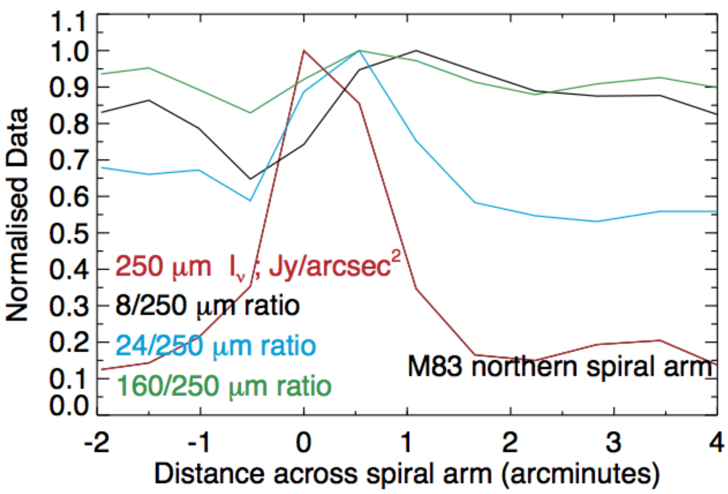

Figure 5.15: Plot of M83 north line cut. The data are normalised and zeroed on the x axis where the 250 μm emission peak.

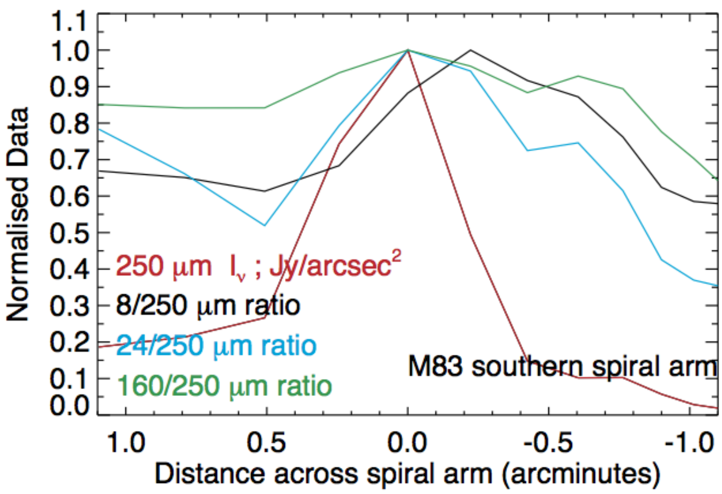

Figure 5.16: 24 μm Plot of M83 south line cut. The data are normalised and zeroed on the x axis where the 250 μm emission peak.

Table 5.5: Table showing the heating mechanisms for 8, 24, 160 and 250 μm emission in M83

Dust emission wavelength (μm)	Heating source
8	Light escaping star forming regions
24	Young stars and star formation
160	Similar to 8 μm PAH heating, with light escaping star forming regions
250	Evolved stellar population seen at 3.6 μm

extinction is shielding the PAHs in the intra arm regions towards the inside of the galaxy. We can say the heating sources for the PAHs are similar to the 160 μm dust emission, which is shown to be light escaping from star forming regions. We summarise the heating sources for PAH and dust seen at 8, 24, 160 and 250 μm in M83 in Table 5.5.

5.4 M51

The relationship between the 8 μm PAH emission and dust emission is more complicated than in M83 and NGC 2403. The PAH 8 μm to 24 μm hot dust emission is similar to the other galaxies, where the high intensity emission from the star formation regions is destroying the PAHs. The relationship with the diffuse dust is a bit

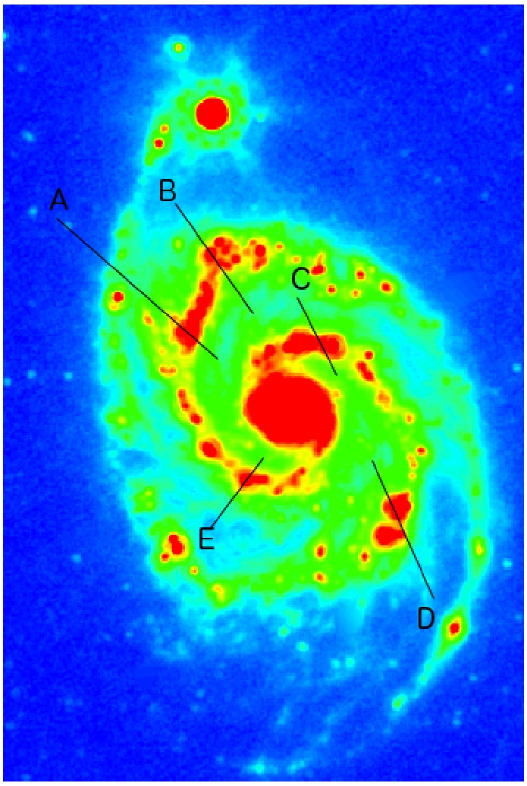

Figure 5.17: 24 μm image of M51 showing the location of the line cuts. Clockwise from left:
A) North east line cut.
B) North Line cut.
C) Northern inner line cut.
D) Southern line cut.
E) Eastern linecut.

more challenging. Here we do not see an obvious correlation for either the 160 μm dust or the 250 μm dust.

In order to analyse these relationships further, line cuts were taken across five areas of the galaxy. These represent the inner spiral arms and the outer spiral arms. Here we hope that these line cuts give a good profile of the dust emission across the galaxy as a whole. The data here for the line cuts were sampled at two intervals for each pixel. This gives a slightly higher resolution and smooths out the peaks slightly. This was done to better resolve the location of the peak of the emission for each relationship.

Line cuts are needed to see what is happening across the spiral arms because there is not much of a discernible relationship between the 8 μm PAH emission with dust at 24, 160 and 250 μm emission. To analyse the galaxy properly, it was decided

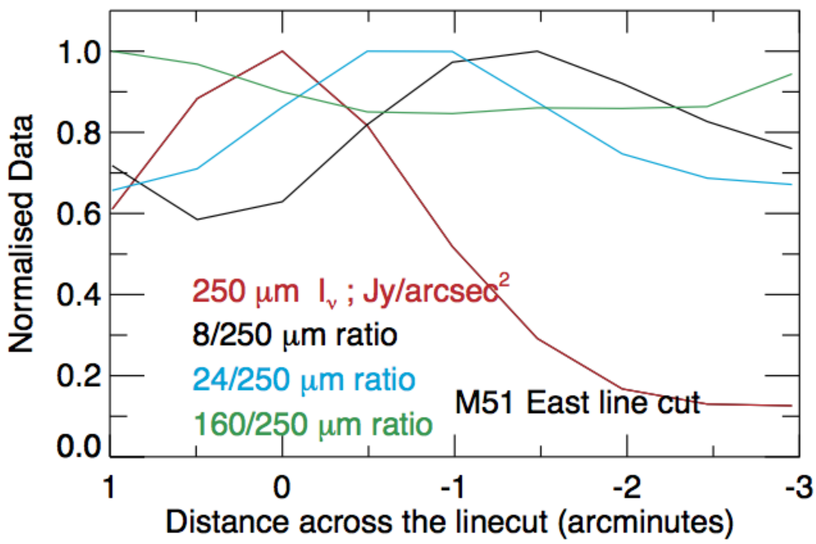

Figure 5.18: Profile of the east line cut. The data are normalised and zeroed on the x axis where the 250 μm emission peaks.

to take each spiral arm separately as well as look at the inner and outer regions of these spiral arms. In total, 5 line cuts were made, these are shown in Figure 5.17. When producing the data for the line cuts we decided to sample it at twice the pixel count, generating two data points for every pixel. We see more structure using this sampling technique. The data are normalised and shown here are the 250 μm tracing dust mass; the 8/250 μm ratio tracing the PAH enhancement; 24/250 μm, local heating by star forming regions; and 160/250 μm showing the heating by light escaping the star forming regions.

The suppression of the 8 μm emission relative to the dust is apparent in both the spiral arms. The 160/250 μm ratio is again fairly flat across the galaxy. It peaks towards the outer edges of the spiral arms for each line cut, except for the eastern line cut, which shows the inner region of one spiral arm. Here the 160 μm emission is suppressed relative to the 250 μm dust emission. For the rest of the line cuts, this is not the case. We do see the 8/250 μm ratio peaks towards the outer edges of the spiral arms across the whole galaxy, the relationship with the diffuse dust either localised heating or heating at a distance is different across the two spiral arms.

For both spiral arms the trend is for the local dust heating to peak on the outer regions of the spiral arm. The 160/250 μm ratio peak moves towards the peak dust

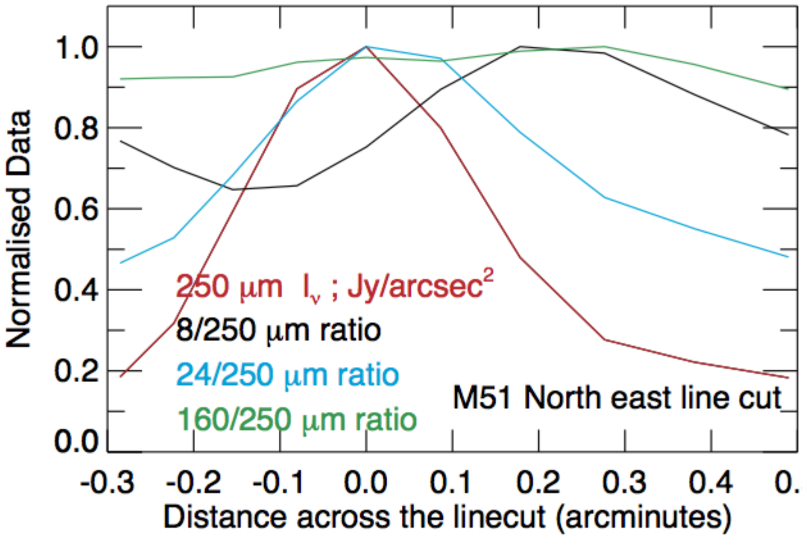

Figure 5.19: Profile of the North east line cut. The data are normalised and zeroed on the x axis where the 250 μm emission peak.

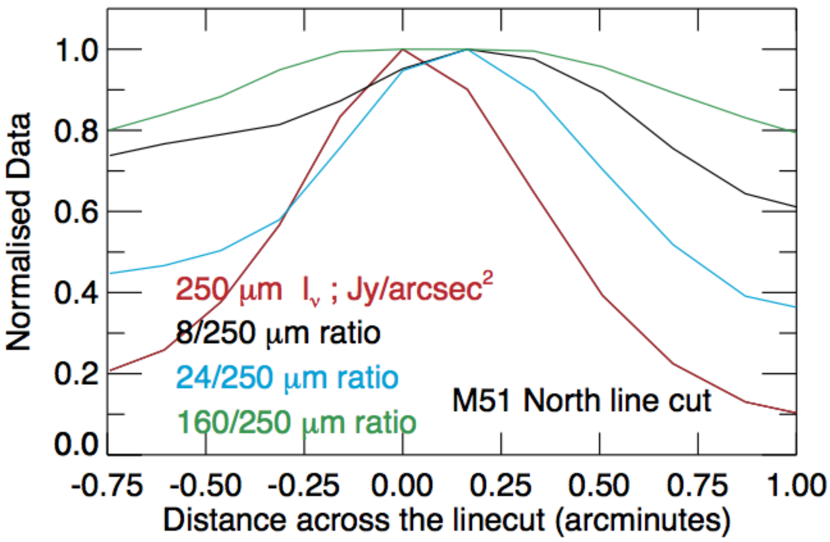

Figure 5.20: Profile of the North line cut. The data are normalised and zeroed on the x axis where the 250 μm emission peaks.

mass as traced out by the 250 μm data. This shows the star forming regions could be heating the larger grains as well as the smaller grains. Generally the 8/250 μm ratio tracing out the PAH enhancement also lies on the outer edge of the spiral arms. In the regions closer to the nucleus, this ratio is more associated with the 160/250 μm ratio. This shows the PAHs are being excited by the same UV photons that are escaping the star forming regions and heating the dust at a distance. The lack of a correlation between the 8 and 3.6 μm and relationship between the 24/250 μm and 8/250 μm suggests the PAHs are more sensitive to the 24 μm surface brightness in M51 than the PAHs in NGC 2043 and M83.

The northern spiral arm is shown by Figures, 5.18, 5.19 and 5.20. We see the 8/250 μm emission peaks follow the trend of the of the localised heating shown by the 24/250 μm ratio. This is still offset towards the outer edge, but has a stronger relationship to the blue line tracing the localised dust emission from UV light escaping the star forming regions. Moving outwards along the spiral arm, The 160/250 μm and 8/250 μm ratio peaks become closer to the 250 μm peak tracing out the dust mass. This could mean the 8 μm enhancement is becoming closer to the star formation regions. We see in the other two line cuts, the 8/250 μm ratio closely follows the 160/250 μm ratio. This is indicative of the PAHs being heated by the star forming regions, but are mixed in with the diffuse dust and the radiation powering this emission is also driving the PAH 8 μm emission.

For the southern spiral arm, shown in Figures 5.21 and 5.22, the 8/250 μm ratio peaks on both sides of the spiral arm, and is further beyond the 160/250 μm ratio. This shows that the PAH enhancement in this spiral arm is slightly different to the other spiral arm. Here we find the 8 μm emission is not closely associated with the 160 μm dust emission. We see the localised heating on both sides of the dust mass for this spiral arm. There is no correlation between the 8/250 μm to the 160/250 μm ratio. This shows that the PAH enhancement for this spiral arm is due to heating by the UV photons at a distance in regions where the The lack of a correlation as described in sections 5.1.1, 5.1.2 and 5.1.3 are demonstrated here. The 24/250 ratio peak is broader than the 250 μm data tracing the dust mass. This shows that

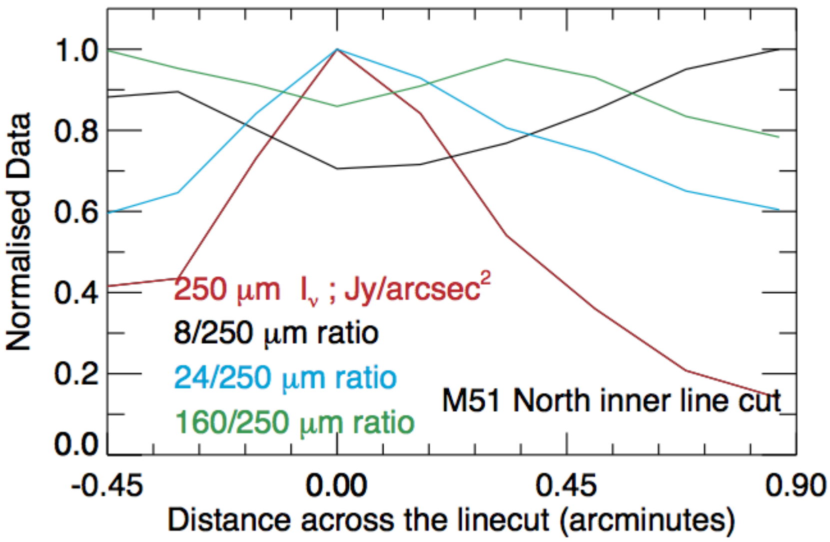

Figure 5.21: Profile of the inner southern arm cut. The data are normalised and zeroed on the x axis where the 250 μm emission peaks.

this spiral arm has a more symmetrical composition that the northern arm. This is evident in the inner line cut as the 8/250 and 160/250 μm ratios are enhanced on both sides of the peak dust mass. The 8/250 ratio here is more closely related to the 160/250 ratio indicating that the PAH heating for this spiral arm is more sensitive to the 160 and 250 μm surface brightness than the 24 μm surface brightness.

For this galaxy it appears there are two separate processes in each spiral arm contributing to the 8 μm PAH heating. For the northern spiral arm, the largest contribution to PAH enhancement are UV photons heating the PAHs on a local scale. The southern spiral arm shares the traits with M83, whereby the PAH enhancement is seen much further from the dust mass and is more closely linked with the 160/250 μm data than the 24/250 μm data.

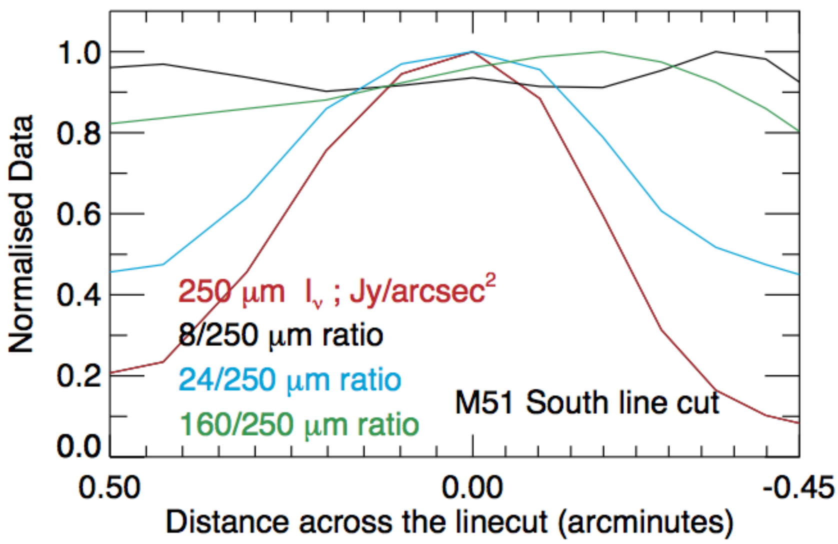

Figure 5.22: Profile of the southern line cut. The data are normalised and zeroed on the x axis where the 250 μm emission peaks.

Chapter 6

Discussion

6.1 Discussion

6.1.1 Discussion of 8 μm PAH to 24 μm Hot dust Relationship

The results from Section 5.1.1, show that that generally the 8 and 24 μm emission do correlate to some degree for all three galaxies, this is shown in Figure, 5.3. However, the results show the 8/24 μm ratio decreases in areas where the 24 μm emission peaks.

Previous results from ISO have suggested that the PAH to hot dust ratio should be uniformly spread across the disc of galaxies. Roussel et al. [2001] have produced a reasonable calibration of 7 μm an 15 μm PAH emission as star formation tracers. Helou et al. [2004] have demonstrated a relation between PAH emission and hot dust emission. Here they show, that the PAH emission peaks around the strong hot dust emission. This is the same behaviour we see in both the grand design spirals, but in NGC 2403 the picture is different, with strong peak 8 μm emission in the centre as well as around the strong 24 μm hot dust emission. Calzetti et al. [2005] show that the PAH 8 μm emission is lower than other star formation tracers including 24 μm hot dust emission, in star forming regions in M51.

Helou et al. [2004], Bendo et al. [2006, 2008], Gordon et al. [2008] show the 8 μm

PAH emission is inhibited in regions with strong 24 μm hot dust emission tracing out star formation. The results show that on local scales the 8 μm PAH emission does not scale with the 24 μm hot dust emission. Our results agree with their findings.

Models of dust emission by Li and Draine [2001], Draine et al. [2007] show the 24 μm emission can arise from dust heating by a strong ISRF as well as contributions from star forming regions. The emission from these dust grains can make the 24 μm emission appear over luminous compared to the 8 μm emission.

Our results suggest that the PAHs may be destroyed in star forming regions. This is in agreement with Madden et al. [2006], who suggest that the PAHs are destroyed in intense star forming regions or areas with high intensity photons. Our analysis shows the 8/24 μm ratio declines steeply in star forming regions.

6.1.2 Discussion of 8 μm PAH to 160 & 250 μm Cold Dust Relationship

The data shown in Sections 5.1.2 and 5.1.3 show the excellent correlation between the cold dust in both the 160 μm and 250 μm for M83 and 250 μm for NGC 2403. The ratio of 8/160 μm in M83 shows an almost one to one correlation, where the 8 μm PAH emission is strongly dependant on the 160 μm surface brightness. M51 has a slightly weaker correlation, but there is still evidence for a relationship. However, in each of the spiral arms, from the line cuts seen in Figures, 5.18 to 5.22, the relationship varies across the galaxy. Towards the centre of the galaxy the 8 μm PAH emission is suppressed relative to the dust mass, in the spiral arms. The diffuse dust in the outer spiral arms traced by the 160/250 μm ratio and the 8 μm PAH emission traces out the diffuse dust heated by UV photons escaping from star forming regions.

The results here are in agreement with data from ISO, where Haas et al. [2002] have shown a relationship between the 850 μm cold dust and 7.7 μm PAH emission line. This suggestion from the authors is that the PAHs are mixed in with the diffuse ISM, this is what is happening in NGC 2403. However, the data that Haas have used, is not a good sample as it uses only edge on galaxies and the 850 μm data is taken from a ground based telescope so the signal to noise ratio is poor Bendo et al. [2008] have shown the 8 to 160 μm relationship correlates very well and scales well over distances of $\sim$ 2kpc. Though the data are taken before the Herschel space telescope provided evidence for cold dust radiating at temperatures longer than 160 μm. This was at the time assumed to be the emission component from diffuse dust heated by the ISRF. With the data presented here in section 5 the 250 μm data trace out the diffuse dust heated by the evolved stellar population, and the 160 μm traces dust heatied by star formation regions Foyle et al. [2013].

Rowan-Robinson et al. [2010], Calzetti et al. [2010], Bendo et al. [2012a], Boquien et al. [2011], Groves et al. [2012] all show the main contributions to dust heating of larger grains is from the evolved stellar population. Here we are using the 3.6 μm to trace out the stellar population. From this, we find the majority of the energy for the PAH 8 μm emission in NGC 2403 is probably due to the evolved stellar population and not the star forming regions.

Several authors have looked at using molecular gas and PAH relationships, Regan et al. [2006], Bendo et al. [2010], Vlahakis et al. [2013] all show a correlation between PAH emission and molecular gas. The molecular gas here traces out the diffuse dust and can relate the PAH mass to tracing star formation.

The reasons for the differences in heating mechanisms across the sample are partly due to the Hubble type, where M51 and M83 are grand design spiral types, the UV photons escaping the star forming regions tend to be absorbed by dust lanes towards one side of the spiral arms, this dust extinction inhibits the PAH emission in these areas causing the PAH 8 μm emission to be suppressed here. We see this effect in the line cuts of M83 and M51 shows the 8 μm emission suppressed relative to the 250 μm tracing out the dust mass. NGC 2403 is a flocculant type so the UV photons from the star forming regions should be able to escape in all directions. Yet we do not see the same correlation between the 160 μm and 8 μm emission as in M83. The heating mechanisms of the ISM and PAH emission look similar to a first order. When comparing the 3.6 μm data to the 8 μm PAH data it becomes clear that the PAHs in NGC 2403 are more closely related to the evolved stellar population than in M83.

The conclusions drawn are the nature of the galaxy is a factor in the PAH to dust relationship. It could be that because NGC 2403 is a flocculant type galaxy, so we don't see dust lanes building up in the spiral arms. This is evidence for the PAHs in this galaxy to be mixed in with the diffuse dust which is heated by the diffuse radiation from the evolved stars. The grand design galaxies, in particular M83, show that the PAHs are excited by light escaping from the star forming regions. The PAHs have an offset from the dust and gas mass, where the majority of the star formation is taking place. Here we see the light escaping the star forming regions and heating the PAHs mixed in with the diffuse dust.

6.1.3 Interpretation of 8 μm PAH As Star Formation Tracers

Our results show the PAH emission is not correlated with star formation on a local scale, this is shown best in Figures, 5.3 and 5.2, where the 8 μm PAH emission is suppressed in areas where the 24 μm emission is strongest. This isn in agreement with Calzetti et al. [2005, 2007]. We do find a correlation between the PAH emission and 24 μm emission on a global scale. Figure 5.3 shows this relationship, we could potentially use the PAH 8 μm emission to trace global star formation across the whole disk of the galaxy. This assumption that the globally integrated PAH 8 μm can trace star formation on a global scale relies on assumptions that the PAH 8 μm emission is directly related to the star formation and not indirectly as described by the Kennicutt-Schmidt law. Several authors have shown the PAH emission strength is a factor of the environment and metallicity, Engelbracht et al. [2005], Madden et al. [2006], Draine et al. [2007]. From out results an those of others, the PAH 8 μm heating mechanisms are much more complicated that a relation to star formation.

We find correlation between the 8 μm emission and the 160 μm emission and the 8 μm to 250 μm emission in all three galaxies, is better than the correlation between the 8 μm and 24 μm emission. The relationship between the 8 μm and 160 μm emission in M83 shows the 8 μm emission is enhanced in areas near the star forming regions. This can be evidence to show that in some cases we can use the 8 μm PAH emission to trace star formation on a global scale.

Using the Kennicutt-Schmidt law Schmidt [1959b] we can trace star formation by looking at PAH to dust mass relationships. The 8 μm emission is related to the dust mass, and the dust mass is in turn related to the gas mass. The gas mass is related to the star formation rate through the Kennicutt-Schmidt law and we can use this relationship to link the global PAH emission to star formation, even in galaxies where the PAHs are not heated by the star forming regions. This is the case we see in NGC 2403.

The problems with correlating the two relationships here on a global scale can also relate back to the dust models produced by Li and Draine [2001], Draine et al. [2007], showing the 24 μm emission can also appear in diffuse dust. This means that the 24 μm hot dust emission is not just produced by star formation, and can arise from dust heating by a strong ISRF as well as contributions from star forming regions. The emission from these dust grains can make the 24 μm emission appear overluminous compared to the 8 μm emission in these areas making both tracers of star formation unreliable.

We conclude the use of 8 μm PAH emission to trace star formaiton is very unreliable on the local scale due to its inhibition in strongly ionizing regions, where the PAH emission is suppressed relative to the 24 μm hot dust emission. We therefore see the PAH emission in the star forming regions being under luminous, this agrees with Calzetti et al. [2005], so using PAH emission as a local SFR tracer should not be attempted. On global scales where the PAH excitation can be due to the ISRF, the relationship between the PAH emission and heating source, can lead to one or more mechanisms for heating the PAHs, as well as destruction by intense UV photons, as shown by Draine et al. [2007], leads to a complex relationship between the PAH emission and star formation rate.

6.1.4 Producing Models of Dust Mass Using 8 μm PAH Emission

From Section 6.1.3 we see the 8 μm PAH emission does not trace star formation on a global scale. The 8 μm emission in all three galaxies is well correlated with the 160 and 250 μm emission. Furthermore, the correlation between the 8 μm and 8/160 μm ratio with the 160 μm surface brightness, as well as the correlation between the 8 μm and 8/250 μm ratio with the 250 μm surface brightness, show we can use the 8 μm emission to trace dust being heated through different mechanisms. From these results we can say that there is no one method to fit the dust mass to the 8 μm emission.

Both the 160 and 250 μm emission components trace thermal emission from large dust grains, with the 160 μm being warmer than the 250 μm emission. The 250 μm emission originates from the coldest dust within the galaxy [Bendo et al., 2012a]. For a given surface brightness, the temperature scales with the dust mass, such that the warmer component of the emission originates from a smaller fraction of the dust mass, compared to the colder emission. Hence, the 160 μm emission traces out a smaller fraction of the dust mass than the 250 μm emission component. The 250 μm emission component should trace the majority of the dust mass. The heating sources for these dust emissions are different, with the emission seen at 160 μm being heated by the light escaping the star forming regions [Boquien et al., 2011]. The dust seen at 250 μm is heated by the diffuse ISRF and evolved stars, [Calzetti et al., 2010, Boquien et al., 2011, Bendo et al., 2012a, Groves et al., 2012, Smith et al., 2012].

We find for NGC 2403 the 8 μm emission is best correlated with the 250 μm emission, with the 8/250 μm ratio is dependant on the 250 μm surface brightness. This implies the 8 μm emission is associated with the cold dust within this galaxy. As the dust emission at 250 μm traces out the majority of the dust mass within NGC 2403, the PAHs are mixed in with the diffuse dust and are able to accurately trace the majority of the dust mass within this galaxy.

For M83 and to an extent M51, we find the 8 μm emission is better correlated with the 160 μm emission. In M83 the 8/160 μm ratio has a relationship which approaches uniity with the 160 μm surface brightness. This shows the 8 μm emission is physically linked to the 160 μm emission. We find the relationship in M51 changes with the region identified, this is shown in section ??. We show that for M83 it is possible to use the 8 to 160 μm relationship to use the PAHs to trace out some of the diffuse dust within the galaxy.

For M51, it is still possible to produce a global relationship. We see a similar, but much worse dependance of the 8/160 μm on the 160 μm surface brightness. The local relations show that in some regions the 8 μm emission is inhibited relative to the dust at 160 μm.

The interpretation of our findings for all three galaxies, shows three different cases to relate the PAHs to the dust mass. For the flocculent type galaxy, there is a relationship with the majority of the cold dust mass, as seen at 250 μm. In M83, we see the PAHs show an almost one to one relationship with the slightly warmer dust emission component seen at 160 μm. This will be an underestimation of the dust mass, due to the 160 μm emission originating from a fraction of the dust mass as it is not emitted by the coldest dust. In M51, we see different mechanisms at work, so it is difficult to produce a global relationship between the PAHs and the dust mass in the galaxy.

6.1.5 Implications for Dust Emission And Radiative Transfer Models

We show the 8 μm emission is inhibited in environments with a strong ISRF, either due to star formation, or a very intense ISRF. Therefore a model with the dust and PAH component is difficult to produce as the radiative transfer mechanisms of the PAHs are dependant on the environment. We see the spiral arms effect the radiative transfer mechanism of the dust and PAHs whereby the PAHs are suppressed behind areas with relatively high dust extinction, and in most cases we see enhancement of the PAHs in regions towards the outer edges of the spiral arms. In some areas of

M51, the PAHs are suppressed relative to the dust emission components at 160 μm. Currently only some models account for how the spiral arms affect the dust and PAH heating. Other models investigated the effects of spiral arms, Popescu et al. [2011] shows no effect when considering the integrated dust emission SED and the attenuation of starlight from younger stars. This is not the case for the grand design galaxies, where we see the dust attenuation of UV photons escaping the star forming regions. This attenuation is particularly present in M83 just to the inside of the spiral arms, and the majority of the dust mass.

Models by Draine et al. [2007] do not account for the dust geometry, this could also be an important factor in the dust emission. Our results do not account for the dust geometry as well. We can say that their models still hold true for our results. Our results show that the spiral arm density waves heavily attenuate the energy from young stars, as well as having an effect on local PAH and dust heating, the PAH heating sources in the grand design galaxies appear to be better correlated with the heating sources for the dust associated with the star formation regions.

We find that there is no single model to predict the dust emission and radiative transfer can fit a SED of all three galaxies and accurately show the PAH relation to dust emission as a function of both excitation and emission. We see the different heating sources for 8 μm PAH emission in all three galaxies, in NGC 2403, the dominant heating source is the ISRF, whereas, for M83 photons escaping star formation, which are not attenuated are responsible for both the 8 μm PAH heating and the diffuse dust. In the case of M51, depending upon the region, we see PAH enhancement correlates with the dust heating to 160 μm, and in other areas, the PAHs are inhibited. The best models to fit this will take into account the differences in excitation and emission on scales of a few kpc or less. At current levels the radiative transfer of energy to the PAH and dust through heating and emission is too complicated to fit one general case for a SED to the sample.

6.1.6 Future Prospects

Our data here show differences between the PAH and dust emission for three broadly similar Hubble type galaxies. The first way we could improve out understanding of the PAH to hot and cold dust relationship is to extend the analysis to include a wider range of Hubble types. For example we want to include elliptical as well as irregular galaxies. Elliptical galaxies with Hubble types including E0 to E7 will allow the PAH to dust relationship to be analysed in galaxies without strong dust lanes.

As well as more loosely wound spiral galaxies such as SAo, SBd and SBm types, where the spiral arms are much more diffuse in nature and no bulge is present. To analyse the relationship between the PAHs and dust in with a stronger bulge and bars, this will allow the relationship in dust lanes to be analysed. These would include Hubble types SBa and SBd. We would be able to perform more line cuts to look at the relationship between the PAHs and duast across the spiral arms

Within this sample we will be be able to develop a more global picture of PAH and dust emission in galaxies. An increase in sample size with the same analysis would provide more insight into the use of 8 μm PAH emission as a tracer for star formation, as well as relations to dust emission models of galaxies.

Another follow on is to change the analysis, here we look at the global relationships for all three galaxies for the 8 to 24, 160 and 250 μm. By selecting discrete regions, it may be possible to develop a further understanding of the 8 μm PAH to dust emission relationships.

Bibliography

L. J. Allamandola, A. G. G. M. Tielens, and J. R. Barker. Interstellar polycyclic aromatic hydrocarbons - The infrared emission bands, the excitation/emission mechanism, and the astrophysical implications. ApJS, 71:733–775, December 1989. doi: 10.1086/191396.

G. Aniano, B. T. Draine, K. D. Gordon, and K. Sandstrom. Common-Resolution Convolution Kernels for Space- and Ground-Based Telescopes. PASP, 123:1218–1236, October 2011. doi: 10.1086/662219.

N. Bastian, M. Gieles, Y. N. Efremov, and H. J. G. L. M. Lamers. Hierarchical star formation in M 51: star/cluster complexes. A&A, 443:79–90, November 2005. doi: 10.1051/0004-6361:20053165.

F. E. Bauer, D. M. Alexander, W. N. Brandt, A. E. Hornschemeier, C. Vignali, G. P. Garmire, and D. P. Schneider. The Chandra Deep Field North Survey. XII. The Link between Faint X-Ray and Radio Source Populations. AJ, 124:2351–2363, November 2002. doi: 10.1086/343778.

E. F. Bell. Estimating Star Formation Rates from Infrared and Radio Luminosities: The Origin of the Radio-Infrared Correlation. ApJ, 586:794–813, April 2003. doi: 10.1086/367829.

G. J. Bendo, D. A. Dale, B. T. Draine, C. W. Engelbracht, R. C. Kennicutt, Jr., D. Calzetti, K. D. Gordon, G. Helou, D. Hollenbach, A. Li, E. J. Murphy, M. K. M. Prescott, and J.-D. T. Smith. The Spectral Energy Distribution of Dust Emission in the Edge-on Spiral Galaxy NGC 4631 as Seen with Spitzer and the James Clerk Maxwell Telescope. ApJ, 652:283–305, November 2006. doi: 10.1086/508057.

G. J. Bendo, B. T. Draine, C. W. Engelbracht, G. Helou, M. D. Thornley, C. Bot, B. A. Buckalew, D. Calzetti, D. A. Dale, D. J. Hollenbach, A. Li, and J. Moustakas. The relations among 8, 24 and 160 μm dust emission within nearby spiral galaxies. MNRAS, 389:629–650, September 2008. doi: 10.1111/j.1365-2966.2008.13567.x.

G. J. Bendo, C. D. Wilson, M. Pohlen, M. Sauvage, R. Auld, M. Baes, M. J. Barlow, J. J. Bock, A. Boselli, M. Bradford, V. Buat, N. Castro-Rodriguez, P. Chanial, S. Charlot, L. Ciesla, D. L. Clements, A. Cooray, D. Cormier, L. Cortese, J. I. Davies, E. Dwek, S. A. Eales, D. Elbaz, M. Galametz, F. Galliano, W. K. Gear, J. Glenn, H. L. Gomez, M. Griffin, S. Hony, K. G. Isaak, L. R. Levenson, N. Lu, S. Madden, B. O'Halloran, K. Okumura, S. Oliver, M. J. Page, P. Panuzzo, A. Papageorgiou, T. J. Parkin, I. Perez-Fournon, N. Rangwala, E. E. Rigby, H. Roussel, A. Rykala, N. Sacchi, B. Schulz, M. R. P. Schirm, M. W. L. Smith, L. Spinoglio, J. A. Stevens, S. Sundar, M. Symeonidis, M. Trichas, M. Vaccari, L. Vigroux, H. Wozniak, G. S. Wright, and W. W. Zeilinger. The Herschel Space Observatory view of dust in M81. A&A, 518:L65, July 2010. doi: 10.1051/0004-6361/201014568.

G. J. Bendo, A. Boselli, A. Dariush, M. Pohlen, H. Roussel, M. Sauvage, M. W. L. Smith, C. D. Wilson, M. Baes, A. Cooray, D. L. Clements, L. Cortese, K. Foyle, M. Galametz, H. L. Gomez, V. Lebouteiller, N. Lu, S. C. Madden, E. Mentuch, B. O'Halloran, M. J. Page, A. Remy, B. Schulz, and L. Spinoglio. Investigations of dust heating in M81, M83 and NGC 2403 with the Herschel Space Observatory. MNRAS, 419:1833–1859, January 2012a. doi: 10.1111/j.1365-2966.2011.19735.x.

G. J. Bendo, F. Galliano, and S. C. Madden. MIPS 24-160 μm photometry for the Herschel-SPIRE Local Galaxies Guaranteed Time Programs. MNRAS, 423: 197–212, June 2012b. doi: 10.1111/j.1365-2966.2012.20784.x.

G. J. Bendo, M. J. Griffin, J. J. Bock, L. Conversi, C. D. Dowell, T. Lim, N. Lu, C. E. North, A. Papageorgiou, C. P. Pearson, M. Pohlen, E. T. Polehampton, B. Schulz, D. L. Shupe, B. Sibthorpe, L. D. Spencer, B. M. Swinyard, I. Valtchanov, and C. K. Xu. Flux calibration of the Herschel?-SPIRE photometer. MNRAS, 433: 3062–3078, August 2013. doi: 10.1093/mnras/stt948.

J. Bernard-Salas, S. Guiles, J. R. Houck, P. Morris, W., and S. Pottasch, R. Measuring the Metallicity Gradient in the Outer Disk of the Milky Way. *Spitzer Proposal*, page 40035, May 2007.

L. Bianchi, D. A. Thilker, D. Burgarella, P. G. Friedman, C. G. Hoopes, S. Boissier, A. Gil de Paz, T. A. Barlow, Y.-I. Byun, J. Donas, K. Forster, T. M. Heckman, P. N. Jelinsky, Y.-W. Lee, B. F. Madore, R. F. Malina, D. C. Martin, B. Milliard, P. Morrissey, S. G. Neff, R. M. Rich, D. Schiminovich, O. H. W. Siegmund, T. Small, A. S. Szalay, B. Y. Welsh, and T. K. Wyder. Recent Star Formation in Nearby Galaxies from Galaxy Evolution Explorer Imaging: M101 and M51. ApJ, 619:L71–L74, January 2005. doi: 10.1086/422685.

R. C. Bohlin, R. H. Cornett, J. K. Hill, A. M. Smith, and T. P. Stecher. Images in the rocket ultraviolet - The starburst in the nucleus of M83. ApJ, 274:L53–L56, November 1983. doi: 10.1086/184149.

M. Boquien, D. Calzetti, F. Combes, C. Henkel, F. Israel, C. Kramer, M. Relaño, S. Verley, P. van der Werf, E. M. Xilouris, and HERM33ES Team. Dust Heating Sources in Galaxies: The Case of M33 (HERM33ES). AJ, 142:111, October 2011. doi: 10.1088/0004-6256/142/4/111.

V. Buat and C. Xu. Star formation and dust extinction in disk galaxies. Comparison between the UV non-ionizing and the FIR emissions. A&A, 306:61, February 1996.

D. Calzetti, A. L. Kinney, and T. Storchi-Bergmann. Dust extinction of the stellar continua in starburst galaxies: The ultraviolet and optical extinction law. ApJ, 429:582–601, July 1994. doi: 10.1086/174346.

D. Calzetti, L. Armus, R. C. Bohlin, A. L. Kinney, J. Koornneef, and T. Storchi-Bergmann. The Dust Content and Opacity of Actively Star-forming Galaxies. ApJ, 533:682–695, April 2000. doi: 10.1086/308692.

D. Calzetti, R. C. Kennicutt, Jr., L. Bianchi, D. A. Thilker, D. A. Dale, C. W. Engelbracht, C. Leitherer, M. J. Meyer, M. L. Sosey, M. Mutchler, M. W. Regan, M. D. Thornley, L. Armus, G. J. Bendo, S. Boissier, A. Boselli, B. T. Draine, K. D. Gordon, G. Helou, D. J. Hollenbach, L. Kewley, B. F. Madore, D. C. Martin, E. J. Murphy, G. H. Rieke, M. J. Rieke, H. Roussel, K. Sheth, J. D. Smith, F. Walter, B. A. White, S. Yi, N. Z. Scoville, M. Polletta, and D. Lindler. Star Formation in NGC 5194 (M51a): The Panchromatic View from GALEX to Spitzer. ApJ, 633: 871–893, November 2005. doi: 10.1086/466518.

D. Calzetti, R. C. Kennicutt, C. W. Engelbracht, C. Leitherer, B. T. Draine, L. Kewley, J. Moustakas, M. Sosey, D. A. Dale, K. D. Gordon, G. X. Helou, D. J. Hollenbach, L. Armus, G. Bendo, C. Bot, B. Buckalew, T. Jarrett, A. Li, M. Meyer, E. J. Murphy, M. Prescott, M. W. Regan, G. H. Rieke, H. Roussel, K. Sheth, J. D. T. Smith, M. D. Thornley, and F. Walter. The Calibration of Mid-Infrared Star Formation Rate Indicators. ApJ, 666:870–895, September 2007. doi: 10.1086/520082.

D. Calzetti, S.-Y. Wu, S. Hong, R. C. Kennicutt, J. C. Lee, D. A. Dale, C. W. Engelbracht, L. van Zee, B. T. Draine, C.-N. Hao, K. D. Gordon, J. Moustakas, E. J. Murphy, M. Regan, A. Begum, M. Block, J. Dalcanton, J. Funes, A. Gil de Paz, B. Johnson, S. Sakai, E. Skillman, F. Walter, D. Weisz, B. Williams, and Y. Wu. The Calibration of Monochromatic Far-Infrared Star Formation Rate Indicators. ApJ, 714:1256–1279, May 2010. doi: 10.1088/0004-637X/714/2/1256.

M. Cerviño, V. Luridiana, E. Pérez, J. M. Vílchez, and D. Valls-Gabaud. On emission-line spectra obtained from evolutionary synthesis models. I. Dispersion in the ionising flux and Lowest Luminosity Limits. A&A, 407:177–190, August 2003. doi: 10.1051/0004-6361:20030861.

J. J. Condon. Radio emission from normal galaxies. ARA&A, 30:575–611, 1992. doi: 10.1146/annurev.aa.30.090192.003043.

D. A. Dale, G. J. Bendo, C. W. Engelbracht, K. D. Gordon, M. W. Regan, L. Armus, J. M. Cannon, D. Calzetti, B. T. Draine, G. Helou, R. D. Joseph, R. C. Kennicutt, A. Li, E. J. Murphy, H. Roussel, F. Walter, H. M. Hanson, D. J. Hollenbach, T. H. Jarrett, L. J. Kewley, C. A. Lamanna, C. Leitherer, M. J. Meyer, G. H. Rieke, M. J. Rieke, K. Sheth, J. D. T. Smith, and M. D. Thornley. Infrared Spectral Energy Distributions of Nearby Galaxies. ApJ, 633:857–870, November 2005. doi: 10.1086/491642.

D. A. Dale, S. A. Cohen, L. C. Johnson, M. D. Schuster, D. Calzetti, C. W. Engelbracht, A. Gil de Paz, R. C. Kennicutt, J. C. Lee, A. Begum, M. Block, J. J. Dalcanton, J. G. Funes, K. D. Gordon, B. D. Johnson, A. R. Marble, S. Sakai, E. D. Skillman, L. van Zee, F. Walter, D. R. Weisz, B. Williams, S.-Y. Wu, and Y. Wu. The Spitzer Local Volume Legacy: Survey Description and Infrared Photometry. ApJ, 703:517–556, September 2009. doi: 10.1088/0004-637X/703/1/517.

G. de Vaucouleurs, A. de Vaucouleurs, H. G. Corwin, Jr., R. J. Buta, G. Paturel, and P. Fouqué. *Third Reference Catalogue of Bright Galaxies. Volume I: Explanations and references. Volume II: Data for galaxies between* 0^h *and* 12^h*. Volume III: Data for galaxies between* 12^h *and* 24^h*.* 1991.

F.-X. Desert, F. Boulanger, and J. L. Puget. Interstellar dust models for extinction and emission. A&A, 237:215–236, October 1990.

C. D. Dowell, M. Pohlen, C. Pearson, M. Griffin, T. Lim, G. J. Bendo, D. Benielli, J. J. Bock, P. Chanial, D. L. Clements, L. Conversi, M. Ferlet, T. Fulton, R. Gastaud, J. Glenn, T. Grundy, S. Guest, K. J. King, S. J. Leeks, L. Levenson, N. Lu, H. Morris, H. Nguyen, B. O'Halloran, S. Oliver, P. Panuzzo, A. Papageorgiou, E. Polehampton, D. Rigopoulou, H. Roussel, N. Schneider, B. Schulz, A. Schwartz, D. L. Shupe, B. Sibthorpe, S. Sidher, A. J. Smith, B. M. Swinyard, M. Trichas, I. Valtchanov, A. L. Woodcraft, C. K. Xu, and L. Zhang. Status of the SPIRE photometer data processing pipelines during the early phases of the Herschel Mission. In *Society of Photo-Optical Instrumentation Engineers (SPIE) Conference Series*, volume 7731 of *Society of Photo-Optical Instrumentation Engineers (SPIE) Conference Series*, July 2010. doi: 10.1117/12.858035.

B. T. Draine. Interstellar Dust Grains. ARA&A, 41:241–289, 2003. doi: 10.1146/annurev.astro.41.011802.094840.

B. T. Draine and A. Li. Infrared Emission from Interstellar Dust. I. Stochastic Heating of Small Grains. ApJ, 551:807–824, April 2001. doi: 10.1086/320227.

B. T. Draine, D. A. Dale, G. Bendo, K. D. Gordon, J. D. T. Smith, L. Armus, C. W. Engelbracht, G. Helou, R. C. Kennicutt, Jr., A. Li, H. Roussel, F. Walter, D. Calzetti, J. Moustakas, E. J. Murphy, G. H. Rieke, C. Bot, D. J. Hollenbach, K. Sheth, and H. I. Teplitz. Dust Masses, PAH Abundances, and Starlight Intensities in the SINGS Galaxy Sample. ApJ, 663:866–894, July 2007. doi: 10.1086/518306.

D. M. Elmegreen, F. R. Chromey, and A. R. Warren. Discovery of a Double Circumnuclear Ring and Minibar in the Starburst Galaxy M83. AJ, 116:2834–2840, December 1998. doi: 10.1086/300657.

C. W. Engelbracht, K. D. Gordon, G. H. Rieke, M. W. Werner, D. A. Dale, and W. B. Latter. Metallicity Effects on Mid-Infrared Colors and the 8 μm PAH Emission in Galaxies. ApJ, 628:L29–L32, July 2005. doi: 10.1086/432613.

C. W. Engelbracht, M. Blaylock, K. Y. L. Su, J. Rho, G. H. Rieke, J. Muzerolle, D. L. Padgett, D. C. Hines, K. D. Gordon, D. Fadda, A. Noriega-Crespo, D. M. Kelly, W. B. Latter, J. L. Hinz, K. A. Misselt, J. E. Morrison, J. A. Stansberry, D. L. Shupe, S. Stolovy, W. A. Wheaton, E. T. Young, G. Neugebauer, S. Wachter, P. G. Pérez-González, D. T. Frayer, and F. R. Marleau. Absolute Calibration and Characterization of the Multiband Imaging Photometer for Spitzer. I. The Stellar Calibrator Sample and the 24 μm Calibration. PASP, 119:994–1018, September 2007. doi: 10.1086/521881.

C. W. Engelbracht, G. H. Rieke, K. D. Gordon, J.-D. T. Smith, M. W. Werner, J. Moustakas, C. N. A. Willmer, and L. Vanzi. Metallicity Effects on Dust Properties in Starbursting Galaxies. ApJ, 678:804–827, May 2008. doi: 10.1086/529513.

J. J. Feldmeier, R. Ciardullo, and G. H. Jacoby. Planetary Nebulae as Standard Candles. XI. Application to Spiral Galaxies. ApJ, 479:231, April 1997. doi: 10.1086/512787.

N. M. Forster Schreiber, H. Roussel, M. Sauvage, and V. Charmandaris. Warm dust and aromatic bands as quantitative probes of star-formation activity. A&A, 419: 501–516, May 2004. doi: 10.1051/0004-6361:20040963.

K. Foyle, G. Natale, C. D. Wilson, C. C. Popescu, M. Baes, G. J. Bendo, M. Boquien, A. Boselli, A. Cooray, D. Cormier, I. De Looze, J. Fischera, O. Ł. Karczewski, V. Lebouteiller, S. Madden, M. Pereira-Santaella, M. W. L. Smith, L. Spinoglio, and R. J. Tuffs. Star formation and dust heating in the FIR bright sources of M83. MNRAS, 432:2182–2207, July 2013. doi: 10.1093/mnras/stt618.

W. L. Freedman, B. F. Madore, B. K. Gibson, L. Ferrarese, D. D. Kelson, S. Sakai, J. R. Mould, R. C. Kennicutt, Jr., H. C. Ford, J. A. Graham, J. P. Huchra, S. M. G. Hughes, G. D. Illingworth, L. M. Macri, and P. B. Stetson. Final Results from the Hubble Space Telescope Key Project to Measure the Hubble Constant. ApJ, 553:47–72, May 2001. doi: 10.1086/320638.

R. Genzel, D. Lutz, E. Sturm, E. Egami, D. Kunze, A. F. M. Moorwood, D. Rigopoulou, H. W. W. Spoon, A. Sternberg, L. E. Tacconi-Garman, L. Tacconi, and N. Thatte. What Powers Ultraluminous IRAS Galaxies? ApJ, 498:579, May 1998. doi: 10.1086/305576.

R. A. González-Lópezlira, J. Pflamm-Altenburg, and P. Kroupa. Gas Surface Density, Star Formation Rate Surface Density, and the Maximum Mass of Young Star Clusters in a Disk Galaxy. II. The Grand-design Galaxy M51. ApJ, 770:85, June 2013. doi: 10.1088/0004-637X/770/2/85.

K. D. Gordon, G. H. Rieke, C. W. Engelbracht, J. Muzerolle, J. A. Stansberry, K. A. Misselt, J. E. Morrison, J. Cadien, E. T. Young, H. Dole, D. M. Kelly, A. Alonso-Herrero, E. Egami, K. Y. L. Su, C. Papovich, P. S. Smith, D. C. Hines, M. J. Rieke, M. Blaylock, P. G. Pérez-González, E. Le Floc'h, J. L. Hinz, W. B. Latter, T. Hesselroth, D. T. Frayer, A. Noriega-Crespo, F. J. Masci, D. L. Padgett, M. P. Smylie, and N. M. Haegel. Reduction Algorithms for the Multiband Imaging Photometer for Spitzer. PASP, 117:503–525, May 2005. doi: 10.1086/429309.

K. D. Gordon, C. W. Engelbracht, G. H. Rieke, K. A. Misselt, J.-D. T. Smith, and R. C. Kennicutt, Jr. The Behavior of the Aromatic Features in M101 H II Regions: Evidence for Dust Processing. ApJ, 682:336–354, July 2008. doi: 10.1086/589567.

J. M. Greenberg. *Interstellar Grains*, page 221. the University of Chicago Press, January 1968.

M. Griffin, P. Ade, P. André, J.-P. Baluteau, J. Bock, A. Franceschini, W. Gear, J. Glenn, M. Huang, K. King, E. Lellouch, D. Naylor, S. Oliver, G. Olofsson, M. Page, I. Perez-Fournon, M. Rowan-Robinson, P. Saraceno, E. Sawyer, B. Swinyard, L. Vigroux, G. Wright, and A. Zavagno. The SPIRE Instrument. In L. Pagani and M. Gerin, editors, *EAS Publications Series*, volume 34 of *EAS Publications Series*, pages 33–42, 2009. doi: 10.1051/eas:0934003.

M. J. Griffin, A. Abergel, A. Abreu, P. A. R. Ade, P. André, J.-L. Augueres, T. Babbedge, Y. Bae, T. Baillie, J.-P. Baluteau, M. J. Barlow, G. Bendo, D. Benielli, J. J. Bock, P. Bonhomme, D. Brisbin, C. Brockley-Blatt, M. Caldwell, C. Cara, N. Castro-Rodriguez, R. Cerulli, P. Chanial, S. Chen, E. Clark, D. L. Clements, L. Clerc, J. Coker, D. Communal, L. Conversi, P. Cox, D. Crumb, C. Cunningham, F. Daly, G. R. Davis, P. de Antoni, J. Delderfield, N. Devin, A. di Giorgio, I. Didschuns, K. Dohlen, M. Donati, A. Dowell, C. D. Dowell, L. Duband, L. Dumaye, R. J. Emery, M. Ferlet, D. Ferrand, J. Fontignie, M. Fox, A. Franceschini, M. Frerking, T. Fulton, J. Garcia, R. Gastaud, W. K. Gear,

J. Glenn, A. Goizel, D. K. Griffin, T. Grundy, S. Guest, L. Guillemet, P. C. Hargrave, M. Harwit, P. Hastings, E. Hatziminaoglou, M. Herman, B. Hinde, V. Hristov, M. Huang, P. Imhof, K. J. Isaak, U. Israelsson, R. J. Ivison, D. Jennings, B. Kiernan, K. J. King, A. E. Lange, W. Latter, G. Laurent, P. Laurent, S. J. Leeks, E. Lellouch, L. Levenson, B. Li, J. Li, J. Lilienthal, T. Lim, S. J. Liu, N. Lu, S. Madden, G. Mainetti, P. Marliani, D. McKay, K. Mercier, S. Molinari, H. Morris, H. Moseley, J. Mulder, M. Mur, D. A. Naylor, H. Nguyen, B. O'Halloran, S. Oliver, G. Olofsson, H.-G. Olofsson, R. Orfei, M. J. Page, I. Pain, P. Panuzzo, A. Papageorgiou, G. Parks, P. Parr-Burman, A. Pearce, C. Pearson, I. Pérez-Fournon, F. Pinsard, G. Pisano, J. Podosek, M. Pohlen, E. T. Polehampton, D. Pouliquen, D. Rigopoulou, D. Rizzo, I. G. Roseboom, H. Roussel, M. Rowan-Robinson, B. Rownd, P. Saraceno, M. Sauvage, R. Savage, G. Savini, E. Sawyer, C. Scharmberg, D. Schmitt, N. Schneider, B. Schulz, A. Schwartz, R. Shafer, D. L. Shupe, B. Sibthorpe, S. Sidher, A. Smith, A. J. Smith, D. Smith, L. Spencer, B. Stobie, R. Sudiwala, K. Sukhatme, C. Surace, J. A. Stevens, B. M. Swinyard, M. Trichas, T. Tourette, H. Triou, S. Tseng, C. Tucker, A. Turner, M. Vaccari, I. Valtchanov, L. Vigroux, E. Virique, G. Voellmer, H. Walker, R. Ward, T. Waskett, M. Weilert, R. Wesson, G. J. White, N. Whitehouse, C. D. Wilson, B. Winter, A. L. Woodcraft, G. S. Wright, C. K. Xu, A. Zavagno, M. Zemcov, L. Zhang, and E. Zonca. The Herschel-SPIRE instrument and its in-flight performance. A&A, 518:L3, July 2010. doi: 10.1051/0004-6361/201014519.

B. Groves, O. Krause, K. Sandstrom, A. Schmiedeke, A. Leroy, H. Linz, M. Kapala, H.-W. Rix, E. Schinnerer, F. Tabatabaei, F. Walter, and E. da Cunha. The heating of dust by old stellar populations in the bulge of M31. MNRAS, 426: 892–902, October 2012. doi: 10.1111/j.1365-2966.2012.21696.x.

M. Haas, U. Klaas, and S. Bianchi. The relation of PAH strength with cold dust in galaxies. A&A, 385:L23–L26, April 2002. doi: 10.1051/0004-6361:20020222.

H. J. Habing. The interstellar radiation density between 912 A and 2400 A. , 19: 421, January 1968.

C.-N. Hao, R. C. Kennicutt, B. D. Johnson, D. Calzetti, D. A. Dale, and J. Moustakas. Dust-corrected Star Formation Rates of Galaxies. II. Combinations of Ultraviolet and Infrared Tracers. ApJ, 741:124, November 2011. doi: 10.1088/0004-637X/741/2/124.

J. Harris, D. Calzetti, J. S. Gallagher, III, C. J. Conselice, and D. A. Smith. Young Clusters in the Nuclear Starburst of M83. AJ, 122:3046–3064, December 2001. doi: 10.1086/324230.

J. S. Heiner, R. J. Allen, O. I. Wong, and P. C. van der Kruit. The volume densities of giant molecular clouds in M 83. A&A, 489:533–541, October 2008. doi: 10.1051/0004-6361:200810430.

G. Helou, B. T. Soifer, and M. Rowan-Robinson. Thermal infrared and nonthermal radio - Remarkable correlation in disks of galaxies. ApJ, 298:L7–L11, November 1985. doi: 10.1086/184556.

G. Helou, H. Roussel, P. Appleton, D. Frayer, S. Stolovy, L. Storrie-Lombardi, R. Hurt, P. Lowrance, D. Makovoz, F. Masci, J. Surace, K. D. Gordon, A. Alonso-Herrero, C. W. Engelbracht, K. Misselt, G. Rieke, M. Rieke, S. P. Willner, M. Pahre, M. L. N. Ashby, G. G. Fazio, and H. A. Smith. The Anatomy of Star Formation in NGC 300. ApJS, 154:253–258, September 2004. doi: 10.1086/422640.

H. Hirashita. Evolution model of dust content in galaxies - prospect of revealing the star formation history of the Universe. *Astronomical Herald*, 94:344–352, August 2001.

J. R. Houck, V. Charmandaris, B. R. Brandl, D. Weedman, T. Herter, L. Armus, B. T. Soifer, J. Bernard-Salas, H. W. W. Spoon, D. Devost, and K. I. Uchida. The Extraordinary Mid-infrared Spectrum of the Blue Compact Dwarf Galaxy SBS 0335-052. ApJS, 154:211–214, September 2004. doi: 10.1086/423137.

B. D. Johnson, D. Schiminovich, M. Seibert, M. Treyer, D. C. Martin, T. A. Barlow, K. Forster, P. G. Friedman, P. Morrissey, S. G. Neff, T. Small, T. K. Wyder,

L. Bianchi, J. Donas, T. M. Heckman, Y.-W. Lee, B. F. Madore, B. Milliard, R. M. Rich, A. S. Szalay, B. Y. Welsh, and S. K. Yi. Ultraviolet through Infrared Spectral Energy Distributions from 1000 SDSS Galaxies: Dust Attenuation. ApJS, 173:392–403, December 2007. doi: 10.1086/522960.

R. C. Kennicutt and N. J. Evans. Star Formation in the Milky Way and Nearby Galaxies. ARA&A, 50:531–608, September 2012. doi: 10.1146/annurev-astro-081811-125610.

R. C. Kennicutt, D. Calzetti, G. Aniano, P. Appleton, L. Armus, P. Beirão, A. D. Bolatto, B. Brandl, A. Crocker, K. Croxall, D. A. Dale, J. D. Meyer, B. T. Draine, C. W. Engelbracht, M. Galametz, K. D. Gordon, B. Groves, C.-N. Hao, G. Helou, J. Hinz, L. K. Hunt, B. Johnson, J. Koda, O. Krause, A. K. Leroy, Y. Li, S. Meidt, E. Montiel, E. J. Murphy, N. Rahman, H.-W. Rix, H. Roussel, K. Sandstrom, M. Sauvage, E. Schinnerer, R. Skibba, J. D. T. Smith, S. Srinivasan, L. Vigroux, F. Walter, C. D. Wilson, M. Wolfire, and S. Zibetti. KINGFISH – Key Insights on Nearby Galaxies: A Far-Infrared Survey with Herschel: Survey Description and Image Atlas. PASP, 123:1347–1369, December 2011. doi: 10.1086/663818.

R. C. Kennicutt, Jr. Star Formation in Galaxies Along the Hubble Sequence. ARA&A, 36:189–232, 1998. doi: 10.1146/annurev.astro.36.1.189.

R. C. Kennicutt, Jr., L. Armus, G. Bendo, D. Calzetti, D. A. Dale, B. T. Draine, C. W. Engelbracht, K. D. Gordon, A. D. Grauer, G. Helou, D. J. Hollenbach, T. H. Jarrett, L. J. Kewley, C. Leitherer, A. Li, S. Malhotra, M. W. Regan, G. H. Rieke, M. J. Rieke, H. Roussel, J.-D. T. Smith, M. D. Thornley, and F. Walter. SINGS: The SIRTF Nearby Galaxies Survey. PASP, 115:928–952, August 2003. doi: 10.1086/376941.

R. C. Kennicutt, Jr., C.-N. Hao, D. Calzetti, J. Moustakas, D. A. Dale, G. Bendo, C. W. Engelbracht, B. D. Johnson, and J. C. Lee. Dust-corrected Star Formation Rates of Galaxies. I. Combinations of Hα and Infrared Tracers. ApJ, 703:1672, October 2009. doi: 10.1088/0004-637X/703/2/1672.

U. Klein, R. Wielebinski, and H. W. Morsi. Radio continuum observations of M82. A&A, 190:41–46, January 1988.

H. A. Kobulnicky and K. E. Johnson. Signatures of the Youngest Starbursts: Optically Thick Thermal Bremsstrahlung Radio Sources in Henize 2-10. ApJ, 527: 154–166, December 1999. doi: 10.1086/308075.

J. Koda, N. Scoville, T. Sawada, M. A. La Vigne, S. N. Vogel, A. E. Potts, J. M. Carpenter, S. A. Corder, M. C. H. Wright, S. M. White, B. A. Zauderer, J. Patience, A. I. Sargent, D. C. J. Bock, D. Hawkins, M. Hodges, A. Kemball, J. W. Lamb, R. L. Plambeck, M. W. Pound, S. L. Scott, P. Teuben, and D. P. Woody. Dynamically Driven Evolution of the Interstellar Medium in M51. ApJ, 700:L132–L136, August 2009. doi: 10.1088/0004-637X/700/2/L132.

X. Kong, S. Charlot, J. Brinchmann, and S. M. Fall. Star formation history and dust content of galaxies drawn from ultraviolet surveys. MNRAS, 349:769–778, April 2004. doi: 10.1111/j.1365-2966.2004.07556.x.

J. Kormendy and R. C. Kennicutt, Jr. Secular Evolution and the Formation of Pseudobulges in Disk Galaxies. ARA&A, 42:603–683, September 2004. doi: 10.1146/annurev.astro.42.053102.134024.

D. Kunth and G. Östlin. The most metal-poor galaxies. A&A Rev., 10:1–79, 2000. doi: 10.1007/s001590000005.

G. Lagache, J.-L. Puget, and H. Dole. Dusty Infrared Galaxies: Sources of the Cosmic Infrared Background. ARA&A, 43:727–768, September 2005. doi: 10.1146/annurev.astro.43.072103.150606.

A. Li and B. T. Draine. Infrared Emission from Interstellar Dust. II. The Diffuse Interstellar Medium. ApJ, 554:778–802, June 2001. doi: 10.1086/323147.

N. Lu, G. Helou, M. W. Werner, H. L. Dinerstein, D. A. Dale, N. A. Silbermann,

S. Malhotra, C. A. Beichman, and T. H. Jarrett. Infrared Emission of Normal Galaxies from 2.5 to 12 Micron: Infrared Space Observatory Spectra, Near-Infrared Continuum, and Mid-Infrared Emission Features. ApJ, 588:199–217, May 2003. doi: 10.1086/374043.

A. A. Lundgren, T. Wiklind, H. Olofsson, and G. Rydbeck. Molecular gas in the galaxy M 83. I. The molecular gas distribution. A&A, 413:505–523, January 2004. doi: 10.1051/0004-6361:20031507.

A. A. Lundgren, H. Olofsson, T. Wiklind, and R. Beck. Star Formation and Molecular Gas in M83. In J. H. Knapen, T. J. Mahoney, and A. Vazdekis, editors, *Pathways Through an Eclectic Universe*, volume 390 of *Astronomical Society of the Pacific Conference Series*, page 144, June 2008.

S. C. Madden, F. Galliano, A. P. Jones, and M. Sauvage. ISM properties in low-metallicity environments. A&A, 446:877–896, February 2006. doi: 10.1051/0004-6361:20053890.

E. Mentuch, R. G. Abraham, K. Glazebrook, P. J. McCarthy, H. Yan, D. V. O'Donnell, D. Le Borgne, S. Savaglio, D. Crampton, R. Murowinski, S. Juneau, R. G. Carlberg, I. Jørgensen, K. Roth, H.-W. Chen, and R. O. Marzke. A Near-Infrared Excess in the Continuum of High-redshift Galaxies: A Tracer of Star Formation and Circumstellar Disks? ApJ, 706:1020–1035, December 2009. doi: 10.1088/0004-637X/706/2/1020.

E. Mentuch, R. G. Abraham, and S. Zibetti. A Simple Connection Between the Near- and Mid-infrared Emission of Galaxies and Their Star Formation Rates. ApJ, 725:1971–1983, December 2010. doi: 10.1088/0004-637X/725/2/1971.

P. G. Mezger and A. P. Henderson. Galactic H II Regions. I. Observations of Their Continuum Radiation at the Frequency 5 GHz. ApJ, 147:471, February 1967. doi: 10.1086/149030.

E. J. Murphy, J. J. Condon, E. Schinnerer, R. C. Kennicutt, D. Calzetti, L. Armus, G. Helou, J. L. Turner, G. Aniano, P. Beirão, A. D. Bolatto, B. R. Brandl, K. V.

Croxall, D. A. Dale, J. L. Donovan Meyer, B. T. Draine, C. Engelbracht, L. K. Hunt, C.-N. Hao, J. Koda, H. Roussel, R. Skibba, and J.-D. T. Smith. Calibrating Extinction-free Star Formation Rate Diagnostics with 33 GHz Free-free Emission in NGC 6946. ApJ, 737:67, August 2011. doi: 10.1088/0004-637X/737/2/67.

A. G. Noble, J. S. Gallagher, and K. E. Dellenbusch. Mapping Tidal Interactions in the M51 System. In *American Astronomical Society Meeting Abstracts*, volume 38 of *Bulletin of the American Astronomical Society*, page 898, December 2006.

M. Ouchi, Y. Ono, E. Egami, T. Saito, M. Oguri, P. J. McCarthy, D. Farrah, N. Kashikawa, I. Momcheva, K. Shimasaku, K. Nakanishi, H. Furusawa, M. Akiyama, J. S. Dunlop, A. M. J. Mortier, S. Okamura, M. Hayashi, M. Cirasuolo, A. Dressler, M. Iye, M. J. Jarvis, T. Kodama, C. L. Martin, R. J. McLure, K. Ohta, T. Yamada, and M. Yoshida. Discovery of a Giant Lyα Emitter Near the Reionization Epoch. ApJ, 696:1164–1175, May 2009. doi: 10.1088/0004-637X/696/2/1164.

E. Peeters, S. Hony, C. Van Kerckhoven, A. G. G. M. Tielens, L. J. Allamandola, D. M. Hudgins, and C. W. Bauschlicher. The rich 6 to 9 vec mu m spectrum of interstellar PAHs. A&A, 390:1089–1113, August 2002. doi: 10.1051/0004-6361:20020773.

E. Peeters, H. W. W. Spoon, and A. G. G. M. Tielens. Polycyclic Aromatic Hydrocarbons as a Tracer of Star Formation? ApJ, 613:986–1003, October 2004. doi: 10.1086/423237.

A. Poglitsch, C. Waelkens, N. Geis, H. Feuchtgruber, B. Vandenbussche, L. Rodriguez, O. Krause, E. Renotte, C. van Hoof, P. Saraceno, J. Cepa, F. Kerschbaum, P. Agnèse, B. Ali, B. Altieri, P. Andreani, J.-L. Augueres, Z. Balog, L. Barl, O. H. Bauer, N. Belbachir, M. Benedettini, N. Billot, O. Boulade, H. Bischof, J. Blommaert, E. Callut, C. Cara, R. Cerulli, D. Cesarsky, A. Contursi, Y. Creten, W. De Meester, V. Doublier, E. Doumayrou, L. Duband, K. Exter,

R. Genzel, J.-M. Gillis, U. Grözinger, T. Henning, J. Herreros, R. Huygen, M. Inguscio, G. Jakob, C. Jamar, C. Jean, J. de Jong, R. Katterloher, C. Kiss, U. Klaas, D. Lemke, D. Lutz, S. Madden, B. Marquet, J. Martignac, A. Mazy, P. Merken, F. Montfort, L. Morbidelli, T. Müller, M. Nielbock, K. Okumura, R. Orfei, R. Ottensamer, S. Pezzuto, P. Popesso, J. Putzeys, S. Regibo, V. Reveret, P. Royer, M. Sauvage, J. Schreiber, J. Stegmaier, D. Schmitt, J. Schubert, E. Sturm, M. Thiel, G. Tofani, R. Vavrek, M. Wetzstein, E. Wieprecht, and E. Wiezorrek. The Photodetector Array Camera and Spectrometer (PACS) on the Herschel Space Observatory. A&A, 518:L2, July 2010. doi: 10.1051/0004-6361/201014535.

C. C. Popescu, R. J. Tuffs, M. A. Dopita, J. Fischera, N. D. Kylafis, and B. F. Madore. Modelling the spectral energy distribution of galaxies. V. The dust and PAH emission SEDs of disk galaxies. A&A, 527:A109, March 2011. doi: 10.1051/0004-6361/201015217.

M. K. M. Prescott, R. C. Kennicutt, Jr., G. J. Bendo, B. A. Buckalew, D. Calzetti, C. W. Engelbracht, K. D. Gordon, D. J. Hollenbach, J. C. Lee, J. Moustakas, D. A. Dale, G. Helou, T. H. Jarrett, E. J. Murphy, J.-D. T. Smith, S. Akiyama, and M. L. Sosey. The Incidence of Highly Obscured Star-forming Regions in SINGS Galaxies. ApJ, 668:182–202, October 2007. doi: 10.1086/521071.

P. Ranalli, A. Comastri, and G. Setti. The 2-10 keV luminosity as a Star Formation Rate indicator. A&A, 399:39–50, February 2003. doi: 10.1051/0004-6361:20021600.

M. W. Regan, M. D. Thornley, S. N. Vogel, K. Sheth, B. T. Draine, D. J. Hollenbach, M. Meyer, D. A. Dale, C. W. Engelbracht, R. C. Kennicutt, L. Armus, B. Buckalew, D. Calzetti, K. D. Gordon, G. Helou, C. Leitherer, S. Malhotra, E. Murphy, G. H. Rieke, M. J. Rieke, and J. D. Smith. The Radial Distribution of the Interstellar Medium in Disk Galaxies: Evidence for Secular Evolution. ApJ, 652:1112–1121, December 2006. doi: 10.1086/505382.

G. H. Rieke, A. Alonso-Herrero, B. J. Weiner, P. G. Pérez-González, M. Blaylock,

J. L. Donley, and D. Marcillac. Determining Star Formation Rates for Infrared Galaxies. ApJ, 692:556–573, February 2009. doi: 10.1088/0004-637X/692/1/556.

H. Roussel. Scanamorphos: a map-making software for Herschel and similar scanning bolometer arrays. *ArXiv e-prints*, May 2012.

H. Roussel, M. Sauvage, L. Vigroux, and A. Bosma. The relationship between star formation rates and mid-infrared emission in galactic disks. A&A, 372:427–437, June 2001. doi: 10.1051/0004-6361:20010498.

M. Rowan-Robinson, I. G. Roseboom, M. Vaccari, A. Amblard, V. Arumugam, R. Auld, H. Aussel, T. Babbedge, A. Blain, J. Bock, A. Boselli, D. Brisbin, V. Buat, D. Burgarella, N. Castro-Rodriguez, A. Cava, P. Chanial, D. L. Clements, A. Conley, L. Conversi, A. Cooray, C. D. Dowell, E. Dwek, S. Dye, S. Eales, D. Elbaz, D. Farrah, M. Fox, A. Franceschini, W. Gear, J. Glenn, E. A. González Solares, M. Griffin, M. Halpern, E. Hatziminaoglou, J. Huang, E. Ibar, K. Isaak, R. J. Ivison, G. Lagache, L. Levenson, N. Lu, S. Madden, B. Maffei, G. Mainetti, L. Marchetti, A. M. J. Mortier, H. T. Nguyen, B. O'Halloran, S. J. Oliver, A. Omont, M. J. Page, P. Panuzzo, A. Papageorgiou, H. Patel, C. P. Pearson, I. Perez Fournon, M. Pohlen, J. I. Rawlings, G. Raymond, D. Rigopoulou, D. Rizzo, B. Schulz, D. Scott, N. Seymour, D. L. Shupe, A. J. Smith, J. A. Stevens, M. Symeonidis, M. Trichas, K. E. Tugwell, I. Valtchanov, L. Vigroux, L. Wang, R. Ward, G. Wright, C. K. Xu, and M. Zemcov. Cold dust and young starbursts: spectral energy distributions of Herschel SPIRE sources from the HerMES survey. MNRAS, 409:2–11, November 2010. doi: 10.1111/j.1365-2966.2010.17041.x.

S. Salim, R. M. Rich, S. Charlot, J. Brinchmann, B. D. Johnson, D. Schiminovich, M. Seibert, R. Mallery, T. M. Heckman, K. Forster, P. G. Friedman, D. C. Martin, P. Morrissey, S. G. Neff, T. Small, T. K. Wyder, L. Bianchi, J. Donas, Y.-W. Lee, B. F. Madore, B. Milliard, A. S. Szalay, B. Y. Welsh, and S. K. Yi. UV Star Formation Rates in the Local Universe. ApJS, 173:267–292, December 2007. doi: 10.1086/519218.

A. Sandage. The brightest stars in nearby galaxies. III - The color-magnitude diagram for the brightest red and blue stars in M81 and Holmberg IX. IV - The color-magnitude diagram for the brightest red and blue stars in NGC 2403. AJ, 89:621–635, May 1984. doi: 10.1086/113558.

M. Sauvage and T. X. Thuan. On the use of far-infrared luminosity as a star formation indicator in galaxies. ApJ, 396:L69–L73, September 1992. doi: 10.1086/186519.

M. Schmidt. The Rate of Star Formation. ApJ, 129:243, March 1959a. doi: 10.1086/146614.

M. Schmidt. The Rate of Star Formation. ApJ, 129:243, March 1959b. doi: 10.1086/146614.

M. Seibert, D. C. Martin, T. M. Heckman, V. Buat, C. Hoopes, T. Barlow, L. Bianchi, Y.-I. Byun, J. Donas, K. Forster, P. G. Friedman, P. Jelinsky, Y.-W. Lee, B. F. Madore, R. Malina, B. Milliard, P. Morrissey, S. Neff, R. M. Rich, D. Schiminovich, O. Siegmund, T. Small, A. S. Szalay, B. Welsh, and T. K. Wyder. Testing the Empirical Relation between Ultraviolet Color and Attenuation of Galaxies. ApJ, 619:L55–L58, January 2005. doi: 10.1086/427843.

B. J. Smith and M. Hancock. The Origin of the 4.5 μm Excess from Dwarf Galaxies. AJ, 138:130–145, July 2009. doi: 10.1088/0004-6256/138/1/130.

J. D. T. Smith and R. C. Kennicutt. The SINGS Spectroscopic Legacy: PAH Variations. In L. Armus and W. T. Reach, editors, *Astronomical Society of the Pacific Conference Series*, volume 357 of *Astronomical Society of the Pacific Conference Series*, page 179, December 2006.

M. W. L. Smith, S. A. Eales, H. L. Gomez, J. Roman-Duval, J. Fritz, R. Braun, M. Baes, G. J. Bendo, J. A. D. L. Blommaert, M. Boquien, A. Boselli, D. L. Clements, A. R. Cooray, L. Cortese, I. de Looze, G. P. Ford, W. K. Gear, G. Gentile, K. D. Gordon, J. Kirk, V. Lebouteiller, S. Madden, E. Mentuch,

B. O'Halloran, M. J. Page, B. Schulz, L. Spinoglio, J. Verstappen, C. D. Wilson, and D. A. Thilker. The Herschel Exploitation of Local Galaxy Andromeda (HELGA). II. Dust and Gas in Andromeda. ApJ, 756:40, September 2012. doi: 10.1088/0004-637X/756/1/40.

D. A. Thilker, L. Bianchi, S. Boissier, A. Gil de Paz, B. F. Madore, D. C. Martin, G. R. Meurer, S. G. Neff, R. M. Rich, D. Schiminovich, M. Seibert, T. K. Wyder, T. A. Barlow, Y.-I. Byun, J. Donas, K. Forster, P. G. Friedman, T. M. Heckman, P. N. Jelinsky, Y.-W. Lee, R. F. Malina, B. Milliard, P. Morrissey, O. H. W. Siegmund, T. Small, A. S. Szalay, and B. Y. Welsh. Recent Star Formation in the Extreme Outer Disk of M83. ApJ, 619:L79–L82, January 2005. doi: 10.1086/425251.

M. D. Thornley and C. D. Wilson. Molecular Gas in the Inner 3.2 Kiloparsecs of NGC 2403: Star Formation at Subcritical Gas Surface Densities. ApJ, 447:616, July 1995. doi: 10.1086/175903.

A. G. G. M. Tielens. Interstellar Polycyclic Aromatic Hydrocarbon Molecules. ARA&A, 46:289–337, September 2008. doi: 10.1146/annurev.astro.46.060407.145211.

M. Treyer, D. Schiminovich, B. Johnson, M. Seibert, T. Wyder, T. A. Barlow, T. Conrow, K. Forster, P. G. Friedman, D. C. Martin, P. Morrissey, S. G. Neff, T. Small, L. Bianchi, J. Donas, T. M. Heckman, Y.-W. Lee, B. F. Madore, B. Milliard, R. M. Rich, A. S. Szalay, B. Y. Welsh, and S. K. Yi. Extinction-corrected Star Formation Rates Empirically Derived from Ultraviolet-Optical Colors. ApJS, 173:256–266, December 2007. doi: 10.1086/521794.

R. J. Trumpler. Absorption of Light in the Galactic System. PASP, 42:214, August 1930. doi: 10.1086/124039.

R. B. Tully. The Kinematics and Dynamics of M51. 11. Axisymmetric Properties. ApJS, 27:437, May 1974. doi: 10.1086/190305.

J. L. Turner and P. T. P. Ho. The 1 parsec radio core and possible nuclear ejection in NGC 253. ApJ, 299:L77–L81, December 1985. doi: 10.1086/184584.

J. L. Turner, P. T. P. Ho, and S. C. Beck. The Radio Properties of NGC 5253 and Its Unusual H II Regions. AJ, 116:1212–1220, September 1998. doi: 10.1086/300485.

C. Vlahakis, P. van der Werf, F. P. Israel, and R. P. J. Tilanus. A CO J = 3-2 map of M51 with HARP-B: radial properties of the spiral structure. MNRAS, 433: 1837–1861, August 2013. doi: 10.1093/mnras/stt841.

M. W. Werner, K. I. Uchida, K. Sellgren, M. Marengo, K. D. Gordon, P. W. Morris, J. R. Houck, and J. A. Stansberry. New Infrared Emission Features and Spectral Variations in NGC 7023. ApJS, 154:309–314, September 2004. doi: 10.1086/422413.

Y.-N. Zhu, H. Wu, C. Cao, and H.-N. Li. Correlations between Mid-Infrared, Far-Infrared, Hα, and FUV Luminosities for Spitzer SWIRE Field Galaxies. ApJ, 686:155–171, October 2008. doi: 10.1086/591121.